Higher Order Modes and Beam Dynamics at The European Spallation Source

A thesis submitted to the University of Manchester for the degree of
Doctor of Philosophy
in the Faculty of Science and Engineering

2017

Aaron Farricker

School of Physics and Astronomy

Contents

Word Count: 40,770

List of Figures

List of Tables

Abstract

Neutron sources provide a key tool in the study of materials and one of the key limiting factors in these experiments is often the total neutron flux. The European Spallation Source (ESS) in Lund, Sweden has set the goal to become the most intense source of cold neutrons in the world. At ESS a 2 GeV, 62.5 mA proton beam will be collided with a solid tungsten target to produce neutrons via spallation with an average beam power of 5 MW. The desired energy is obtained through the use of three families of superconducting accelerating structures from which 96% of the beam energy is gained. The fundamental goal in the accelerator design is to meet the desired power whilst minimising losses which can reduce the performance of the machine and may cause damage to the many sensitive components. One possible source of beam loss in the accelerator is beam-excited higher-order modes (HOMs). These are usually damped using HOM couplers to reduce the impact on the beam, at ESS however, designers have opted to forgo their use and rely instead on careful cavity design and production. Manufacturing errors are inherent in production processes and it is these which can result in the frequencies of HOMs varying from cavity-to-cavity—which in the worst case could have catastrophic consequences for the machine. The focus in this research is to analyse the impact of HOMs when manufacturing errors are present. To this end, detailed modal simulations have been performed to study the cavity designs and the impact of geometric errors on their modal spectra. These simulations have been used in conjunction with an equivalent circuit model to analyse the impact of geometric errors in individual cells of the full modal structure of the cavity. These simulations suggest that errors of less than 400 μm are sufficient to prevent the HOMs in the elliptical cavities becoming dangerous. This has been combined with detailed beam dynamics studies performed using a drift-kick-drift scheme to analyse the limits set by ESS to mitigate the impact of HOMs on the beam. The result of this study was series of limits on the frequencies and R/Q of HOMs with the most important being a possible reduction in the allowable separation of HOMs from harmonics of the bunch frequency by up to 50%. In addition, a redesign of the high-β cavity was undertook, which reduced the frequency separation of the dangerous HOMs from the ESS HOM frequency separation limit of 5 MHz from 5.38 MHz to 12.95 MHz.

Declaration

No portion of the work referred to in this thesis has been submitted in support of an application for another degree or qualification at this or any other university or other institution of learning.

Copyright

[1] http://documents.manchester.ac.uk/DocuInfo.aspx?DocID=487
[2] http://www.manchester.ac.uk/library/aboutus/regulations

Acknowledgements

Firstly, I would like to thank my supervisor Roger Jones for his encouragement and support throughout the last three and a half years. Without his support and guidance this work would not have been possible. I would also like to thank Stephen Molloy for the time he took to provide both guidance and technical expertise.

I benefited greatly from discussions with many colleagues at ESS and CEA Saclay. I thank them for their comments and suggestions which helped to shape this work.

Next I would like to thank my friends and colleagues at the University of Manchester and the Cockroft Institute for their incredible support and encouragement. Thanks go the past and present members of the MEW group for their help through our weekly meetings and various discussions. Particular thanks must go to Nirav Joshi, Matthew Crouch and Andrew Green for being kind enough to read through this manuscript and for managing to reduce the number of mistakes.

A special mention must also go to my family and friends who have provided unwavering support throughout this work. Most of all thanks must go to my Mum, Dad and brother Liam for being there to encourage and support me through both the good and the bad times.

Finally, I would like to dedicate this thesis to the memories of my friend John Ellis, my grandfather Kevin Farricker and my grandmother Irene Stewart who passed away during the course of this work.

Chapter 1

Introduction

Since the early part of the 20th century, particle accelerators have grown to play a key role in research, industry and medicine. In the last decade the demand for accelerators for various applications has increased steadily. Accelerators are used in many fields, for example, in radiotherapy for the treatment of cancer, as light or neutron sources and to investigate the structure and origins of our universe by utilising machines such as the Large Hadron Collider (LHC) [1] at the European Organisation for Nuclear Research (CERN) [2]. In the field of material science; high intensity light sources such as synchrotrons and free electron lasers (FELs) have been key in furthering the understanding of materials in parallel with data taken using high intensity neutron sources such as ISIS [3] and SNS [4].

In many of these fields the accelerator has not only been responsible for discoveries but also in pushing the boundaries of current technology and driving innovation.

The earliest accelerators used static electric fields to accelerate particles; electrostatic accelerators include the cathode ray tube used by Thomson to measure the charge to mass ratio of the electron in 1896 [5] and the Cockcroft-Walton accelerator used to split the lithium atom in 1932 [6]. The applications of elec-

trostatic accelerators are limited due to electrical breakdown which ultimately limits their accelerating gradient.

To overcome the limitation of accelerating gradient in electrostatic accelerators the concept of radio frequency (RF) acceleration was proposed, first by Ising in 1924 [7] before being developed and patented by Winderöe in 1928 [8]. The linear accelerator (linac) designed by Winderöe was the first step along the path that has lead to the development of a vast catalogue of machines which are operational today.

Accelerators can be placed into two distinct classes: either circular or linear. In a circular machine the beam is bent into a closed circular orbit where it can circulate in the same machine many times, whereas in a linear machine, the beam traverses only once.

Both the circular and linear machines rely on electromagnetic (EM) fields to manipulate the beam. The force, $\vec{F}$ experience by a charge moving through an EM field is given by the Lorentz force law [9];

$$\vec{F} = q\left(\vec{E} + \vec{v} \times \vec{B}\right) \tag{1.1}$$

where q is the particle's charge, $\vec{v}$ is the particle's velocity, $\vec{E}$ and $\vec{B}$ are the electric and magnetic fields respectively. In equation 1.1 it can be seen that the force due to the magnetic field is always perpendicular to the particle's velocity and hence cannot accelerate the particle. Further the force due to the electric field is independent of the particle's velocity and hence is able to cause the particle to gain energy and also change trajectory. As a consequence accelerators are generally made up of two key components; accelerating structures used to accelerate the beam using electric fields and magnets used to manipulate the beam shape and trajectory. In the case of RF accelerators the accelerating structures take the

form of cavities. More detailed descriptions of the various types of accelerator and the relevant beam physics can be found in [10–12].

One of the fundamental components of any RF accelerator is its accelerating cavities. Many types of accelerating cavities have been developed for various applications; a broad overview can be found in [13]. In general, cavities fall into two categories—either Normal Conducting (NC) or Superconducting (SC)—depending on the materials used in their construction and the temperature at which they operate. The main advantage of superconducting radio frequency (SCRF) cavities is the significant reduction in surface resistance, typically by 4-6 orders of magnitude compared to normal conducting radio frequency (NCRF) cavities. This reduction in surface resistance, even after accounting for the cryo-efficiency results in a significant power reduction compared to an equivalent NCRF structure [14].

In many situations NCRF cavities have appreciable advantages over SCRF cavities in particular in situations where space at a premium. This is owing to the fact that as the NC materials can withstand higher fields which combined with the ability to support higher frequencies results in accelerating gradients of the order of 100 MV/m or more being obtainable for a given beam current and pulse length. This means that less space is required per unit of energy gain and the accelerators overall length can be reduced. Further copper—which is most often used—is relatively cheap and easy to manufacture through many common machining techniques [15]. Overall SRCF cavities typically have a higher capital cost than NC cavities in part due to the manufacturing costs and also due to the additional cryogenic systems required.

1.1 Uses of SCRF Cavities

Due to the reduction in power loss from SCRF cavities compared to NC cavities and the need for CW operation, SCRF cavities are becoming increasingly popular. This is increasingly the case when high duty cycles are required as the power lost in NCRF cavities begins to become detrimental to the machine efficiency. This section will briefly outline the current and proposed facilities utilising SCRF technology.

1.1.1 Lepton machines

In lepton machines the particle which in usually accelerated is the electron (or positron) which, due to its low mass compared to ions or protons, obtains relativistic velocities (i.e. a kinetic energy comparable to its rest mass energy) within a fraction of the distance required for ions to do the same. As a result of this the velocity of the particle is almost constant throughout most of the machine and hence the design of each accelerating cell and other parameters are essentially constant. One of the most popular SCRF cavities for lepton machines is the TESLA cavity [16] which is a 1.3 GHz, 9-cell elliptical cavity designed to minimise surface EM fields whilst maximising the shunt impedance, allowing for optimised accelerating gradients due to reduced sensitivity to thermal breakdown, multipacting and field emission.

Future Colliders

The successor to the LHC is likely to be a linear collider, which will collide positrons and electrons with a centre of mass energy in the 100's GeV to TeV energy range. The alternative is a circular machine on the 100 km scale with a centre of mass energy on the TeV scale with the potential to convert to a hadron

machine in the future, one candidate is the Future Circular Collider (FCC) [17]. The FCC would be a ring with circumference of 100 km utilising several 400 or 800 MHz SCRF accelerating cavities.

One of the proposed linear machines is the International Linear Collider (ILC) [18] which will consist of two 10 km long SCRF linacs, one accelerating an electron beam and the other a positron beam up to a final centre of mass energy of 500 GeV before collision. Each of the linacs will contain nearly 8,000 TESLA style SCRF cavities with an average accelerating gradient of 31.5 MeV/m. If the project receives funding, construction of the cavities will commence on an unprecedented scale in an international context.

Free Electron Lasers

Another important application is to 4^{th} generation light sources or Free Electron Lasers (FELs) [19]. In these machines SCRF cavities are used to accelerate electrons to energies in the GeV range before passing them to insertion devices to produce radiation ranging over the EM spectrum from the THz to hard X-rays ($E = 5 - 10$ keV). An insertion device uses spatially alternating magnetic fields which cause the beam to undulate, producing radiation. This initial radiation causes the beam to micro bunch and radiate coherently. These machines produce very high brightness, short pulses of photon beams for uses in material, medical and biological science studies. Current and future machines include FLASH [20], X-FEL [21] and LCLS-II [22].

1.1.2 Hadron Machines

Hadron machines pose additional difficulties compared to lepton machines as the beam velocity—particularly in the early stages of acceleration—is much less than

the speed of light and changes significantly from cavity-to-cavity. This varying velocity means several types of cavity need to be designed for different velocity ranges in a single machine. As a result, a large array of different cavities have been designed for various energy ranges including; elliptical cavities, spoke cavities, quarter- and half-wave resonators [23].

Accelerator Driven Systems

An accelerator driven system (ADS) is a nuclear reactor system which allows fission to occur within a radioactive fuel whilst keeping it in a sub-critical state [24]. An ADS would use a proton accelerator and a fixed target to produce spallation neutrons, which initiate fission in a sub-critical reactor core. Being sub-critical means that the fissile material does not produce enough neutrons to sustain a chain reaction and as such when the accelerator is turned off, fission processes begin to decrease in frequency. The ADS concept is usually discussed in the context of transmutation of radioactive waste, where a long lived isotope of decay times upwards of 1,000 years is taken and transmutated into an isotope with a lifetime of order 100 years. Currently the ADS demonstrator, MYRRHA [25] is under construction.

Radioactive Ion Beam Facilities

Radioactive ion beam facilities (RIBs) [26] such as the Facility for Rare Ion Beams (FRIB) [27], in Michigan, USA, are used to produce rare isotopes for study and uses in medical applications. In the case of FRIB the accelerating cavities used will be of the quarter- and half-wave resonator types. These facilities operate by colliding a high power proton beam with a target to produce rare ions through nuclear interactions induced by the beam. Another example of such a

machine in HIE-ISOLDE at CERN [28]. The ions that these machines produces have short lifetimes and cannot be readily produced through other methods.

Neutrino Factories

Due to the very low interaction cross section for neutrinos with particle physics detectors, large fluxes of neutrinos are required to perform measurements [29]. To produce high fluxes, a proton beam can be collided with a target to produce neutrons or pions, which then through electroweak-decay produce a beam of electron or muon neutrinos. For a facility to be feasible, it would require a high power and current, GeV energy proton beam. The T2K [30] experiment at JPARC is already in use and future projects could include the SPL [31] and Project X [32].

Neutron Sources

Neutron scattering [33] is a technique used to investigate the properties of materials that allows the nuclei of a material to be viewed directly, with no interference from the electron cloud and as such is very useful. In neutron experiments, large fluxes of neutrons are desirable and there is a limit to how much flux can be supplied by nuclear decay or fission sources. One process that can be used to improve the neutron flux is spallation, which involves the emission of neutrons from an excited nuclei. This excitation can be achieved through several processes, but a high power proton beam is ideal and demand for such facilities is growing.

Early neutron scattering experiments relied on purpose-built high flux neutron reactors such as ILL [35]. However, newer facilities are tending towards accelerator driven production; the first such facility was ISIS [3] which began

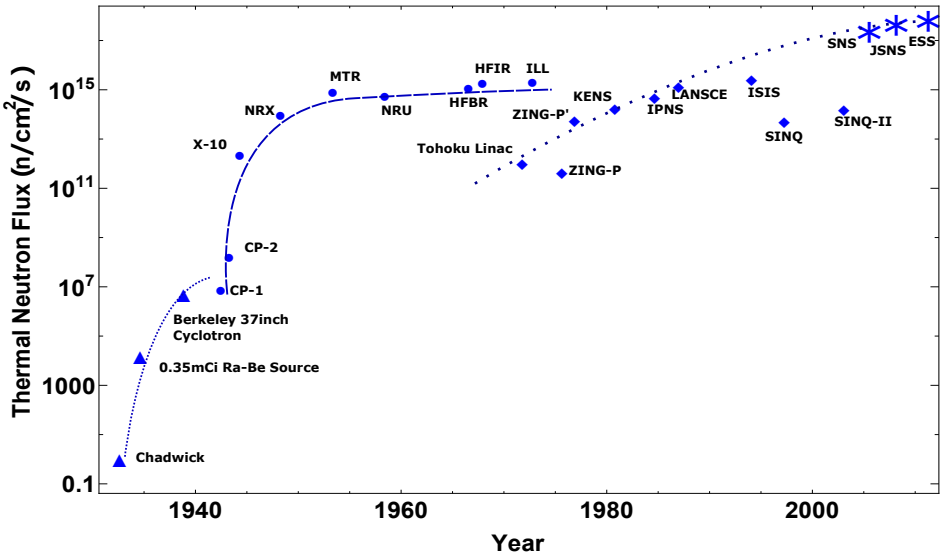

Figure 1.1: Comparison of peak thermal neutron flux. Data has been updated from [34]. Particle sources are plotted with triangles, fission sources with circles and spallation sources are plotted as diamonds with the exception of the three newest machine which are plotted with stars.

construction in the late 1970's and is still in operation. The demand for higher and higher fluxes has led to SCRF proton linacs being used as high power drivers for new sources.

In 2006 the spallation neutron source (SNS) [4] began operation using a SCRF linac to produce neutrons via spallation using a liquid mercury target. Another machine currently under construction is the European Spallation Source (ESS), which is part of a pan-European consortium. The design of this linac is the focus of this thesis and some of the essential characteristics of it are described in the following section.

1.2 The European Spallation Source

The ESS is a European project with contribution from 19 European countries. The ESS is currently under construction in Lund, Sweden with the first beam

anticipated in 2019 and full operation expected in 2022. When fully operational the ESS will be a slow neutron source of unparalleled power and scientific performance.

The ESS will be five times more powerful than the worlds current leading neutron source and hence offers an unprecedented neutron flux. This high neutron flux will enable experiments which as yet cannot be performed. This includes experiments that require: fast measurements, the measurement of small samples and the increased use of polarised neutrons. Further the long pulse of the ESS will make it possible to use long wavelength neutrons to achieve a wider dynamic range in experiments.

The beam of the ESS will be collided with a solid rotating tungsten target at an energy of 2 GeV to produce high energy spallation neutrons which are then thermalised using a moderator. Due to the isotropic angular distribution of neutron production via spallation the target will be surrounded by 22 experimental beam line which will allow for a large throughput of users.

1.2.1 The Beam Parameters at ESS

The ESS spallation source has been designed with the aim of achieving an average beam power of protons on target of 5 MW putting it ahead of all other linacs in terms of power and allowing the ESS to be the brightest source of thermal neutrons in the world. The average beam power of a linac is given by

$$P[\mathrm{W}] = E[\mathrm{eV}] \times I[\mathrm{A}] \times \text{duty cycle}. \tag{1.2}$$

The targeted power sets the beam parameters and consequently shapes the design of the accelerator. The proposed design in the technical design report [36,

37] was for a 50 mA beam with a final energy of 2.5 GeV at a 4% duty cycle. However in 2013 the ESS accelerator was redesigned to reduce costs whilst keeping the scope of the project the same. The main changes entailed a reduction in beam energy by 20% to 2 GeV and therefore to ensure the average beam power of 5 MW was maintained the average beam current was raised by 25% to 62.5 mA (c.f. equation 1.2). A summary of the current beam parameters are shown in table 1.1.

The redesign significantly changed the accelerator (see section 1.2.2) by reducing the number of elliptical cryomodules by 33%—from 45 to 30—and compensating for the resulting energy discrepancy by increasing the accelerating gradient of the remaining cavities by 10%. These changes result in a design which is more cost effective, but includes more technical risk in the form of increased power per cavity and increased cavity surface fields.

Parameter	Value	Units
Beam Power	5	MW
Final Beam Energy	2	GeV
Beam Current	62.5	mA
Pulse Length	2.86	ms
Bunch Frequency	352.21	MHz
Pulse Repetition Rate	14	Hz

Table 1.1: Beam parameters for the ESS linac Optimus+ design [38].

At beam energies above 1 GeV the neutron production rate in tungsten is constant at 2.1×10^{17} n/s/MW and as such great freedom in the choices of the parameters in equations 1.2 is available. This is a result of the stopping power of protons in the target at this energy being approximately constant and therefore the neutron production rate increases linearly with beam energy [39]. Therefore the changes to the beam parameters from the original design maintain the neutron flux of the original as long the average beam power is the same and the final beam

energy is above 1 GeV. As the protons pass through the target they loose energy through collisions with the tungsten atoms which can result in an intra-nuclear cascade of high energy particles such as protons, neutrons and pions which may cause further spallation processes. The target nuclei may the be in a highly excited state which results in the evaporation of particles of which neutrons form a large component. Many of the neutrons produced in these collisions are at a higher energy than required for neutron experiments and must be moderated to thermal energies using a liquid moderator before being sent to an experimental beam line. With the ESS average power of 5 MW an average neutron production rate of 1.05×10^{18}n/s is expected.

An advantage of using a machine with a high power long pulsed beam is the possibility to shape the initial proton beam shape prior to the target which will control the time structure of the emitted neutrons. This is particularly useful in experiments where the time arrival of neutrons is important in performing energy selection of the neutrons which is crucial in several different types of neutron experiment [40, 41].

In the future it may be possible to increase the neutron flux by increasing the beam power beyond 5 MW. However due to the increased beam current from the original design the scope for increasing the beam current is small as the 1.2 MW power couplers already present significant risk to the machine performance. Therefore any upgrade will likely be primarily in the introduction of additional RF cavities at the end of the linac in the beam transport to increase the beam energy.

1.2.2 The ESS Accelerator

At the heart of the ESS is its SCRF accelerator which is designed to deliver an average beam power of 5 MW, achieved by colliding a 2.86 ms long, 62.5 mA proton beam at an energy of 2 GeV with a solid tungsten target. This choice of design parameters is primarily driven by the goal of making ESS a 5 MW average power neutron source with a neutron yield 30 times high than the best performing current machine [36]. The current design is the so called Optimus+ design [38]; a general layout of which is given in figure 1.2.

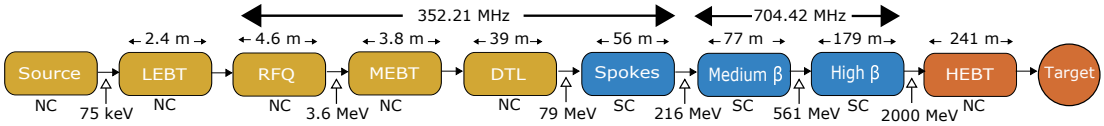

Figure 1.2: The Optimus+ layout of the ESS linac with NC section in warm colours and SC sections in cold colours and additionally labelled below each section [38].

Protons are produced at an ion source and transported through a Low Energy Beam Transport (LEBT) [42] to a four vane Radio Frequency Quadrupole (RFQ) [43] where the beam is bunched at 352.21 MHz before being passed through a Medium Energy Beam Transport (MEBT) [44]. At this stage, the final section of the NCRF linac is reached, which contains a Drift Tube Linac (DTL) [45]. From the DTL the beam goes into the SCRF section of the linac which consists of 26 Two-Spoke Cavity resonators [46], 36 Medium-β cavities and 84 High-β Cavities [47]. These cavities, operate at a cryogenic temperature of 2 K, which is achieved by immersing the cavities in liquid helium. Details of the SCRF cavities are shown in table 1.2. In addition details on how the power and accelerating gradient of each cavity varies along the linac is given in figure 1.3. After the final accelerating cavity the beam is passed through a High Energy Beam Transport (HEBT) before colliding with a solid tungsten target to produce the intended

Parameter	Spoke	Medium-β	High-β
Frequency (MHz)	352.21	704.42	704.42
Number of Cavities	26	36	84
Velocity Range (v/c)	0.42-0.58	0.58-0.78	0.78-0.95
Accelerating Voltage (MV)	5.74	14.3	18.2
Loaded Q	3×10^5	8×10^5	7.6×10^5
Dynamic Heat Load (W)	0.8	4.9	5.5
Max Forward Power (kW)	335	1100	1100
RF Source	Tetrode	Klystron	IOT

Table 1.2: Parameters for the ESS superconducting cavities [48].

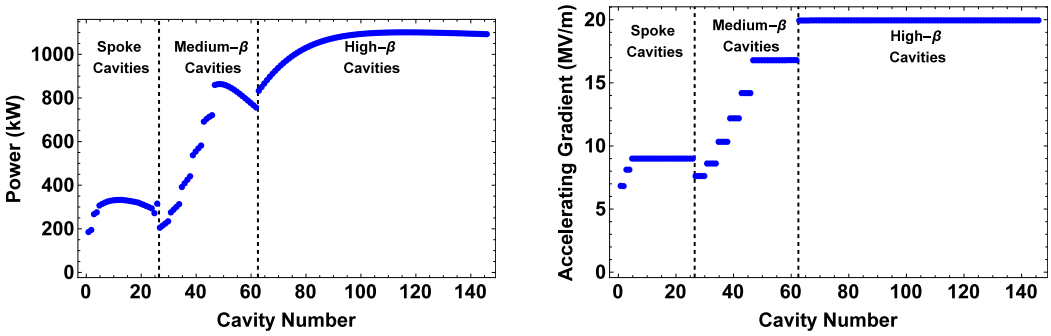

(a) Linac power profile.

(b) Linac accelerating gradient profile.

Figure 1.3: Power and accelerating profiles of the ESS superconducting linac.

neutrons.

The accelerator at ESS makes use of both well known technologies including an Radio Frequency Quadrupole (RFQ), a Drift Tube Linac (DTL) and elliptical SC cavities whilst also using new technologies such as SC spoke cavities.

1.3 Thesis Outline

When a bunch of charged particles traverse an accelerating cavity, it interacts not only with the accelerating mode but also with all other fields that can exist inside the cavity. Modes other than the accelerating mode in the cavity are referred to as Higher-Order Modes (HOMs) if they have frequencies greater than the accelerating mode. The interaction of the beam with HOMs can have a

significant impact on the beam, with the potential to cause instabilities which can result in degradation of the beam quality and/or the loss of a significant fraction of the beam. In addition, beam excited HOMs can also lead to additional energy being stored in the cavity, which when deposited into the cavity wall leads to heating. This heating can cause additional strain on the cryogenic system and if uncontrolled can potentially lead to cavities quenching, resulting in downtime for the machine.

Studying and understanding the impact of HOMs both on the cavities and the beam is therefore very important. By understanding the impact of HOMs, it is possible to implement counter measures to minimise their impact on the machine performance. Characterising the impact of HOMs, and developing mitigating strategies where appropriate is the main focus of this thesis.

This thesis is motivated by the question of the impact of HOMs on the performance of superconducting proton linacs, in particular the case of the ESS but also in a more general sense. The current understanding of the phenomena associated with HOMs in this instance was provided by [49, 50] and subsequently extended by [51, 52]. The earlier work focussed on the performance of the SNS and the SPL with the latter writing codes to simulate the expected behaviour in more general proton linacs. In each of these studies they found that the need for additional damping through HOM couplers was minimal particularly in the transverse plane, however they opted to proceed with them in place in order to completely mitigate the risk. In the SNS linac which is the only machine of this type which is operating the introduction of HOM couplers led to issue with multipacting which limited the machine performance [53]. The work performed by Ainsworth [52] formed the basis for the understanding of HOMs in the ESS and was included in the technical design report [36] forming the basis of their decision

to operate without HOM couplers.

The work contained in this thesis is therefore an extension of the work carried out in the studies carried out by [51, 52] on the possible impact of HOMs on the ESS linac and superconducting proton linacs in general. In particular for ESS this is due to the inclusion of the final cavity designs and also the most up to date linac layout at the time the work has been performed. Further the result found for ESS can be extended to a more general linac of this type such as the SPL [31] and Project-X [32]. This work is accompanied by a detailed study into the impact of manufacturing errors in the production of low-β elliptical cavities which are used in the ESS linac using several methods which can be extended alternative cavity designs.

In addition to analysis of the impact of HOMs on the beams in superconducting proton linacs this thesis focuses on the more fundamental behaviour of the wakefield which is formed by the HOMs. There is a particular focus on the behaviour of the wakefield in low-β cavities whilst two bunches are present simultaneously in a structure as is potentially the case for linacs with a high bunch frequency. Currently there is very little material which covers the issues which may arise due to this situation. As this is a fundamental effect in low velocity situations it could have an impact on other low energy cases such as electron guns and future proton linacs which may have higher cavity frequencies.

This thesis is arranged such that in chapter two the concepts RF acceleration and various RF parameters are introduced. In chapter three the concept of wakefields is introduced and decomposed into a modal summation. This is followed by chapter four which introduces the circuit model of accelerator modes and highlights its applications and limitations.

In chapter five the methodologies behind cavity simulations are introduced and

an analysis of the modal structure of the three ESS cavities is given in detail. The modal structure has then been analysed to identify modes which are likely to have a significant impact on the performance of the ESS. This was extended to include modes which may shift in frequency to lie on a harmonic of the bunch frequency for which the sensitivity to manufacturing errors was analysed using intensive simulations and the circuit model. These harmonics of the bunch frequency are also referred to as machine harmonics or machine lines.

Chapter six contains a detailed study of the impact of HOMs on the beam dynamic of the ESS paying particular attention to the impact of alignment issues in the transverse plane. In the longitudinal plane the analysis focuses on the impact of resonantly driven HOMs on the beam of ESS. The ESS elliptical cavities are not equipped with HOM damping ports—in contradistinction with most high power SCRF accelerators. The decision to exclude them was based on cost and the potential for negative effects on the machine operation—such as multipacting which is the resonate discharge of electrons at a material surface due to RF fields [53]. In this thesis I explore the impact of beam-excited HOMs on the beam quality.

It is also noted that, though there are no HOM damping ports, the fundamental power couplers are anticipated to provide some level of damping to the beam-excited HOMs. In order to understand the fundamental issues of HOMs in cavities the next chapter provides an introduction to the electromagnetic (EM) theory of cavities and to the main cavity types studied in this thesis.

Chapter 2

Introduction To Radio Frequency Cavities

In this chapter the fundamental principles of RF acceleration will be discussed with reference to the EM fields. Several important parameters pertaining to accelerating cavities are also given along with a brief discussion of their meaning and impact on cavity performance. In addition, different types of RF cavities, couplers and tuners are briefly discussed. The behaviour of the cavities is essential to understanding the impact of RF system on the beam of a machine and whether any additional precautions need to be taken to improve machine performance.

2.1 Maxwell's Equations

In classical EM, the behaviour of all electric and magnetic fields are described by Maxwell's equations [9, 54]. Maxwell's equations relate the electric field, $\vec{E}$ and magnetic field, $\vec{B}$ to their sources; charge density ρ and current density $\vec{j}$. In differential form Maxwell's equations are;

$$\vec{\nabla} \cdot \vec{D} = \rho, \tag{2.1}$$

$$\vec{\nabla} \times \vec{E} = -\frac{\partial \vec{B}}{\partial t}, \tag{2.2}$$

$$\vec{\nabla} \cdot \vec{B} = 0, \tag{2.3}$$

$$\vec{\nabla} \times \vec{H} = \vec{j} + \frac{\partial \vec{E}}{\partial t}, \tag{2.4}$$

where,

$$\vec{D} = \epsilon \vec{E}, \tag{2.5}$$

$$\vec{B} = \mu \vec{H}. \tag{2.6}$$

Here ϵ is the electric permittivity and μ is the magnetic permeability of the material. For EM fields in free space, with no sources, Maxwells equations can be written as

$$\vec{\nabla} \cdot \vec{E} = 0, \tag{2.7}$$

$$\vec{\nabla} \times \vec{E} = -\frac{\partial \vec{B}}{\partial t}, \tag{2.8}$$

$$\vec{\nabla} \cdot \vec{B} = 0, \tag{2.9}$$

$$\vec{\nabla} \times \vec{B} = \frac{1}{c^2} \frac{\partial \vec{E}}{\partial t}, \tag{2.10}$$

where c is the speed of light in a vacuum, given by $c = \frac{1}{\sqrt{\epsilon_0 \mu_0}}$. Taking the curl of equation 2.8 or 2.10 and applying the vector identity (shown for an arbitrary vector $\vec{A}$),

$$\vec{\nabla} \times (\vec{\nabla} \times \vec{A}) = \vec{\nabla}(\vec{\nabla} \cdot \vec{A}) - \vec{\nabla}^2 \vec{A} \tag{2.11}$$

two wave equations:

$$\vec{\nabla}^2\vec{E} - \frac{1}{c^2}\frac{\partial^2\vec{E}}{\partial t^2} = 0. \tag{2.12}$$

$$\vec{\nabla}^2\vec{B} - \frac{1}{c^2}\frac{\partial^2\vec{B}}{\partial t^2} = 0, \tag{2.13}$$

can be obtained. One set of solutions to these equations can be expressed as;

$$\vec{E}(\vec{r},t) = \vec{E_0}\ e^{i(\vec{k}_r.\vec{r}-\omega_r t)} \tag{2.14}$$

$$\vec{B}(\vec{r},t) = \vec{B_0}\ e^{i(\vec{k}_r.\vec{r}-\omega_r t)} \tag{2.15}$$

and equivalently in the frequency domain by taking the Fourier transform as

$$\vec{\tilde{E}}(\vec{k},\omega) = \vec{\tilde{E}_0}\ \delta(\omega-\omega_r)\delta(\vec{k}-\vec{k}_r) \tag{2.16}$$

$$\vec{\tilde{B}}(\vec{k},\omega) = \vec{\tilde{B}_0}\ \delta(\omega-\omega_r)\delta(\vec{k}-\vec{k}_r) \tag{2.17}$$

which represent a series of plane travelling waves travelling through free space. The phase velocity, v_p for both can be defined as,

$$v_p = \frac{\omega}{|\vec{k_r}|}. \tag{2.18}$$

2.1.1 Specific Cases

There are several specific cases where Maxwell's equations can be solved analytically for structures relevant to accelerator physics. Two cases which shed light on the essential physics for this thesis are the circular waveguide (beam pipe) and the circular pillbox.

The structures discussed here are axisymmetric, and hence the fields will be

found in cylindrical polar co-ordinates. In this co-ordinate system the Laplacian operator becomes:

$$\nabla^2 = \frac{1}{r}\frac{\partial}{\partial r}\left(r\frac{\partial}{\partial r}\right) + \frac{1}{r^2}\frac{\partial^2}{\partial \phi^2} + \frac{\partial^2}{\partial z^2}. \tag{2.19}$$

In each case there will be six equations that require solving, three for the electric field and three for the magnetic field.

2.1.2 Circular Waveguide

Consider a perfectly conducting circular waveguide which is infinitely long in the $\hat{z}$ direction and of radius r_0. To obtain the electric and magnetic fields for this structure the wave equations 2.12 and 2.13 need to be solved in cylindrical polar co-ordinates using equation 2.19. This set of equations has two distinct solutions; Transverse Magnetic (TM) with no axial magnetic field and Transverse Electric (TE) with no axial electric field. Only solutions for the longitudinal fields of both the TM and TE solutions will be given here, however full details can be found in [55, 56].

To solve the equation for the electric field in a TM mode, the boundary conditions [57] require that $E_z(r_0) = 0$. In addition we also require that the field remains physical, that is to say it does not become infinite within the region of interest. These boundary conditions lead to the solution [55]:

$$E_z^{m,n}(r, \phi, z, t) = E_0 J_m\left(\frac{j_{n,m} r}{r_0}\right)\cos(m\phi)\ e^{i(k_z z - \omega t)} \tag{2.20}$$

where J_m is the m$^{\text{th}}$ Bessel function of the first kind and $j_{n,m}$ is the n$^{\text{th}}$ zero of that function. The relationship between ω and k_z is known as the dispersion

relationship, and is given by:

$$\omega_{m,n}^2 = \left(\frac{j_{n,m}c}{r_0}\right)^2 + k_z^2 \tag{2.21}$$

where k_z is the wave number of the in the $\hat{z}$ direction. The phase velocity for all modes in a waveguide is greater than the speed of light; modes may only propagate if k_z is real, hence a cut-off frequency

$$\omega_c = \frac{j_{n,m}c}{r_0}, \tag{2.22}$$

exists below which an EM wave is unable to propagate. The dispersion curve for a cylindrical waveguide is shown in figure 2.1.

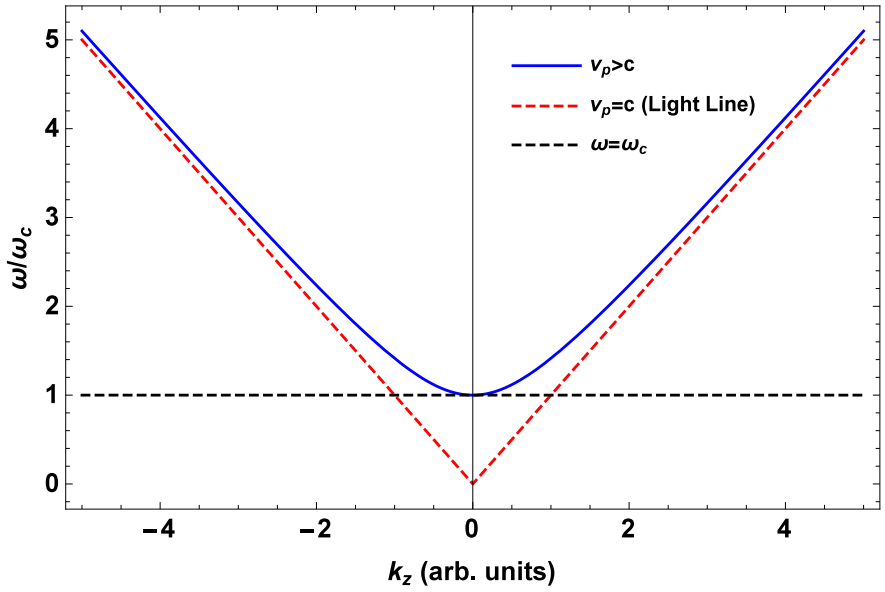

Figure 2.1: Dispersion curve for a cylindrical waveguide.

In a similar way the longitudinal magnetic field for TE mode can be calculated as,

$$B_z^{m,n} = B_0 J_m\left(\frac{j'_{n,m}r}{r_0}\right)\cos(m\phi)e^{i(k_z z-\omega t)} \tag{2.23}$$

where $j'_{n,m}$ is the n$^{\text{th}}$ zero of derivative of the m$^{\text{th}}$ Bessel function of the first kind.

For a TE mode the dispersion relationship is:

$$\omega_{m,n}^2 = \left(\frac{j'_{n,m}c}{r_0}\right) + k_z^2 \tag{2.24}$$

and the associated cut-off frequency is

$$\omega_c = \frac{j'_{n,m}c}{r_0}. \tag{2.25}$$

Beam pipes are circular waveguides which allow the beam to traverse and power to be coupled to the cavity. The presence of a waveguide between two structures allows power from one to flow to the other and can lead to multiple structures coupling together.

If the phase velocity of an EM wave in a structure is greater than the velocity of a charged particle which traverses it, then the charged particle will not be synchronous with the electric fields and hence is not accelerated. As a result, waveguides cannot be used to accelerate a beam. In order to reduce the phase velocity of the EM field discontinuities or dielectric media need to be introduced. This can be done by periodically loading a waveguide with disks which results in the formation of passbands within which a given frequency may propagate. This is evident in the dispersion curve for such a structure, an example of which is given in figure 2.2 and the intersection with the $v = c$ line is seen.

In the next section the introduction of end walls used to form a pillbox cavity will be discussed.

2.1.3 Circular Pillbox Cavity

The introduction of end walls to a waveguide results in the continuum of modes above a certain cut-off frequency being separated into a series of spacial har-

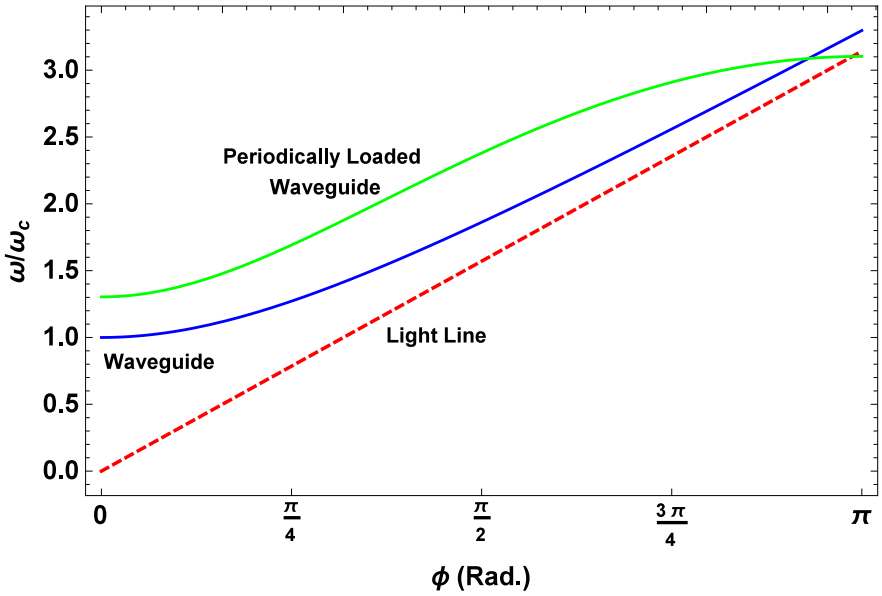

Figure 2.2: Dispersion curve for a cylindrical waveguide and for a periodically loaded waveguide.

monics. These spatial harmonics have a $v_p < c$ and can therefore effect charges which traverse the cavity. The simplest cavity is the closed pillbox cavity which has a well defined analytic solution and forms the basis for understanding the behaviour of more complicated structures. This analytic solution will be detailed in the following discussion.

Consider a cylindrical pillbox cavity of radius r_0 and length l can be constructed by using a circular waveguide and placing conducting end caps at, $z = 0$ and $z = l$. The fields can then be derived by applying appropriate boundary conditions to each component of the field. In a similar fashion to the waveguide we can divide the solutions into TE and TM modes. However, due to the introduction of the end caps, a continuous spectrum is no longer seen; instead a set of discrete cavity modes are found. The frequencies of the TM modes are given by [14, 58, 59]

$$\omega_{n,m,p} = c\sqrt{\left(\frac{j_{nm}}{r_0}\right)^2 + \left(\frac{p\pi}{l}\right)^2} \tag{2.26}$$

and for the TE modes

$$\omega_{n,m,p} = c\sqrt{\left(\frac{j'_{nm}}{r_0}\right)^2 + \left(\frac{p\pi}{l}\right)^2}. \tag{2.27}$$

The full expressions for the TM fields in a pillbox cavity are given by

$$E_z = E_0 \cos\left(\frac{p\pi z}{l}\right) J_m\left(\frac{j_{n,m}r}{r_0}\right)\cos(m\phi), \tag{2.28}$$

$$E_r = -E_0 \frac{p\pi r_0}{l j_{n,m}} \sin\left(\frac{p\pi z}{l}\right) J'_m\left(\frac{j_{n,m}r}{r_0}\right)\cos(m\phi), \tag{2.29}$$

$$E_\phi = E_0 \frac{mp\pi r_0^2}{r l j_{n,m}^2} \sin\left(\frac{p\pi z}{l}\right) J_m\left(\frac{j_{n,m}r}{r_0}\right)\sin(m\phi), \tag{2.30}$$

$$H_z = 0, \tag{2.31}$$

$$H_r = iE_0 \frac{m\omega_{mnp} r_0^2}{Z_0 c r j_{n,m}^2} \cos\left(\frac{p\pi z}{l}\right) J_m\left(\frac{j_{n,m}r}{r_0}\right)\sin(m\phi), \tag{2.32}$$

$$H_\phi = iE_0 \frac{m\omega_{mnp} r_0}{Z_0 c j_{n,m}^2} \cos\left(\frac{p\pi z}{l}\right) J'_m\left(\frac{j_{n,m}r}{r_0}\right)\cos(m\phi), \tag{2.33}$$

where $Z_0 (= \sqrt{\mu_0/\epsilon_0})$ is the impedance of free space. The commonly used nomenclature is $\mathrm{TM_{m,n,p}}$ where m represents the number of periods in the azimuthal direction, ϕ and n is the number of nodes in the longitudinal electric field as you move radially outward from the centre towards the cavity walls, excluding on-axis nodes. The final index p represents the number of half period variations in the z direction. The lowest frequency mode in a pillbox cavity is the $\mathrm{TM_{0,1,0}}$ mode which has a frequency that is independent of the cavity length.

For a mode to accelerate a charged particle traversing on-axis, the z component of the electric field must of course be non-zero on axis. As a result $\mathrm{TM_{m,n,p}}$ modes with m=0 are used to accelerate the beam. These modes are commonly known as monopole modes due to their rotational symmetry. $\mathrm{TM_{m,n,p}}$ modes m=1 are known as dipole modes and modes with m=2 as quadrupole modes. Provided the

beam is steered close to the electrical centre of the cavity, consideration of dipole and quadrupole modes will be most important in a transverse beam dynamics analysis. Typical field profiles for each type of mode are given in figure 2.3.

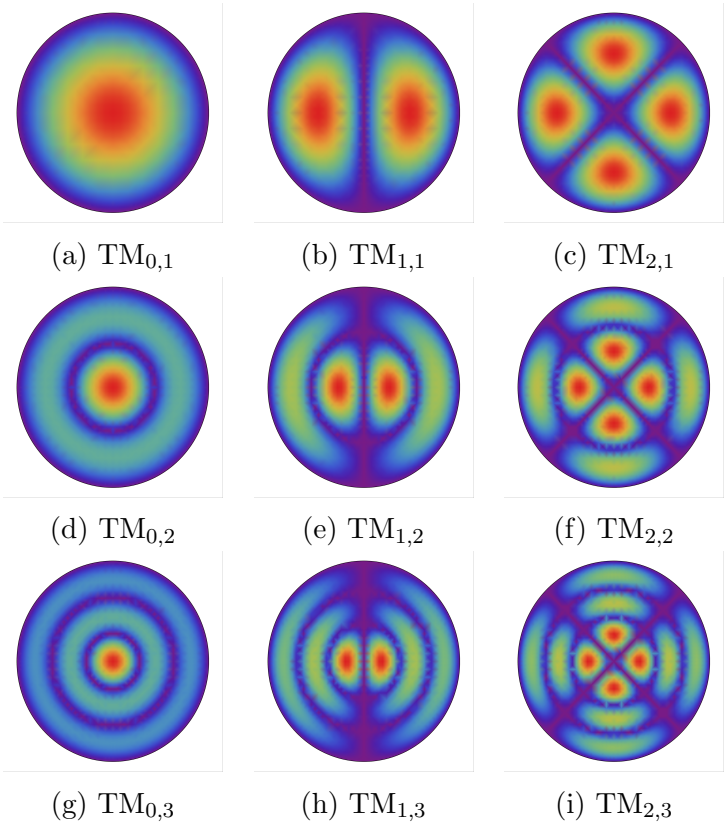

(a) $TM_{0,1}$ (b) $TM_{1,1}$ (c) $TM_{2,1}$

(d) $TM_{0,2}$ (e) $TM_{1,2}$ (f) $TM_{2,2}$

(g) $TM_{0,3}$ (h) $TM_{1,3}$ (i) $TM_{2,3}$

Figure 2.3: E_z field profiles for the first three $TM_{m,n}$ monopole (m=0), dipole (m=1) and quadrupole (m=2) modes.

Typically a $TM_{0,1,0}$ mode is used as the accelerating mode and all other modes are referred to as higher-order modes (HOMs). In order to allow a beam to pass through and for power to be introduced into the cavity, openings must be introduced. The addition of irises changes the field profiles significantly and as a result pure TE or TM modes are no longer present. However, the modes found are often referred to as TE-like or TM-like. Further the introduction of irises can lead to cells in close proximity coupling and significantly complicates the modal structure of multi-cell RF cavities which will be discussed in section 2.4.3. In ad-

dition, these openings make an analytic analysis impractical and hence numerical techniques or equivalent circuit models are employed. There are many parameters used to characterise the performance of an RF cavity, several of which will now be discussed.

2.2 Cavity Radio Frequency Parameters

There are several parameters which are used to characterise the behaviour of RF accelerating structures, the definitions of which can be found in [11, 12, 14, 60] for example.

When a charged particle of charge q traverses a cavity of length L with a velocity $\beta = v/c$, it experiences an accelerating voltage, which is given by,

$$V_{acc} = \int_0^L E_z(r,z)e^{-i\omega_n z/\beta c}dz \tag{2.34}$$

where $E_z(r,z)$ is the $\hat{z}$ component of the electric field and ω_n is the angular frequency of mode n respectively. The exponential term in the integral accounts for the time it takes the particle to traverse the cavity and also the oscillation of the field in that time. The effect of field oscillation can be characterised by the transit-time factor

$$T = \frac{\Re\left[\int_0^L E_z(r,z)e^{-i\omega_n z/\beta c}dz\right]}{\left|\int_0^L E_z(r,z)dz\right|}. \tag{2.35}$$

With a field map for a cavity it is a simple task to calculate the accelerating voltage through numerical integration. In practise the acceleration for a cavity is usually given as an acceleration gradient, $E_{acc} = V_{acc}/L$ in units of MV/m where L is the active length of the structure.

The stored energy, U_n in a mode is calculated from the peak EM fields as

$$U_n = \frac{1}{4}\left(\epsilon_0 \int_V |\vec{E}|^2 \, dV + \mu_0 \int_V |\vec{H}|^2 \, dV\right), \tag{2.36}$$

where, the integral is over the entire volume enclosed by the cavity when all fields are at peak values. However the energy stored in the electric and magnetic fields at resonance is equal [61] and hence;

$$U_n = \frac{1}{2}\epsilon_0 \int_V |\vec{E}|^2 \, dV = \frac{1}{2}\mu_0 \int_V |\vec{H}|^2 \, dV. \tag{2.37}$$

The walls of an accelerating cavity, even in a SCRF cavity, have finite RF conductivity [62] and as a result energy will be dissipated into the cavity walls. The power lost in the walls of an accelerating structure is given by,

$$P_c = \frac{1}{2}R_s \int_S |\vec{H}|^2 \, dS, \tag{2.38}$$

where the integral is of the peak $\vec{H}$ field taken over the cavity walls and R_s is the surface resistance of the walls. From equations 2.37 and 2.38 the Quality Factor Q_0, of the cavity can be defined as

$$Q_0 = \frac{U\omega}{P_c}. \tag{2.39}$$

Q_0 is related to the number of RF cycles it takes for stored energy to dissipate in the cavity walls. Therefore cavities with a high Q_0 can store energy for long periods with lower losses than low Q_0 structures. The Q_0 takes into account losses in the cavity surface, however addition losses—through couplers and ports—can be included in an additional external quality factor, Q_{ex}. The combined effect of

the Q_0 and Q_{ex} is known as the loaded quality factor, Q_L defined as

$$\frac{1}{Q_L} = \frac{1}{Q_0} + \frac{1}{Q_{ex}}. \tag{2.40}$$

The Q_L of the cavity is closely related to the filling time,

$$t_f = \frac{2Q_L}{\omega} \tag{2.41}$$

which is the amount of time required for the field to drop by a factor of $1/e$

Another important quantity to consider when studying an accelerating structure is the shunt impedance, R_a, which is given by

$$R_a = \frac{V_{acc}^2}{2P_c}. \tag{2.42}$$

The shunt impedance represents how efficiently a mode can accelerate a beam as a high shunt impedance implies that a lower input power is required per unit of acceleration. For an accelerator, a high R_a for the accelerating mode is required and a low R_a is desirable for all other modes.

When a charged particle traverses a cavity it looses a fixed amount of energy per unit charge squared; this is known as the loss factor. The loss factor is usually decomposed as

$$k_{\parallel} = \sum_n k_{\parallel,n} \tag{2.43}$$

where $k_{\parallel,n}$ is the modal loss parameter and is amount of energy lost into each mode n, per charge squared and is given by

$$k_{\parallel,n} = \frac{|V_{acc,n}|^2}{4U_n}. \tag{2.44}$$

The loss parameter is usually given in units of V/pC/m where it is normalised to the cavity length and is related to the fundamental theorem of beam loading discussed in section 3.1.2 and detailed in appendix A. By applying the Panofsky-Wenzel theorem [63] the transverse loss parameter, $k_\perp$ can be defined as

$$k_{\perp,n} = \frac{k_{\parallel,n}c}{\omega_n}. \tag{2.45}$$

The geometric parameter R/Q is defined as

$$\left(\frac{R}{Q}\right) = \frac{1}{r^{2m}}\frac{R_a}{Q_0} = \frac{1}{r^{2m}}\frac{|V_{acc}|^2}{\omega U} \tag{2.46}$$

where the R/Q is independent of the surface resistance and r is the radial offset of the integration axis for V_{acc}. This parameter can be used to directly compare the accelerating efficiency of very different cavity shapes.

Finally the transverse kick factor [64], which allows the loss parameter to be expressed independent of radial offset r, is defined as

$$K_n = \frac{c}{\omega_n L}\frac{1}{r^{2m}}k_{\parallel,n}. \tag{2.47}$$

where L is the cavity length. The kick factor is normalised in this way as to first order it makes it independent of offset which is sufficient for a beam which is close to the axis. Both the loss factor and kick factor are key parameters when investigating the wakefield of which more details are given in chapter 3.

The parameters discussed in this section are key to understanding the properties and performance of RF cavities. In the next section SCRF cavities are discussed and typical values of the parameters discussed in this section are given.

2.3 Structure Types

In general there are two major types of cavity operation which are used these are; travelling wave (TW) and standing wave (SW). In a TW structure power flows through the cavity at the group velocity ($v_g = \frac{\partial \omega}{\partial k}$) structure and the power decays along the length of the cavity with any remaining power dissipated at an external load. Whereas in a SW cavity a standing wave is set up due to multiple internal reflection from the cavities end walls which result in energy being stored for long periods in the cavity.

A TW structure can be made by periodically loading a circular wavguide with irises to reduce the phase velocity of the RF and to allow it to couple to the beam. By attaching an input and output coupler to a loaded waveguide it can become an accelerating structure. As an RF pulse moves along the TW structure the RF power falls at a constant rate and this is known as a constant impedance structure. However, by varying the iris of the disks the group velocity from cell-to-cell can be decreased to obtain a constant accelerating gradient in each individual cell, these structures are known as constant gradient structures and they have an increased efficiency compared to constant impedance structures. A TW structure allows any frequency that lies in one of its passbands to propagate.

To make a SW structure the end of a circular waveguide is closed with conducting end-caps which cause reflection to allow a SW field to be produced. However as the beam and power need to be able to enter and leave the cavity irises must also be present in the end-caps. In the case of an SW structure only a finite number of spatial harmonics are able to exist due to cancelling of the EM fields due to the multiple internal reflections. This means only very specific frequencies of RF power can be coupled to the structure.

Both TW and SW structure work in a mode of a specific electric field phase

advance per cell, in the case of TW this is often the $2\pi/3$ mode which gives the maximum shunt impedance. However for a SW structure it can be shown that for all phase advances except $\phi = 0, \pi$ that the shunt impedance is exactly half that of a TW structure. This is consistent with the naive view that a SW is the sum of two TW's of which only one may accelerate [65], however for $\phi = 0, \pi$ the shunt impedances can be shown to be equal. Therefore most SW linacs operate in the π-mode with some operating in the $\pi/2$-mode with side coupled cells such that it appears to the beam as a π-mode.

A major factor that must be considered is the difference in how the TW and SW structures are filled with RF power. A TW structure is filled in space which means the power propagates along the structure filling one cell after another with the fill time determined by the group velocity of the RF in the structure. In a SW structure the field slowly builds up after many internal reflections which takes much longer to fill than a TW structure and there is also a considerable amount of power reflected from the structure until the beam is present. As a result for short pulses TW structures are much more efficient, however for long pulses both SW and TW may be optimised to have similar efficiencies. This is complicated by the fact that it is possible to use superconducting materials to make the SW which means that a SW structures has additional benefits for long pulse operation.

One final consideration is the velocity of the beam, in a typical lepton accelerator $\beta = 1$ for a significant proportion of the machine and each cell of an accelerator is identical. However for a hadron machine $\beta < 1$ and the velocity of the beam can change appreciably within a structure which for a TW cavity can be a particular problem due to the large number of cells which requires the cell shape to continually vary along the linac to keep the beam synchronous with the accelerating mode. Whereas for a SW structure several families of cavity are

often used each with specific velocity acceptances, which due to the small number of cells is quite large.

Comparisons between the cost and efficiency of SW and TW structure have and will continue to be debated with each new accelerator, examples of the analyses carried out include [65, 66].

As a result of ESS being a long pulse, high power proton machine the choice of SW structures is clearly favoured particularly when the use of SCRF cavities is possible. SCRF structure will be discussed in the next section.

2.4 Superconducting Cavities

The SCRF section of the ESS linac is the main focus of this thesis and in this section a brief overview of superconducting effects related to RF will be given, as well as an overview of the types of SCRF cavity used at ESS.

2.4.1 Introduction To SCRF

An SCRF cavity is one which is constructed from a material which is able to transition into the superconducting state when cooled below a critical temperature, T_c [62]. Below T_c, the DC conductivity of the material drops to zero, however for an AC current a very small residual resistance that is analogous to inertia will remain present due to the finite mass of the conducting electrons. Typically the T_c of a superconductor is of the order of 10 K, with niobium—commonly used in SCRF—having a T_c of 7.2 K.

The AC resistance of a superconductor can be written as:

$$R_s = R_{BCS} + R_0 \tag{2.48}$$

where R_0 is the residual resistance and R_{BCS} is the frequency-dependent resistance describe by the Bardeen, Cooper, Schrieffer (BCS) theory [14, 62, 67]. BCS theory allows the electrons in a material to interact with each other and also with the crystal lattice of the niobium. As a result, electrons can be attracted to each other through perturbations in the lattice leading to electrons becoming paired. These pairs of electrons are the well known Cooper pairs, where two electrons of opposite spin become coupled and behave as boson-like particles with zero spin and as a result obey Bose-Einstein statistics. This transition allows for a macroscopic number of Cooper pairs to drop into the ground state where the binding energy of the Cooper pair is greater than the kinetic energy of the electrons. The resistance due to the BCS theory at temperatures below $T_c/2$ is given by

$$R_{BCS} \propto \frac{1}{T} f^2 e^{-1.76 T_c/T}. \tag{2.49}$$

The BCS resistance increases with the square of the frequency and as a result it is optimal for SCRF cavities to operate at frequencies which lie below 4 GHz [14]. The resistance also decreases exponentially as a function as temperature as at lower temperatures more electrons pair and collapse into the ground state. This phenomena can be explained using the two-fluid model [68] where two possible states, normal conducting and superconducting are both present simultaneously.

The residual resistance of a superconducting material is finite due to the quality of the material and the manufacturing techniques employed. Resistance is caused by the presence of impurities and/or discontinuities in the crystal lattice of the material. Throughout the manufacturing process many techniques are used and these can result in contamination of the material with hydrides or oxides—for example due to chemical treatments and exposure to air [69]. In addition it is also possible to pin magnetic flux to the material resulting in surface currents

which dissipate energy. These effects limit the minimum surface resistance of an SCRF cavity to $\mathcal{O}(n\Omega)$ which is still three orders of magnitude lower than that of a NCRF structure.

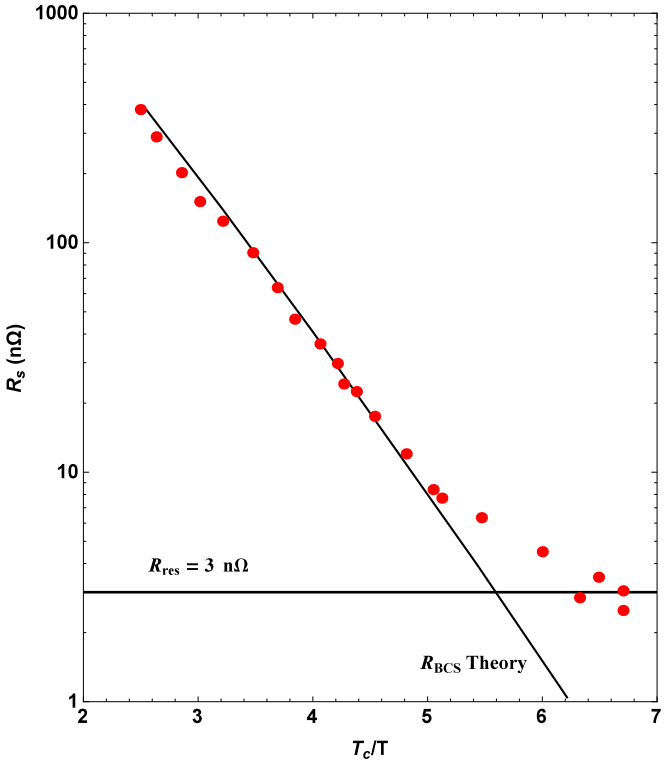

Figure 2.4: The surface resistance of a niobium TESLA cavity [16].

A typical SCRF cavity is made from bulk niobium which is cooled to a temperature of about 2 K and operates at a frequency less than 4 GHz. These frequencies and temperatures are chosen as a balance between minimising the surface resistance of the cavity to prevent quenching and having a high accelerating gradient to minimise the amount of space occupied.

SCRF structures are preferred to NCRF structure in applications where continuous wave (CW) or high duty cycles are required due to the reduced power consumption. However, the reduced power loss is partially offset by the efficiency

of the cryogenic system which is unable to exceed the Carnot efficiency:

$$\eta_c = \frac{T_{low}}{T_{high} - T_{low}} \tag{2.50}$$

where T_{low} is the target temperature and T_{high} is the surrounding temperature. For a system at the cryogenic temperatures of 2-6 K required the Carnot efficiency is 1-2% which cancels much of the gain in terms of surface resistance. Once the cooling efficiency and other 'lossy' processes are taken into account, the efficiency of SCRF and NCRF are similar with a factor of approximately two gain in favour of the SCRF cavities. For example at a centre of mass energy of 500 GeV the predicted wall power requirement for CLIC is 272 MW [70] and for the ILC it is 215 MW [18] which is a 21% difference.

A key limitation of superconducting materials is their critical fields at which the cooper pairs are broken and they transition into the normal conducting state. In most cases it is the critical magnetic field H_c which is reached and for an SCRF structure the magnetic field is linearly proportional to the surface magnetic field. Hence the maximum gradient is limited by the surface magnetic field of the structure.

The most common material used is niobium, which as a type-II superconductor and it does not have a well defined critical field due to a transitional state which exists with surface fields between $H_{c1} = 160$ mT and $H_{c2} = 300$ mT due to the appearance of NC vortices [71]. This means that it is theoretically possible for niobium to support fields up to H_{c2}, however in practise the appearance of vortices gives rise to heating which can result in the cavity quenching. Typically cavities are designed to have $H_{pk} < 180$ mT to avoid excessive heat load and minimise the risk of quenching. Taking the super-heating field, $H_{sh} = 230$ mT the maximum obtainable accelerating gradient is approximately 55 MV/m [14, 72]. In prac-

tise however the highest gradient obtained is for a single cell and is ∼52 MV/m achieved using the Reentrant cavity at Cornell University, Ithaca, New York, USA [73]. For structures with multiple cells this limit is still valid, however the more complicated geometry and required construction procedures result in significantly lower fields being practical with the maximum obtained of order 45 MV/m [74].

2.4.2 Elliptical Cavities

Elliptical Cavities form the main subgroup of SCRF cavities [75, 76]. They are known as elliptical cavities due to their shape which is composed of two ellipses joined by a common tangent, as illustrated in figure 2.5. This shape is preferable

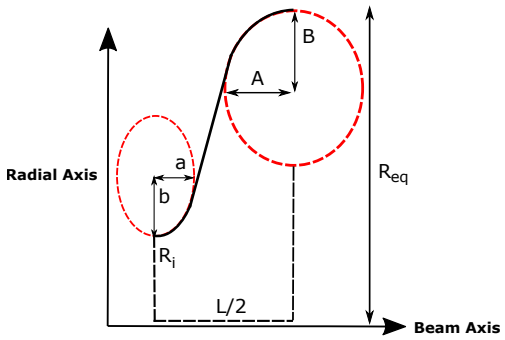

Figure 2.5: Schematic of the cross-section of an elliptical half cell showing the equator radius R_{eq}, iris radius R_i, half cell length $L/2$, iris ellipse eccentricities a and b and the equator ellipse eccentricities A and B.

as it reduces both multipacting and field emission whilst retaining mechanically rigid. The reduction in these detrimental effects is in part due to the reduced surface fields in the design, which also means that the Q_0 of the cavity is increased resulting in improved performance. To achieve the maximum possible acceleration the cell length must be tuned so that a particle traverses a cell in phase with the

accelerating field. This can be achieved by setting the cell length to be

$$L = \frac{\beta_g c \pi}{\omega} = \frac{\beta_g \lambda}{2} \tag{2.51}$$

where λ is the wavelength of the accelerating field and β_g is the geometric or design β of the cavity. As the velocity of the particle is increased the length of the cavity also increases meaning low-β cavities are significantly shorter than high-β cavities of the same frequency and type.

For proton machines β is typically in the range 0.3 to 1.0 and the velocity of the beam is changes appreciably between cavities. In principle this means for optimum performance a cavity designed specifically for each position in the linac is required, this is impractical and hence one cavity is used over a wide velocity range with reduced accelerating efficiency.

2.4.3 Multi-Cell Cavities

In most accelerators, space is at a premium so single cell SCRF cavities are not a viable option due to each individual cell requiring it's own power and HOM couplers which as well as taking up space increase the cost of the machine. The active accelerating length divided by the total space taken up by the structure and all of its equipment is known as the packing factor [13]. Ideally accelerators would have a packing factor of one, however each structure requires its own cryomodule, power and HOM couplers meaning SCRF cavities take up a space significantly larger than the active length of the cavity. This results in a reduced packing factor and more space being required per MeV of energy gain. A low packing factor can be increased by using cavities with multiple cells which use the same cryomodule and couplers. Multiple cavities are also placed in the same cryomodule, however

gaps must still be left for other components such as diagnostics, magnets and bellows meaning the packing factor is still usually significantly less than one. For example the ESS SCRF linac is 312 m long with approximately 133 m of active cavity length corresponding to a packing factor of 0.43. A multicell structure is illustrated in figure 2.6. Adding more cells increases the active length of the

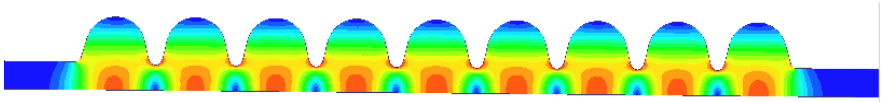

Figure 2.6: Image of a nine cell 1.3 GHz TESLA cavity drawn using HFSS with the magnitude of the electric field plotted with the beam axis in the horizontal direction. Regions of high field are in red and low field in blue.

cavity whilst allowing the cavity to be supplied by a single power coupler and a single set of HOM couplers. This reduction in the amount of equipment reduces the amount of space required whilst also being economically beneficial.

As a result of having multiple cells the mode structure of the accelerating structure becomes significantly more complex due to the cells coupling together [11]. This results in the original modes splitting into passbands each with the same number of modes as cells. In addition, to achieve the maximum possible acceleration the field must be flat which requires the end cells to be at a different frequency due to coupling between the cavity and the beam pipe.

Although this increases the packing factor significantly, it also presents several issues: firstly as a result of the iris between cells there is a region of high field which limits the accelerating gradient compared to a single cell. Secondly, it is possible for 'trapped modes' to exist inside a cavity, meaning damping may not be possible using HOM couplers [12]. This could lead to beam excited fields also known as wakefields causing the beam quality to degrade or the cavity to heat. And finally obtaining field flatness is more difficult with multiple cells and often the performance is limited by the worst cell in the cavity.

Trapped HOMs, as well as power consumption limit the maximum number of cells in a $\beta = 1$ cavity. However in a $\beta < 1$ cavity increasing the number of cells also results in a reduction of the velocity acceptance which means more types of cavities could be required to cover the whole velocity range of the accelerator. This is illustrated in figure 2.7 for several cases where an ideal sinusoidal field has been used.

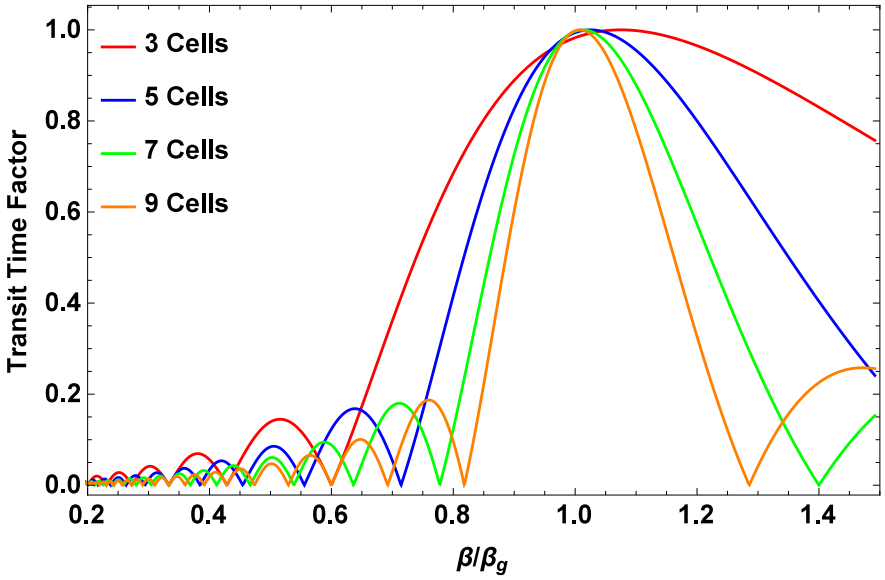

Figure 2.7: Transit time factor (equation 2.35) as a function of β relative to β_g for an ideal cavity of fixed length with a sinusoidal field. The number of half periods of the sinusoid equates to the number of cells.

For low-β structures, cavities of the Transverse Electromagnetic (TEM) type are usually used and at ESS these cavities will be spoke cavities which are discussed in the next section.

2.4.4 Spoke Cavities

Spoke cavities [13, 23, 69, 77] are a variant of the TEM resonator which consists of a series of stacked half wave resonators with neighbouring inner conductors rotated at 90 degrees with respect to each other. In structures with multiple

spokes passbands are seen similar to those in elliptical cavities, however as spoke cavities are TEM resonators, it is the number of conductors which defines the number of modes. Thus, a two-spoke cavity—such as those at ESS—will have two modes in each passband. In the accelerating band only the 0 and π modes will be present.

The modes present in a spoke cavity are strongly coupled (20-30%) through the magnetic field which leads to a mechanically robust structure where the modes are less sensitive to geometrical errors than those in elliptical cavities. Further, spoke cavities also have a wide velocity acceptance which makes them particularly useful in the early stages of acceleration in ion machines. Many spoke cavities

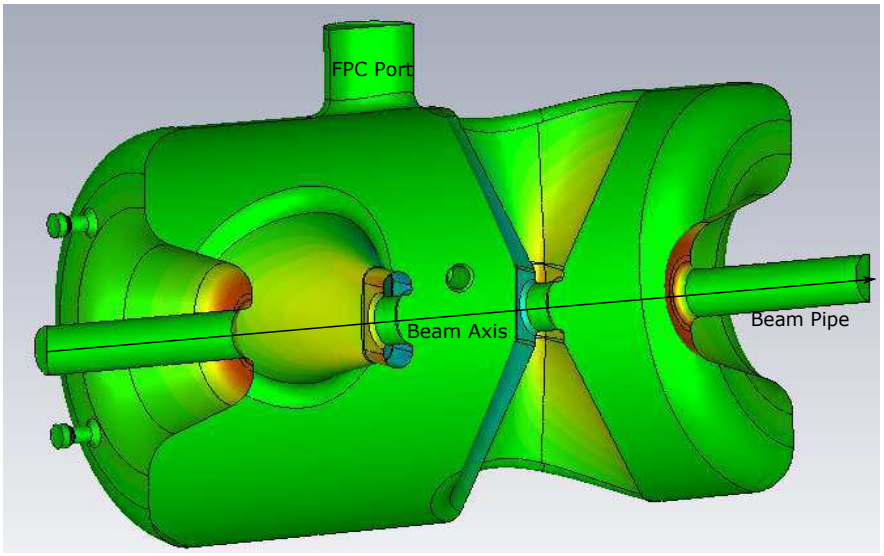

Figure 2.8: The ESS spoke cavity modelled in CST MWS [78] showing the magnitude of the surface electric field with high fields in red and low fields in green.

have been developed for various velocity and frequency regimes, however none have yet been installed in a operating facility. It is expected that ESS will be the first major facility to operate using spoke cavities when it begins operation in 2019.

2.5 Power Coupling

For an accelerating cavity to be able to accelerate a beam, EM power must be supplied to the cavity. The power is usually delivered to the cavity from a power source (Magnetron, Klystron, IOT, etc.) via a series of waveguides from which it is coupled into the cavity. The coupler [79] itself can take one of two forms either waveguide or coaxial depending on the application.

A waveguide coupler is usually used in high frequency structures due to its size and the fact that it can be cooled using water channels. As they are used at high frequency they are typically used in NC structures.

Coaxial couplers are beneficial for use in lower frequency cavities due to their reduced size and also where a variable coupler is desired, as the antenna penetration depth can easily be changed. Coaxial couplers are more complex than waveguide couplers due to requiring a waveguide-to-coax transition and complex cooling systems. Further high fields on the antenna can result in multipacting which can adversely effect the performance. Examples of both the waveguide and coaxial coupler types are shown in figure 2.9. Power couplers for SCRF cavities

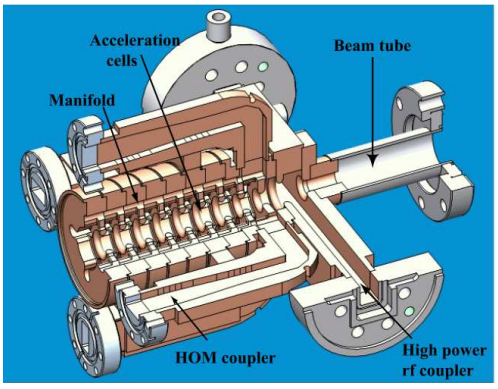

(a) Waveguide coupler [80].

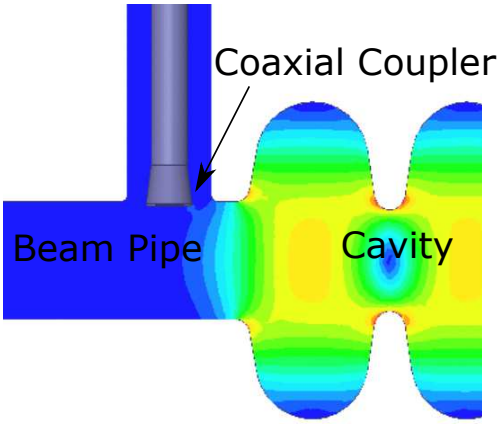

(b) Coaxial coupler.

Figure 2.9: Examples of waveguide and coaxial coupler types.

usually have Q_{ex} values several orders of magnitude below the Q_0 of the cavity. In addition to reducing the Q_L of the accelerating mode so the system is matched the power coupler can also couple to other modes providing damping. However, they are not specifically designed for this purpose and additional HOM couplers are in most cases required.

The fundamental power couplers (FPC's) at ESS will be coaxial [47, 81], with different designs for the spoke and elliptical cavities. The other type of couplers that can be employed are HOM couplers which are discussed in the next section.

2.6 HOM Couplers

Due to the high quality factors ($Q \sim 10^{10}$) associated with SCRF cavities beam-excited HOMs are present for many RF cycles and may affect trailing bunches. As a result of this, HOMs are usually actively damped through the use of HOM couplers [82]. There are several types of HOM couplers which include waveguide, coaxial and beam pipe couplers.

Waveguide couplers involve the extraction of HOM fields using a waveguide which has a cut-off frequency above that of the accelerating mode. By having the accelerating mode below cut-off, the accelerating mode will not couple efficiently to the waveguide. These type of couplers tend to be quite large and for low frequency cavities are impractical. For high frequency structures such as those designed for the NC accelerator known as CLIC [70], waveguide couplers are well suited.

Coaxial HOM couplers use a coax line with an antenna at the end to couple out HOMs [69]. The antennas can take the form of either a capacitive gap to couple to the electric field or an inductive loop to couple to the magnetic field. They avoid coupling to the accelerating mode through the use of a rejection

filter. Coaxial couplers have the advantage of being small even at low frequencies, however multipacting and field emission present significant issues. Examples of the both the coaxial and HOM couplers are shown in figure 2.10.

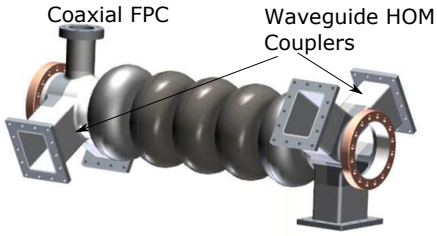

(a) Waveguide HOM coupler for BESSY-VSR cavity [83].

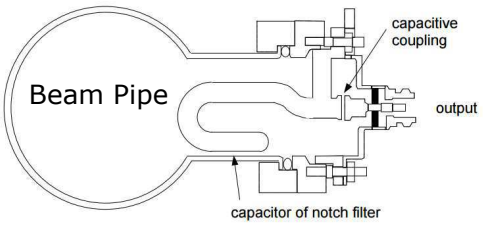

(b) Coaxial HOM coupler for the TESLA cavity [16].

Figure 2.10: Examples of waveguide and coaxial HOM coupler types.

Beam pipe couplers make use of HOMs being above the beam pipe cut-off frequency which allows them to propagate down the beam pipe which can then be loaded with a lossy material such as ferrite. Sections of the beam pipe are then lined with an absorbing material such as ferrite which damps the mode [84]. Beam pipe couplers are advantageous when high powers need to be dissipated, however if a mode is below or near cut-off their damping effects can be significantly reduced.

These types of couplers are generally used in a SCRF machine, however ESS has opted to forgo their use. This decision was taken as HOMs have been shown to have little impact on the beam unless resonantly excited by the beam [85]. Resonant excitation of a HOM can be prevented by designing the cavity with these aims in mind and the placing quality control measures to prevent manufacturing errors causing the HOM frequencies shifting toward the machine resonances. Further to this shifts caused when tuning the cavity frequency during operation must be accounted for, this tuning is done using mechanical systems to deform the cavity and is discussed next.

2.7 Cavity Tuners

When a cavity is evacuated and cooled down to cryogenic temperatures there can be significant shifts in the frequency of the accelerating mode. This is corrected using a mechanical tuner [12, 69]. The tuning range is usually reasonably small, for the ESS elliptical cavities the tuning range is ±300 kHz.

During operation the cavity will be filled with large amounts of RF power which results in radiation pressure on the inside of the cavity walls. This causes the frequency of the accelerating mode to vary and is known as Lorentz detuning [86, 87]. The pressure on the wall of the cavity is given by

$$P = \frac{1}{4}\left(\mu_0|\vec{H}|^2 - \epsilon_0|\vec{E}|^2\right). \tag{2.52}$$

The pressures deform the cavity wall, tending to act outward near the equator and inward near the iris resulting in a frequency shift which is given by

$$\Delta f = K_L V_{acc}^2. \tag{2.53}$$

K_L is the Lorentz detuning coefficient and is usually of the order 1-3 Hz/(MV/m)^2 for a SCRF elliptical cavities [88, 89]. The Lorentz detuning can either be damped through mechanical supports or actively compensated using piezo-tuners. At ESS a Saclay V-type piezo-tuner will be used [36, 90]. In NCRF structures Lorentz detuning is less of an issue as the cavity walls can be made much thicker and are hence more mechanically rigid.

An unavoidable consequence of the cavity deformation is that the frequency of HOMs as well as the accelerating mode can shift significantly. As a result this shift must be considered when setting limits on the HOM frequency separation

from harmonics of the bunch frequency (352.21 MHz) at the design stage.

In summary, the concept of RF accelerating structure has been introduced starting from Maxwell's equations and finishing with a derivation of the fields inside a pillbox cavity. Several important parameters in characterising the behaviour of RF cavities were also discussed in detail. Further, the effects of changing the cavity shape to allow the beam to pass through and to improve performance have also been discussed before introducing cavity couplers and tuners.

The concepts discussed here will be extended in the next chapter to introduce the concept of the beam-excited wakefield and its potential implications on the beam dynamics of an accelerator.

Chapter 3

Wakefields and Impedances

The wakefield is an important concept when considering the performance of an accelerator. When a beam passes near a discontinuity or past a surface of finite resistance the beam will excite an EM field, known as the wakefield. The excited wakefield acts back on the bunch and may influence subsequent bunches. It is well known that wakefields can cause beam degradation and/or beam instabilities which may result in reduced machine performance [91].

In this chapter the basic concepts and definitions of the wakefield will be given. The potential implications of the wakefield on the beam will be discussed. In addition the concept of the sum wakefield will also be discussed as well as the idea of impedance and its relationship to the wakefield.

3.1 Definition and Basic Concepts

Consider a particle of charge q moving in free space with velocity β as a fraction of the speed of light in the $\hat{z}$ direction, henceforth referred to as the drive charge. In the case where $\beta \approx 1$ the electric and magnetic fields will be confined to the plane perpendicular to the charges motion, with an opening angle given by

$1/\gamma$ [9], where γ is the Lorentz factor given by [92]

$$\gamma = \frac{1}{\sqrt{1-\beta^2}}. \tag{3.1}$$

In the limit $\beta \approx 1$ for a charge in free space there will be no fields ahead or behind the drive charge as a result of the principle of causality [92], which states that information cannot travel faster than the speed of light through space. Consequently a test charge travelling some distance behind or in front of the drive charge with the same velocity does not experience a force due to the EM fields of the drive charge.

Now consider the same situation, where this time both charges are moving on-axis within the walls of a perfectly conducting pipe of circular cross-section. The field from the drive charge will cause image charges to form on the metallic wall of the cylinder [93], these image charges will move with the same velocity as the drive charge. As a result the test charge will experience no field from either the drive charge or image charges. However, if the perfectly conducting walls are replaced with a material of finite conductivity the image charges will lag behind the drive charge due to the finite resistance making their mean free path finite. These lagging image charges in the resistive walls cause field to be present behind the drive bunch, which are know as the resistive wall wakefield, which will be experienced by the bunch [91].

A similar situation can be envisaged if instead of a finite resistance, a discontinuity is introduced to the walls of the vacuum chamber (collimator, cavities bellows etc.) [60]. These discontinuities cause the EM fields from the drive bunch to scatter, and results in a wakefield. This field can kick the trailing test charge and is known as the geometric wakefield.

The wakefield can be split into two very distinct regimes, the short range

wake acting over the bunch length and the long range which acts over many bunch lengths. The short range wake is usually associated with effects within a single finite length bunch such as the head-tail instability [91]. Whereas the long range wakefield is generally considered as the field which is able to impact on subsequent trailing bunches. The derivations and definitions in the following sections can be found in many texts notably [60, 94–96].

3.1.1 The Catch-Up Problem

The fixed value of the speed of light in a vacuum leads to several interesting phenomena related to the topic of wakefields. If a relativistic drive charge is travelling along the z-axis past a metallic discontinuity positioned a distance, b off the z axis as illustrated in figure 3.1. A test charge travelling a distance, s behind the drive charge along the same path does not experience the scattered field until it reaches a position z_c known as the catch-up distance given by

$$z_c = \frac{b^2 - s^2}{2s}. \tag{3.2}$$

For small values of s, z_c can be very large. In the case where γ is finite the catch up distance for the charge to experience its own field is given by $z_c \approx b\gamma$ [60]. This phenomena is commonly known as the catch-up problem and results purely from the fact that the speed of light is fixed and hence there is a finite delay in information transfer to the test charge. For the wake potential to be useful as a Greens function the wake potential must be accurate for values of s which is small compared to the bunch length σ. As a result in simulations the mesh used to model the cavity must have a length that is fractions of the bunch length.

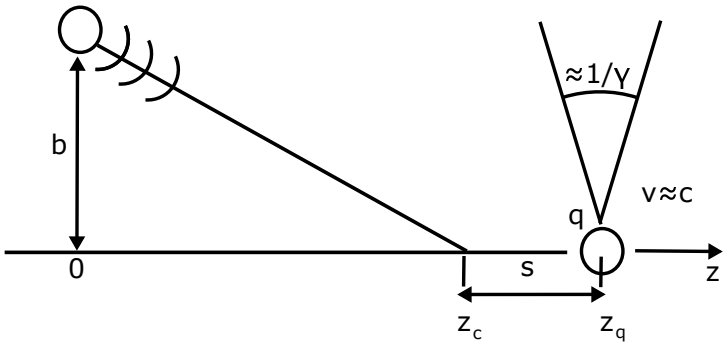

Figure 3.1: Fields radiated by a metallic discontinuity excited by a relativistic charge moving along the z axis.

3.1.2 Fundamental Theorem of Beam Loading

Consider a charged particle traversing an accelerating structure, entering at $z = 0$ and leaving at $z = L$. The charge particle will induce a voltage, V_b inside the cavity. The beam must put energy into the cavity to achieve this, due to energy conservation. As the bunch must loose energy it must experience a decelerating potential V_e, as the field is excited. This decelerating potential can be shown to be exactly half the excited voltage through the application of energy conservation as shown in appendix A. This is known as the fundamental theorem of beam loading [97] and is stated formally as

$$V_e = \frac{1}{2} V_b. \tag{3.3}$$

This theorem is independent of the energy already stored inside the cavity and is valid for all β as it is a result purely due to energy considerations.

3.2 Modal Expansion of The Wake Potentials

The wakefield is often a complicated function which is heavily dependent on the geometry under consideration and also the properties of the exciting bunch. To

simplify the analysis the wakefield is decomposed into a summation over individual frequency components in the form of the wake potential. The wake potential is simpler than the wakefield as it involves averaging over the fields. This method of decomposing the field relies on the fact that the solutions to Maxwell's equations for a particular case form an orthonormal basis and the EM potentials can therefore be expanded in the Coulomb gauge in terms of the empty cavity eigenmodes. This method was first introduced by Condon in 1941 [98] before later being applied to the wakefields in closed cavities. In this section the modal expansion of the wakefield in the longitudinal and transverse planes is discussed.

3.2.1 Longitudinal Wake Potential

Consider a driving charge, Q entering a perfectly conducting cavity at $z = 0$ and leaving at $z = L$ travelling at the speed of light. The voltage experienced by a test bunch trailing by a distance s along the same path, normalized by the charge of the drive particle. The longitudinal wakefield is given by

$$W_z(s) = -\frac{1}{Q}\int_{-\infty}^{s} \left[E_z\left(\vec{r}, z, t\right)\right]_{t=(z+s)/c}\ dz, \tag{3.4}$$

where $t = \frac{(z+s)}{c}$ and $E_z(z,t)$ is the longitudinal component of the electric field excited by the driving charge. Due to the causality condition, $W_z(s < 0) = 0$ which results in no wakefield being present ahead of the drive charge. This formalism of the wakefield is much simpler than considering the induced amplitude of the EM fields.

This integral over the total field inside the cavity can be changed into a summation over a set of orthonormal modes by applying the Condon method [98]. After several lines of mathematics which have been detailed in [60] and is given

in appendix B, the wakefield can be written as:

$$W_z(s) = \sum_n^{\infty} k_{\parallel,n} \cos\left(\frac{\omega_n s}{c}\right) \begin{cases} 0 & s < 0 \\ 1 & s = 0 \\ 2 & s > 0. \end{cases} \tag{3.5}$$

where $k_{\parallel,n}$ is the modal loss factor and $\omega_n/2\pi$ is the mode frequency. Equation 3.5 is in principle a summation over an infinite series of modes, however in most cases it is convenient to truncate the summation, looking only at modes of high loss factors and/or modal frequencies of interest. Doing so allows for a practical computation times to be achieved as each mode require a full eigenmode simulation to obtain its frequency and loss factor.

In the case where a cavity is of finite conductivity the exponential decay of the wakefield can also be included in the summation through the formula

$$W_z(s) = \sum_n k_{\parallel,n} \cos\left(\frac{\omega_n s}{c}\right) e^{-\omega_n s/2Q_n c} \begin{cases} 0 & s < 0 \\ 1 & s = 0 \\ 2 & s > 0, \end{cases} \tag{3.6}$$

where Q_n is the modal quality factor. This enables the wakefield after many frequency cycles to be considered even in the case when heavy damping is present.

3.2.2 Transverse Wake Potential

The transverse wake potential is defined as the transverse momentum kick experienced by a test charge trailing a distance, s behind the driving charge normalised

by the charge of drive particle.

$$W_{\perp}(s) = -\frac{1}{Q}\int_{-\infty}^{s}\Big[E_{\perp} + (\vec{v}\times\vec{B})_{\perp}\Big]_{t=(z+s)/c}\,dz. \tag{3.7}$$

The transverse wake can be written as a modal sum in a similar way to the longitudinal wakefield and is derived in a similar fashion. The modal sum of the transverse wakefield is detailed in [60] and given by:

$$W_{\perp}(s) = \sum_{n}\frac{k_{\perp,n}c}{\omega_n}\sin\left(\frac{\omega_n s}{c}\right)e^{-\omega_n s/2Q_n c}\begin{cases}0 & s<0\\ 1 & s=0\\ 2 & s>0.\end{cases} \tag{3.8}$$

It is worth noting that the transverse wake is out of phase with the exciting charge and hence a point charge does not experience the transverse field which it excites. Therefore there is no analogous effect to the fundamental theorem of beam loading for transverse deflecting modes.

3.3 Wake Potential of a Bunch

So far only the wake potential of a point charge has been discussed as they are the key in looking at the wakefield from more complex bunch structures. The wakefield of a point charge acts as a Greens function's [99] for the wakefield associated with an arbitrary bunch distribution. As such the wakefield of an arbitrary line distribution, $\lambda(s)$ can be found by taking the convolution of the

bunch distribution with the δ-function wake potential [95], given by;

$$V_z(s) = \int_0^\infty \lambda(s-s')W_z(s')\ ds' \tag{3.9}$$

and

$$V_\perp(s) = \int_0^\infty \lambda(s-s')W_\perp(s')\ ds'. \tag{3.10}$$

The energy lost by a bunch traversing the cavity is equivalent to the work done on the bunch by the field and is given by

$$\Delta U = Q_t \int_{-\infty}^\infty \lambda(z)W_z(z)\ dz \tag{3.11}$$

where Q_t is the total charge of the bunch. The loss factor for the bunch can then be written as

$$k_{tot} = \frac{1}{Q_t}\int_{-\infty}^\infty \lambda(z)W_z(z)\ dz. \tag{3.12}$$

3.4 The Panofsky-Wenzel Theorem

If a drive bunch traverses an arbitrary shaped closed cavity, exciting a longitudinal electric field, E_z then the transverse momentum kick given to a test charge travelling behind the exciting bunch is given by [63, 100];

$$p_\perp = \frac{ie}{\omega}\int_0^L [\nabla_\perp E_z(z,t)]_{t=z/c}\ dz, \tag{3.13}$$

where e is the EM charge of the electron. Here we assume that there is no electric field at $z = 0$ or $z = L$, and that the end walls are perpendicular to the beams velocity. For a test bunch arriving once the drive bunch has left the cavity ($s > L$)

the longitudinal and transverse wake potentials are related by

$$\frac{\partial W_\perp}{\partial s} = \frac{c}{eQ}\frac{\partial p_\perp}{\partial s} \tag{3.14}$$

$$= -\frac{1}{Q}\int_0^L [\nabla_\perp E_z(z,t)]_{t=s/c}\ dz \tag{3.15}$$

$$= \nabla_\perp W_z. \tag{3.16}$$

This is known as the Panofsky-Wenzel theorem and it relates the longitudinal and transverse wakefields experienced by the test charge.

3.5 The Wakefield Excited By a Train of Bunches

When a train of identical charged bunches traverses an accelerating cavity each bunch will deposit a voltage of equal magnitude into the cavity modes. The voltages induced will however have different phases to those already present in the cavity. As a result some modes add in phase and some out of phase, this can result in some voltages growing steadily over the bunch train and others cancelling out or oscillating.

For cavities with high Q_{ex} the resonant driving of a cavity mode can lead to voltages comparable to the voltages in the accelerating mode building up. These voltages can result in heating of the cavity walls, degradation of the beam quality and potentially the loss of bunches.

To look at this phenomena the sum wakefield can be defined as;

$$S_{z,\perp}(N) = \sum_{n=0}^{N} W_{z,\perp}(ns_b) \tag{3.17}$$

where $W_{z,\perp}$ are the longitudinal or transverse wakefield given by equations 3.6

and 3.8 respectively, s_b is the bunch spacing and N is the total number of bunches in the bunch train. The sum wakefield amounts to the addition of the voltages induced as complex phasors.

As with the wakefield it is possible to look at the behaviour of both the sum wakefield as a whole or at a specific set of modes which are of particular interest. The sum wakefield is a useful tool for looking at the behaviour of the wakefield over many bunches where full time domain simulations are impractical due to the large computational demands. For example a full simulation of a bunch train which is 1 ms long would require a wakefield of approximately 300 km to be simulated which is impractical in terms of computational expense.

The sum wakefield over the bunch train at ESS is particularly important due to the lack of active damping applied to the HOMs due to the lack of HOM couplers. This means that HOMs may have Q_{ex} which result in e-folding lengths ($\frac{2Q_{ex}c}{\omega}$) comparable in magnitude to the length of the bunch train. As a result the fields excited by bunch at the start of the bunch train may be able to act on bunches at the end of the bunch train. The effects of resonantly excited HOM will be discussed in detail in chapter 7.

3.6 Impedance

The concept of impedance is a common idea in circuit theory where the impedance is defined as the ratio of the complex voltage and the current. The impedance, Z of a circuit is usually separated into two components,

$$Z = R + jX \tag{3.18}$$

where R is the resistance and X is the reactance. Impedance is useful tool for solving circuit problems in the frequency domain as the impedance is a function of frequency.

The idea of impedance in a circuit is analogous to the situation where a beam is inside an accelerator. In this analogy, the beam behaves as a time varying current source and the fields induced in the accelerator components as a voltage. This is commonly known as the beam coupling impedance and its longitudinal component is defined as

$$Z_{\parallel}(\vec{r}_b,\omega) = -\frac{1}{\tilde{I}}\int_{-\infty}^{\infty} \tilde{E}_z(\vec{r}_b,z)e^{jkz}\ dz \tag{3.19}$$

and the transverse dipole impedance as

$$Z_{\perp}(\vec{r}_b,\omega) = \frac{j}{qr_b}\int_{-\infty}^{\infty} \left[\tilde{E}(\vec{r}_b,z) + \vec{v}\times\tilde{\vec{B}}(\vec{r}_b,z)\right]_{\perp} e^{j\omega z/v}\ dz \tag{3.20}$$

where $\tilde{I}$ is the time varying current, $\tilde{E}$ the time varying electric field and $\tilde{B}$ the time varying magnetic field. $Z_{\parallel}$ is given in units of Ω and $Z_{\perp}$ in units of Ω/m and they are the Fourier pair of the longitudinal and transverse wakes respectively [101]. Figure 3.2 shows the longitudinal impedance spectra for a copper pillbox of radius 50 mm and length 100 mm with a 2 mm radius beam pipe obtained using CST, excited by a bunch of length σ =25 mm. Each of the peaks corresponds to a mode that has been excited by the beam, the area and width of which can be used to calculate both the loss parameter and Q_{ex} for the mode.

In this chapter the concepts of the wakefield and relativistic effects such as the catch-up problem have been discussed. In addition details the modal summa-

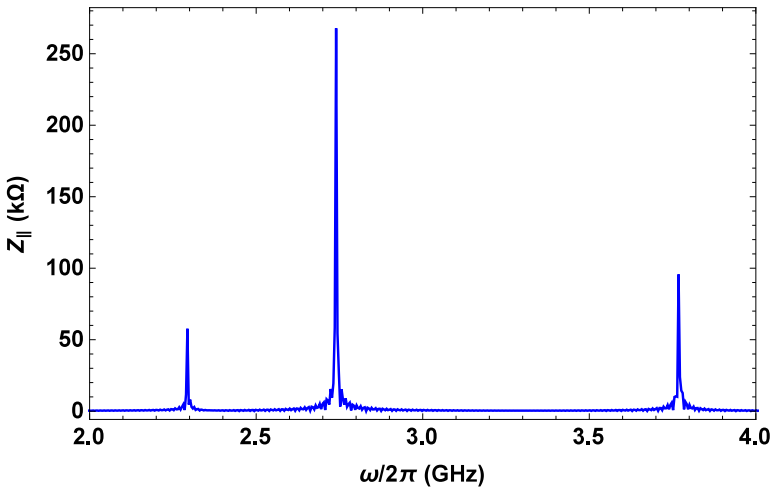

Figure 3.2: Longitudinal impedance spectrum for a pillbox cavity excited by a Gaussian bunch in CST.

tion method for both the longitudinal and transverse wakefield have been given. Further the relationship between the wakefield and impedance has been given.

Each of these requires simulations of the accelerating cavity to obtain both the frequency and loss/kick factors. As simulations of full cavities can be very costly it is beneficial in the first instance to model the behaviour using single cell simulations and an equivalent circuit model. In the next chapter the circuit model of accelerator cavities will be introduced and its relationship to what is observed in full eigenmode simulations is discussed.

Chapter 4

Circuit Model of Accelerator Cavities

The simulation of full accelerating structures computationally expensive in terms of both CPU time and memory particularly for larger structures. One method to reduce the cost of initial simulations is an equivalent circuit model which reduces the simulation to a straightforward eigenvalue problem which can be readily solved. This reduction in the number of parameters truncates the problem resulting in a partial loss of the physics and as a result full eigenvalue simulations are required of final cavity designs. The cavity parameters can be approximated rapidly by modelling it as an equivalent lumped element RLC circuit [95]. The circuit model comes into its own during early design work as a design tool or when many different changes need to be investigated rapidly which is particularly useful for the work later in chapter 5. The first application of this method to multi-cell structures was performed by Nagle et al. [102] where they accurately modelled the behaviour of a standing wave accelerator tank.

The analogy between the circuit model and that of a real accelerating structure

is very apt. The inductor (L) in the circuit represents the magnetic field whilst the capacitor (C) represents the electric field, the oscillation of stored energy from capacitive to inductive is analogous to the oscillation between the electric and magnetic fields in an EM wave. The resistor in the circuit is used to represent losses from the field to the metallic walls of the cavity.

In practise the EM fields of several accelerating cells are coupled close together and the whole structure behaves as a system of coupled oscillators. This coupling can be represented in the model either through a mutual inductance or capacitance between neighbouring cells. The actual nature of the coupling is of little concern as long as it is modelled consistently throughout and the coupling is small.

4.1 The Single Chain Circuit Model

The behaviour of uncoupled monopole bands can be accurately modelled through the use of a single chain of coupled RLC circuits [102]. Due to the coupling between cells the degeneracy of the resonant frequency is lost and a series of modes or a passband appears. The gap between the various bands is known as the stop-band, within the frequency range of the stop-band no modes exist within the cavity. The cell-to-cell coupling plays a key role in the behaviour of the structure as it influences both the bandwidth of the passbands as well as the stability of each mode to changes in the structure.

In this section the circuit model will be derived with inductive coupling between cells and will then be compared to the result obtained using capacitive coupling to show that the nature of the coupling is unimportant in most cases. In the first instance only nearest neighbour coupling will be considered as it is dominant until the fields couple from cells further away in the chain.

The circuit used in this derivation is illustrated in figure 4.1 for the case of an infinite chain of cells. Kirchoff's voltage rule can be applied to cell m to give;

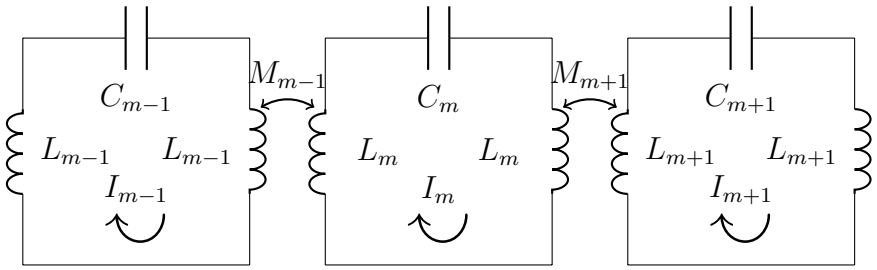

Figure 4.1: Single chain circuit model, with the inductors acting as couplers between neighbouring cells.

$$\left(2j\omega L_m + \frac{1}{j\omega C_m}\right) I_m + j\omega M_{m,m+1} I_{m+1} + j\omega M_{m,m-1} I_{m-1} = 0 \tag{4.1}$$

where L_m, C_m and I_m are the inductance, capacitance and current of the m$^{\text{th}}$ cell respectively. $M_{m,m\pm1}$ is the mutual inductance between loop m and $m \pm 1$. dividing through by $2j\omega L_m$ and defining the resonance frequency as

$$\omega_r = \frac{1}{\sqrt{2L_m C_m}} \tag{4.2}$$

results in

$$\left(1 - \frac{\omega_m^2}{\omega^2}\right) I_m + \frac{M_{m,m+1}}{2L_m} I_{m+1} + \frac{M_{m,m-1}}{2L_m} I_{m-1} = 0. \tag{4.3}$$

By normalising the current in terms of independent variables as

$$I_m = \frac{a_m}{\omega_m \sqrt{L_m}} = \frac{a_m \sqrt{C_m}}{\omega_m} \tag{4.4}$$

and multiplying by $\frac{\sqrt{L_m}}{\omega_m}$ equation 4.3 becomes

$$\left(\frac{1}{\omega_m^2} - \frac{1}{\omega^2}\right) a_m + \frac{a_{m+1} M_{m,m+1}}{2\omega_m \omega_{m+1} \sqrt{L_m L_{m+1}}} + \frac{a_{m-1} M_{m,m-1}}{2\omega_m \omega_{m-1} \sqrt{L_m L_{m-1}}} = 0. \tag{4.5}$$

The cell-to-cell coupling can be defined as

$$\eta_{m\pm\frac{1}{2}} = \frac{M_{m,m\pm1}}{\omega_m \omega_{m\pm1}\sqrt{L_m L_{m\pm1}}} \tag{4.6}$$

and the coupling coefficient as

$$\kappa_{m\pm\frac{1}{2}} = \eta_{m\pm\frac{1}{2}}\omega_m\omega_{m\pm1}. \tag{4.7}$$

In a structure subjected to infinite periodic boundary conditions $\eta_{m\pm\frac{1}{2}} = \eta$ and by applying the Bloch boundary condition,

$$a_m = a_0 e^{jm\phi} \tag{4.8}$$

a further relationship can be found

$$\left(\frac{1}{\omega_m^2} - \frac{1}{\omega^2}\right) + \frac{\eta}{2}\left(e^{j\phi} + e^{-j\phi}\right) = 0 \tag{4.9}$$

If the cells are identical $\omega_{m+1} = \omega_m$ equation 4.9 becomes

$$\left(1 - \frac{\omega_m^2}{\omega^2}\right) + \kappa\cos\phi = 0 \tag{4.10}$$

where $\kappa = \eta/2\omega_m^2$ and this can be rearranged to make ω the subject

$$\omega = \frac{\omega_r}{\sqrt{1+\kappa\cos\phi}}. \tag{4.11}$$

This relationship is known as the dispersion relationship. To apply this relationship and the equivalent matrix formalism of the equations, the resonant frequency and cell-to-cell coupling must be calculated using an eigenmode solver.

This is done so the dispersion relationship can be constrained which requires the use of two frequencies from simulations. In most cases the 0 and π modes are chosen as they are readily calculated in most RF codes. In terms of the ω_0 and ω_π mode frequencies the cell resonant frequency is given by

$$\omega_r = \sqrt{\frac{2\omega_0^2\omega_\pi^2}{\omega_0^2 + \omega_\pi^2}} \tag{4.12}$$

and the cell-to-cell coupling by

$$\kappa = \frac{\omega_\pi^2 - \omega_0^2}{\omega_\pi^2 + \omega_0^2}. \tag{4.13}$$

An example of a dispersion curve obtained by applying the single chain circuit model is given in figure 4.2.

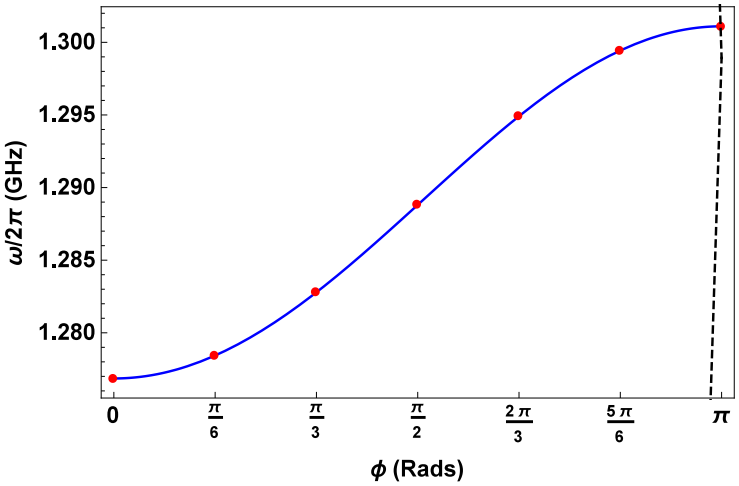

Figure 4.2: The single chain circuit model with nearest neighbour coupling applied to the first band of the TESLA cavity [16]. Single cell data from HFSS is plotted as red circles, the circuit model is plotted as a solid blue line and the light line is plotted as dashed line.

In addition to the data in figure 4.2 the light line is also plotted. The light line is a visual representation of the phase velocity of light and is useful as only

modes which intersect the light line will be strongly excited by the beam. The light line is given by [11]

$$\omega = \frac{\phi\beta c}{L} \tag{4.14}$$

where L is the cell length.

To find the resonance frequencies for a finite length structure, equation 4.5 is written for each cell of the structure and cast as a matrix equation which can then be readily solved.

4.1.1 Next Nearest Neighbour Coupling

In the case where the coupling is large the single chain model begins to break down due to coupling from cells further down the chain. The model can be extended to take this into account [76] by including an additional inductive coupling from the next-nearest neighbour cells. Following a similar derivation the normal single chain model, the dispersion relationship takes the form of

$$\omega = \frac{\omega_r}{\sqrt{1 + \kappa_1 \cos(\phi) + \kappa_2 \cos(2\phi)}}. \tag{4.15}$$

In principle this could be extended further as

$$\omega = \frac{\omega_r}{\sqrt{1 + \sum_{n=1}^{N} \kappa_n \cos(n\phi)}}, \tag{4.16}$$

however in practice the third order and beyond coupling is usually very small. The system described her can also be represented through capacitive coupling which is discussed in the next section.

4.1.2 Capacitive Coupling

Taking the circuit used by Padamsee [14] illustrated in figure 4.3 where C_k is the coupling capacitance between cells and C_b is the coupling capacitance of the end-cells to the beam-pipe. The individual cell capacitances, inductances and currents are given bt C, L and I respectively.

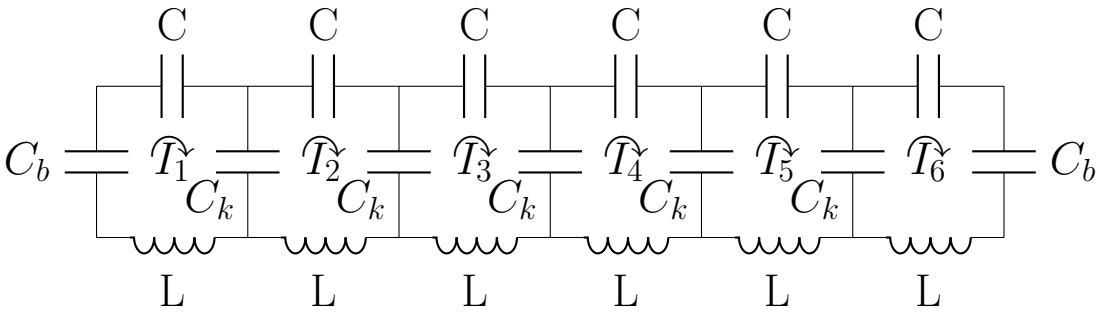

Figure 4.3: Equivalent circuit used in [14] for a six cell cavity.

Applying Kirchoff's voltage rules the equations can be found:

$$(1+k+\gamma)I_1 - kI_2 = \Omega_r I_1 \tag{4.17}$$

$$(1+2k)I_n - k(I_{n+1}+I_{n-1}) = \Omega_r I_n \tag{4.18}$$

$$(1+k+\gamma)I_N - kI_{N-1} = \Omega_r I_N, \tag{4.19}$$

where $k = \frac{C_k}{C}$ to be the cell-to-cell coupling and $\Omega_r = \frac{\omega^2}{\omega_r^2}$. Further $\gamma = \frac{C_b}{C}$ which is present due to the beam pipe and is a shift in the end cell frequencies used to obtain a field-flat accelerating mode.

Taking equation 4.19 for the mid-cells and applying Floquet's theorem results in the dispersion relationship

$$\omega_m = \omega_r \sqrt{1+2k(1-\cos\phi)} \tag{4.20}$$

which is similar in form to equation 4.11. The two models which have been given

include the cell-to-cell coupling in different ways; one through a mutual inductance/capacitance and the other through a shared capacitor/inductor. Although slightly different due to the definitions of the different resonant frequencies and coupling terms the are equivalent and differ mainly in the position of the square root. In the next section the differences between the resulting equations is discussed.

4.1.3 Inductive Vs Capacitive Coupling

The various bands in different types of accelerating structure may be coupled capacitively, inductively or by a combination of both. By following the derivation given in section 4.1 with the coupling through a mutual capacitance rather than inductance the dispersion relationship is found to be

$$\omega = \omega_r \sqrt{1 + \kappa \cos \phi}. \tag{4.21}$$

Taking the Taylor expansion of the inductive model (equation 4.11) gives

$$\omega \approx \omega_r (1 + \frac{\kappa \cos(\phi)}{2} - \frac{(\kappa \cos(\phi))^2}{8} + ...) \tag{4.22}$$

and the Taylor expansion of the capacitive model (equation 4.21) gives

$$\omega \approx \omega_r (1 - \frac{\kappa \cos(\phi)}{2} + \frac{3(\kappa \cos(\phi))^2}{8} + ...). \tag{4.23}$$

Comparing equations 4.22 and 4.23 to second order they differ by a relative minus sign in the second term which is taken into account by the different definitions of κ. For most cases κ is $\mathcal{O}(0.01)$ and hence the nature of the coupling is a minimal contributor to the resulting mode frequencies. This is shown in figure 4.4

where even for $\kappa = 0.1$ the difference in predicted frequency is around 0.5%.

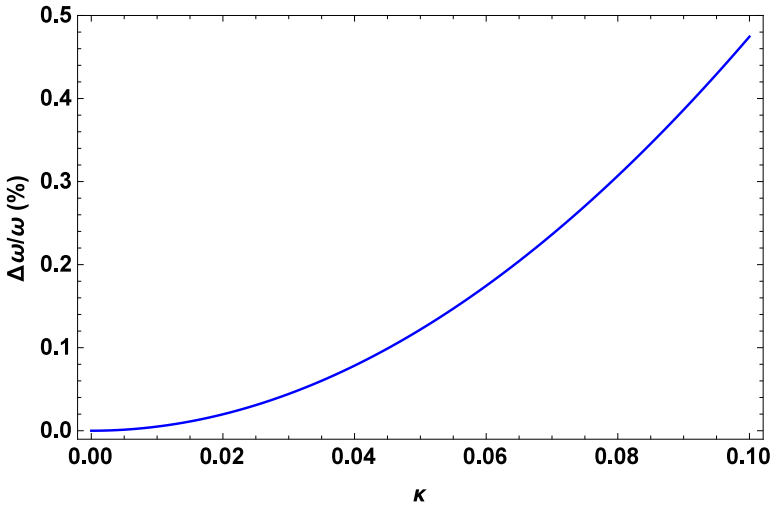

Figure 4.4: The percentage difference in a π mode frequency found using capacitive and inductive coupling as a function of cell-to-cell coupling.

4.2 The Double Chain Circuit Model

In a single cell cavity the dipole modes are independent of each other, however when multiple cells are present hybridisation between TE and TM modes occurs. This hybridisation is caused by coupling between TE and TM modes which cannot be accounted for in the single chain model. This problem was resolved by Bane and Gluckstern [103] through the development of the double band circuit model.

In the double band circuit model two chains of circuits are introduced, with one representing the TE and one the TM mode. In addition to the coupling a long a single chain, the TE and TM chains are allowed to couple to each other mimicking the hybridisation seen in real cavities. This circuit is illustrated in figure 4.5. In the following derivation, the lower chain corresponds to the TM mode and the upper to the TE mode. Kirchoffs voltage rules are again applied to each chain and the current is normalised in terms of independent variables as

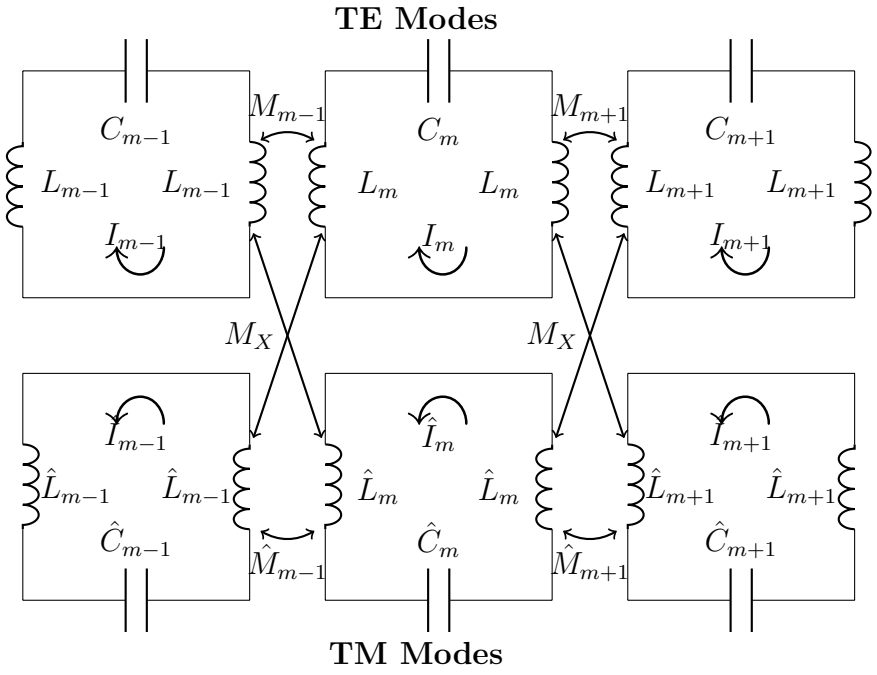

Figure 4.5: Double chain circuit model with two chains similar to the single chain model circuit, one representing the TE mode and the other the TM. In addition there is also an extra coupling between the two chains.

in the single chain case.

For the TE wave the corresponding equation is

$$\left(\frac{1}{\omega_m^2}-\frac{1}{\omega^2}\right)a_m+\frac{\eta_{m+\frac{1}{2}}}{2}a_{m+1}+\frac{\eta_{m-\frac{1}{2}}}{2}a_{m-1}=\frac{\sqrt{\eta_{m+\frac{1}{2}}\hat{\eta}_{m+\frac{1}{2}}}}{2}\hat{a}_{m+1}+\frac{\sqrt{\eta_{m+\frac{1}{2}}\hat{\eta}_{m-\frac{1}{2}}}}{2}\hat{a}_{m-1}, \tag{4.24}$$

while for the TM wave

$$\left(\frac{1}{\hat{\omega}_m^2}-\frac{1}{\omega^2}\right)\hat{a}_m+\frac{\hat{\eta}_{m+\frac{1}{2}}}{2}\hat{a}_{m+1}+\frac{\hat{\eta}_{m-\frac{1}{2}}}{2}\hat{a}_{m-1}=\frac{\sqrt{\eta_{m+\frac{1}{2}}\hat{\eta}_{m+\frac{1}{2}}}}{2}a_{m+1}+\frac{\sqrt{\eta_{m+\frac{1}{2}}\hat{\eta}_{m-\frac{1}{2}}}}{2}a_{m-1}. \tag{4.25}$$

The parameters in these two equations have the same definitions as those given in section 4.1. As in the previous derivation the infinite periodic condition in equation 4.8 and the cell-to-cell coupling is written in terms of κ and $\hat{\kappa}$ defined

by equation 4.7. The resulting equations are

$$\left(1-\frac{\omega_r^2}{\omega^2}\right)a + a\kappa\cos\phi = \frac{j\sqrt{\kappa\hat{\kappa}}}{2\hat{\omega}}\hat{a}\sin\phi \tag{4.26}$$

$$\left(1-\frac{\hat{\omega}_r^2}{\omega^2}\right)\hat{a} - \hat{a}\hat{\kappa}\cos\phi = -\frac{j\sqrt{\kappa\hat{\kappa}}}{2\hat{\omega}}a\sin\phi. \tag{4.27}$$

Equations 4.26 and 4.27 can be expressed in matrix form as

$$\begin{pmatrix} \frac{1+\kappa\cos\phi}{\omega_m^2} & \frac{j\sqrt{\kappa\hat{\kappa}}\sin\phi}{\omega_m\hat{\omega}} \\ -\frac{j\sqrt{\kappa\hat{\kappa}}\sin\phi}{\omega_m\hat{\omega}} & \frac{1-\hat{\kappa}\cos\phi}{\omega_m^2} \end{pmatrix}\begin{pmatrix} a \\ \hat{a} \end{pmatrix} = \frac{1}{\omega^2}\begin{pmatrix} a \\ \hat{a} \end{pmatrix} \tag{4.28}$$

Finally by rearranging equation 4.28 and finding its determinant the dispersion relationship is found to be

$$\left(\frac{1+\kappa\cos\phi}{\omega_m^2}-\frac{1}{\omega^2}\right)\left(\frac{1-\hat{\kappa}\cos\phi}{\omega_m^2}-\frac{1}{\omega^2}\right) - \frac{\kappa\hat{\kappa}}{\omega_m^2\hat{\omega}_m^2}\sin^2\phi = 0 \tag{4.29}$$

The dispersion relationship contains both the individual TE and TM dispersion curves as well as an additional coupling term. When applying this equation it is important to identify which wave is forward travelling ($\omega_\pi > \omega_0$) and which is backward travelling ($\omega_\pi < \omega_0$) to ensure the coupling coefficients are both positive. Again the coupling coefficients and resonant frequencies can be found in terms of the 0 and π mode frequencies;

$$\omega_r = \sqrt{\frac{2\omega_0^2\omega_\pi^2}{\omega_0^2+\omega_\pi^2}} \quad \text{and} \quad \kappa = \frac{\omega_\pi^2-\omega_0^2}{\omega_\pi^2+\omega_0^2} \tag{4.30}$$

and

$$\hat{\omega}_r = \sqrt{\frac{2\hat{\omega}_0^2\hat{\omega}_\pi^2}{\hat{\omega}_0^2+\hat{\omega}_\pi^2}} \quad \text{and} \quad \hat{\kappa} = \frac{\hat{\omega}_\pi^2-\hat{\omega}_0^2}{\hat{\omega}_\pi^2+\hat{\omega}_0^2} \tag{4.31}$$

Figure 4.6 shows a fit of equation 4.27 applied to single cell data obtained through

simulations of the TESLA cavity mid-cell in HFSS.

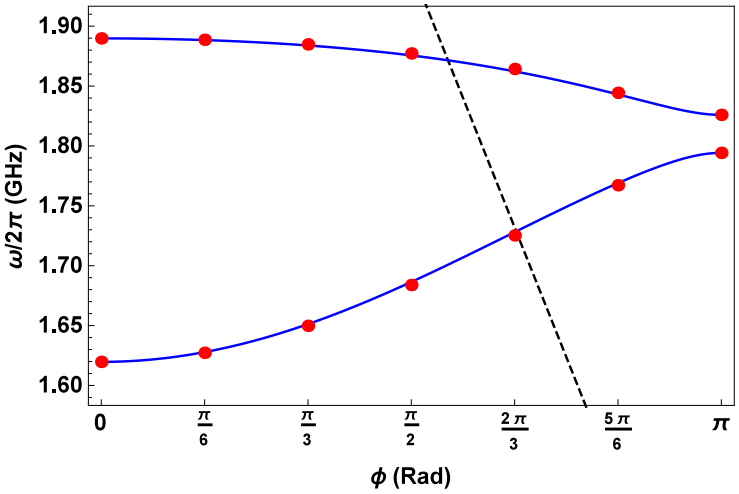

Figure 4.6: The double chain circuit model applied to the first two dipole bands of the TESLA cavity. Single cell data from HFSS is plotted as red circles, the circuit model is plotted as a solid blue line and the light lines are plotted as dashed line.

4.3 Including Errors In The Circuit Model

It is possible to investigate the impact of manufacturing errors on the modes of a cavity using the circuit model. This is much less computationally expensive than performing full 3D simulations which can only allow a limited number of errors to be investigated. In a cavity the cell frequencies and fields change due to the geometric differences adding or subtracting regions of EM fields. Similarly in the circuit model this can be achieved by adding error to the components of the circuit.

An error on the capacitance is equivalent to a perturbation in the electric field and similarly with the inductance in the magnetic field. In practice, for the accelerating mode, the errors are usually capacitive in nature, however for HOMs a combination of errors occurs. As a result of this making an exact prediction is

difficult however it is possible to use the circuit model to comment on the likely spread in frequencies and field profiles.

Taking the circuit shown in figure 4.3 and allowing the capacitance and inductance to have errors of the form

$$C \to \frac{C}{1+e_n} \tag{4.32}$$

$$L \to L(1+\delta_n) \tag{4.33}$$

where e_n and δ_n are capacitive and inductive errors on cell n. The resulting equations for each cell an be found to be,

$$\begin{aligned}
\frac{1+k+\gamma+e_1}{1+\delta_1}I_1 - \frac{k}{1+\delta_1}I_2 &= \Omega_r I_1, & (4.34)\\
\frac{1+2k+e_n}{1+\delta_n}I_n - \frac{k}{1+\delta_n}(I_{n+1}+I_{n-1}) &= \Omega_r I_n, & (4.35)\\
\frac{1+k+\gamma+e_N}{1+\delta_N}I_N - \frac{k}{1+\delta_N}I_{N-1} &= \Omega_r I_N. & (4.36)
\end{aligned}$$

This set of equations can be cast as a matrix eigenvalue problem which is readily solvable with minimal computational resources. The changes in the inductance and capacitance will result in the resonant frequency of the cell shifting to a new value given by

$$\omega_r^2 = \frac{1}{LC}\frac{1+e}{1+\delta}. \tag{4.37}$$

Identifying the specific errors that cause the cell frequency to shift would require full simulations of each individual cell. However if a distribution of cell frequencies is found by applying random errors it is possible to investigate the anticipated spread in the final frequencies caused by the distribution of single cell frequencies.

The use of circuit models in the design of accelerating cavities is extensive and well documented. In the studies within this thesis the circuit model allows the

study of a multitude of errors to be performed very quickly with only a handful of eigenvalue simulations required which is particularly useful when small changes or errors are introduced. By reducing the problem to a circuit model there is information in the original design which is lost an example would be that the cell-to-cell coupling may be a hybrid between electric and magnetic coupling which is not taken into account. Further it is not possible to look at the surface electric or magnetic fields which are particularly important if working close to the surface field limits of material used to construct the cavity. In addition in cases where the frequency of the modes is close to or above the beam pipe cut-off frequency multiple cavities may couple together and in this model the implications of this are not considered.

The circuit model allows the essential physics of the situation in hand to be focussed on whilst varying many parameters, and hence it serves as an essential initial design tool. These circuit models must then be verified with full finite element or finite difference-based EM computer codes—such as HFSS, GdFiDL and CST MWS.

The equivalent circuit models described in this section will be applied to the accelerating mode and HOMs in the ESS cavities. In particular the circuit model including errors will be used to investigate the likely spread in HOM frequencies due to manufacturing errors. These errors can result in HOM frequencies shifting by 10's of MHz and can lead to significant effect on the beam. The major concern is if an lightly damped mode lies on a harmonic of the bunch frequency which can result in the resonant excitation of the mode. The errors themselves are discussed in chapter 5 and the impact on the beam at ESS in chapter 7. In the next chapter a detailed analysis of the SCRF cavities at ESS is give which is followed by a study of the impact of fabrication errors on the modal structure of

the ESS medium-β cavity, using both detailed eigenmode simulations as well as equivalent circuits.

Chapter 5

ESS Cavity Mode Analysis

The mode frequencies and associated field distributions for an arbitrarily shaped cavity cannot readily be found analytically, therefore numerical techniques are usually employed. In this chapter a brief introduction to the numerical methods and various codes used to determine the field profiles and mode frequencies of accelerating structures will be given. This is followed by a detailed modal and wakefield analysis of each of the ESS SCRF cavities. In addition, modifications to the ESS high-β cavity are proposed which would increase the cavity performance and reduce the risks posed by HOMs to the performance of the machine. Finally, the frequency sensitivity of the HOMs in the ESS medium-β cavity are analysed using an equivalent circuit approach in conjunction with extensive eigenmode simulations. The methodology adopted for investigating the impact of manufacturing errors on the resonant frequency of the HOMs can readily be extended to other machines in particular it could be used to investigate the effects in the proposed ILC and future high power proton machines such as Project-X.

5.1 Simulation Techniques

In order to calculate the fields and eigenfrequencies of a cavity Maxwell's equations must be solved—either analytically or numerically. Solving Maxwell's equations analytically within complex geometries is impractical due to the complexity and size of the problems often encountered. As a result numerical techniques are usually employed. However, these can be both time and computationally expensive.

The problem at hand generally takes the form of a classical boundary value problem which can be described by

$$L(u) = s \tag{5.1}$$

where L is a differential operator, u is the solution to be found and s is the source. The sources for Maxwell's equations are currents and charges within the computational volume. This equation combined with a set of known solutions at the boundaries allow the equation to be solved. Such equations can be solved by implementing several numerical techniques, the two most common of which are the Finite Difference Method (FDM) and Finite Element Method (FEM) [104]. In these simulations the mesh is iteratively varied until the frequency of the solution changes at a level below some predefined level to ensure the solution is not an artefact of the mesh.

5.1.1 Finite Difference Method

The FDM is based on the Taylor expansion of the solution [105] at mesh point j,

$$f(x_{j+1}) = \sum_{n=0}^{\infty} f^{(n)}(x_j)\frac{h_j^n}{n!} \tag{5.2}$$

where

$$h_j \equiv x_{j+1} - x_j. \tag{5.3}$$

In a 1D problem the derivatives can be written in terms of the functions values at discreet mesh points x_j as;

$$f'(x_j) = \frac{f(x_{j+1}) - f(x_{j-1})}{2h_j} \tag{5.4}$$

$$f''(x_j) = \frac{f(x_{j+1}) - 2f(x_j) + f(x_{j-1})}{4h_j^2}. \tag{5.5}$$

These derivatives can be used to write the differential equation as a series of linear equations that can be cast as a matrix and solved to find the solutions at each mesh point. The FDM requires few calculations per mesh point, however due to its slow frequency convergence it requires a large number of mesh points to achieve accurate results.

5.1.2 Finite Element Method

The FEM method of solving the boundary problem, involves dividing the computational domain up into a series of smaller elements known as finite elements [106]. The solution is then expressed as a series of interpolating functions which form an expansion basis. The approximate solution can the be written as

$$f = \sum_{i=1}^{n} \alpha_i N_i, \tag{5.6}$$

where n is the number of nodes, α_i is the solution at node i and N_i is the expansion basis at point i. To solve the boundary value problem given by equation 5.1 this then needs to be integrated along the computational domain using the weighted

residual approach, in which the average residual is forced to zero. This result in

$$\int_0^1 L(u)w(x)dx = \int_0^1 sw(x)dx, \tag{5.7}$$

where the choice of $w(x)$, the weight function defines the scheme. In the case of Galerkin FEM, the weight function is the same as the basis function $N_i(x)$. The problem can then be represented as an eigenvalue problem using sparse matrices which can be readily solved using modern computers.

For Maxwell's equations in a source free region ($s = 0$), u may be identified to be the electric field, $\vec{E}$ inside the region resulting in the operator equation

$$\nabla \times \left(\frac{1}{\mu}\nabla\vec{E}\right) - k^2\epsilon\vec{E} = 0 \tag{5.8}$$

5.1.3 Mesh Types

In order to utilise these numerical tools, the problem must be discretised. This is achieved by approximating the volume with a mesh constructed of primitive mesh cells. Each edge/face of a mesh cell is uniquely connected to its neighbouring cells and contains common mesh points with them.

In 2D problems the primitive cells are usually rectangles or triangles, although curved elements can be used. The quality of a mesh is determined by how accurately it represents the boundaries of the problem. Rectangles in general produce a poorer surface representation than a similar number of triangles and hence higher mesh densities are required to achieve an equivalent accuracy.

In the 3D case these 2D shapes are replaced with their 3D counterparts; hexahedra and tetrahedra which are shown in figure 5.1 alongside their curved linear counterparts. Whilst it is easiest to construct a hexahederal mesh the surface

representation is poor compared to tetrahedral meshes. This often results in more mesh cells being required which can significantly reduce the computational speed. Further, the use of tetrahedral mesh elements allows specific regions to be refined without changing the entire mesh, which as a result allows for fine tuning of the mesh near to the boundary where high fields are expected or found during earlier iterations.

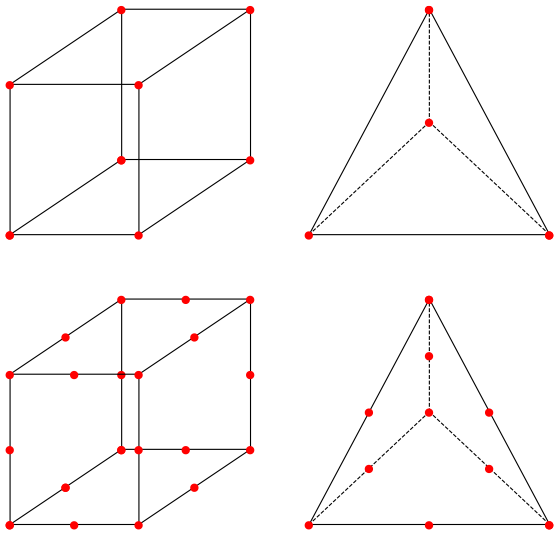

Figure 5.1: Schematic of hexahedral (top left), tetrahedral (top right), curved-hexahedral (bottom left) and curved-tetrahedral (bottom right) with the nodes highlighted as red dots.

5.1.4 Boundary Conditions

In boundary value problems the type of boundaries are extremely important as they are what constrains the problem. In most EM applications the boundary fall into two categories, these are Dirichlet and Neumann conditions [57]. The Dirichlet condition forces the electric field perpendicular to the boundary and magnetic field parallel to it to be zero. This means that it behaves as a perfect electrical conductor (PEC). The Neumann condition forces the transverse magnetic and parallel electric fields to be zero, meaning that it behaves as a perfect magnetic

conductor (PMC). The properties of these boundary conditions are summarised in table 5.1. In the case of a superconducting cavity three types of boundary are

	Dirichlet	Neumann
$\vec{E}$	$\hat{n} \times \vec{E} = 0$	$\hat{n} \cdot \vec{E} = 0$
$\vec{H}$	$\hat{n} \cdot \vec{H} = 0$	$\hat{n} \times \vec{H} = 0$
Material	PEC	PMC
Symmetry Type	Electric	Magnetic

Table 5.1: Summary of the types of boundary used in EM simulations

commonly simulated, the first is the cavity walls which are PEC and the second is the vacuum which exists at every point within the structures walls. Finally many codes also utilise the symmetry of structures by assigning PEC and PMC to planes of electric and magnetic symmetry to reduce computational time and/or to look at solutions with specific field symmetries.

In addition to these boundary conditions several others may be defined and they include, waveguide ports, impedance boundaries and perfectly matched layers (PML's) which are important for driven modal simulations and also quality factor calculations.

5.1.5 Types of Codes

Due to the increase in CPU power and RAM capacity in recent years many 2D and 3D electromagnetic solvers have been written which can operate on either; desktop computers, large servers or supercomputers. These codes can be used to simulate RF cavities of various geometries and can work in either the time or frequency domains. When simulating the monopole modes in an elliptical cavity we can make use of the inherent symmetry of the modes and utilise fast 2D codes such as Poisson Superfish (SF) [107] which takes minutes to solve or appreciably slower 3D solvers such as CST Microwave Studio (MWS) [78], Ansys

HFSS [108] or GdfidL [109] which can take hours, days or weeks to solve in some cases. However, when looking at higher multipoles or cavities without axial symmetry—such as spoke cavities—3D solvers with high meshes are required to acquire even the most basic of results.

The list of codes mentioned here is by no means exhaustive and many other codes are available. In table 5.2 the properties of the codes mentioned by name are summarised.

Code	2D/3D	Mesh Type	Method	Symmetry	Modes/Sim.
SF	2D	Triangular	FDM	360 deg	1
MWS	3D	Tetrahedral	FIT	90 deg	Many
HFSS	3D	Curved Tetrahedral	FEM	Arbitrary	20
Gdfidl	3D	Hexahedral	FDM	90 deg	Many

Table 5.2: Simulation code features

Each code has its own unique set of advantages and disadvantages which determine when they are best used. In this work the codes HFSS, CST and Superfish will be primarily used. In the next section the methodology behind one of the simpler 2D solvers will be given as an example.

5.1.6 Poisson Superfish

SF is a an example of a 2D EM field solver which is readily available and very efficient. In the SF code the cavity is described by a closed contour constructed from various straight lines and conic sections. This contour is approximated by a triangular mesh with Derichlet or Neumann boundary conditions used on the walls. A drive point is also included to excite the structure which must be located in a region of non-zero magnetic field, this means various drive points may be required to find specific modes.

The solver is based on the method described in [107] which works by solving

the generalised Helmholtz equation (c.f. equation 5.1)

$$\nabla^2\phi + k^2\phi = S \tag{5.9}$$

for the eigenvalue k and the eigenfunction $\phi(x)$, the quantity S is the source term. The solver uses the Poynting theorem [9] which is in essence a statement of energy conservation for EM fields within a closed volume and the fact that for a closed cavity the surface integrals must vanish (i.e. no flow of power out of the system). The problem is the solved by finding roots to the function

$$D(k^2) = kc\frac{\int_V \vec{H}_t.\vec{K}_t \; dV}{\int_V \epsilon \left|\vec{H}_t\right|^2 \; dV} \equiv R(k^2) - k^2c^2, \tag{5.10}$$

derived from Maxwell's equations [107], where $\vec{H}_t, \vec{K}_t$ are the time dependent parts of the magnetic field and current density and

$$R(k^2) = k^2c^2\frac{\int_V \epsilon \left|\vec{E}_t\right|^2 \; dV}{\int_V \epsilon \left|\vec{H}_t\right|^2 \; dV}. \tag{5.11}$$

The resonances occur when $D(k^2) = 0$ and $\frac{dD(k^2)}{d(k^2)} = -1$. As there is no magnetic current required to maintain the fields it is implied that $R(k^2) = k^2c^2 = \omega^2$ and the energy stored in the magnetic and electric fields is equal—and the solution is hence resonant. In the following sections the methodology behind the simulation of RF cavities is discussed.

5.2 Simulation of Cavity Modes

Simulation of a full cavity is both time and computationally expensive even with the latest codes and access to a reasonably sized server. To alleviate this issue it is possible to utilise the inherent symmetry within a given structure to reduce the computational volume and hence the number of mesh cells. For the majority of RF cavities this symmetry manifests itself in the form of an azimuthal symmetry. In this case, rather than simulating the whole volume many codes are able to simulate an angular slice of the cavity by using appropriate boundary conditions.

5.2.1 Monopole Mode Simulations

Monopole modes have a full 360 degree symmetry in their field profile and hence only a small segment needs to be simulated. In HFSS as little as a 10 degree segment is require however, in CST MWS and GdfidL the minimum allowable of 90 degrees must be used due to limitations in the code. To simulate monopole modes the symmetry planes of this region must be either; electric-electric to simulate TE modes or magnetic-magnetic to simulate TM modes. In the following analysis monopole modes will refer to TM-type monopole modes as they are the only type which impact significantly on the beam.

A typical electric field profile for TM monopole mode in a pillbox, simulated using HFSS with and without symmetry places are shown in figure 5.2, magnetic-magnetic symmetry planes have been used when simulating the 10 degree slice.

In order to calculate the figures of merit for the cavity, the fields must be extracted and the calculations performed numerically on the extracted field data. For HOMs it is often difficult to identify if a mode is indeed a monopole due to the shape of the cavity distorting the field profiles. In the first instance inspecting the field profile will identify the mode, however if this is not possible, the loss

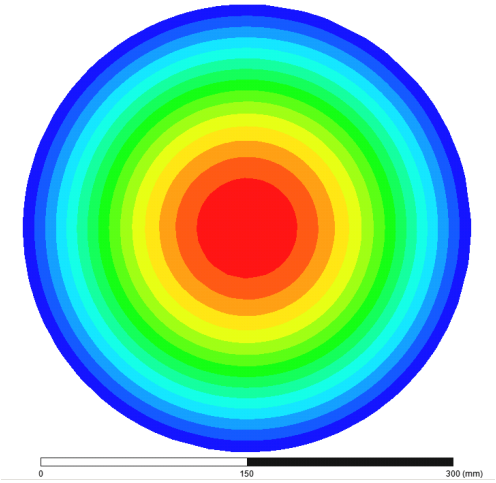

(a) Monopole mode without using symmetry planes.

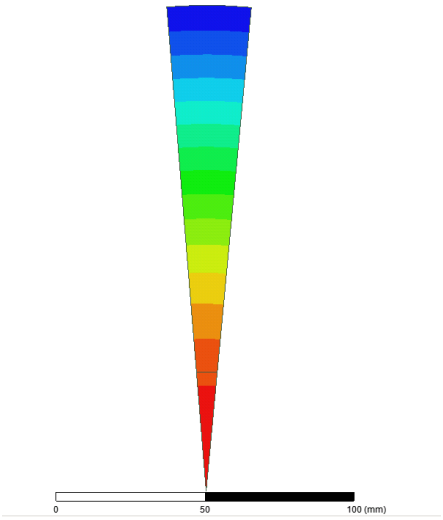

(b) Monopole mode using symmetry planes.

Figure 5.2: Example of electric field profile of a monopole mode both with and without the use of symmetry planes in ANSYS HFSS. Red corresponds to regions of high field and blue to regions of low field.

factor can be used. As alluded to in section 2.2 the loss factor varies as offset to the m^{th} power, which for monopole mode means it is constant. By calculating the loss factor at various offsets the mode type can therefore be easily verified. This method is illustrated for a monopole mode in figure 5.3 and in this case it is clear there is no variation in the loss parameter with offset.

5.2.2 Dipole Mode Simulations

To the dipole modes, a similar method to that of the monopole modes is employed, however a 90 degree segment must be used with electric-magnetic symmetry planes. An electric field profile of a dipole mode simulated in HFSS is shown in figure 5.4.

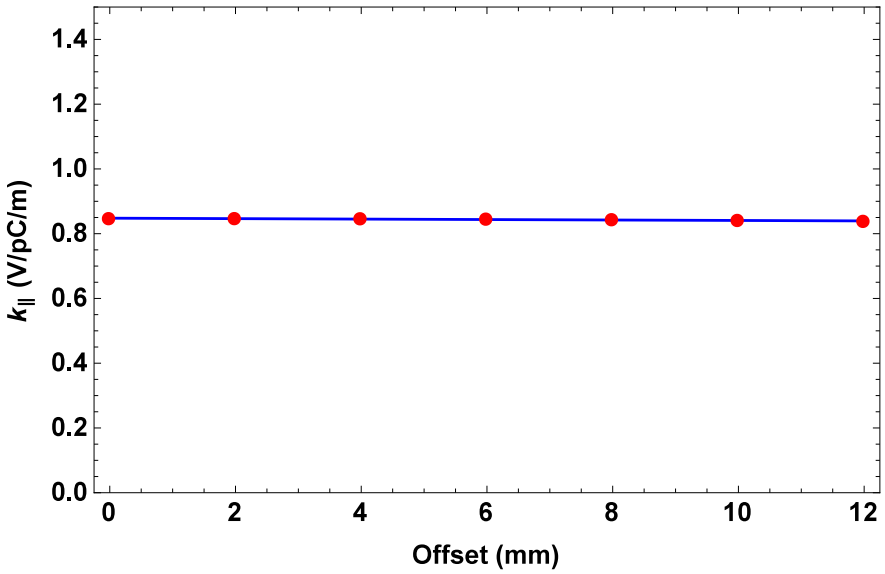

Figure 5.3: Variation of the loss factor for a monopole mode in a pillbox cavity with offset.

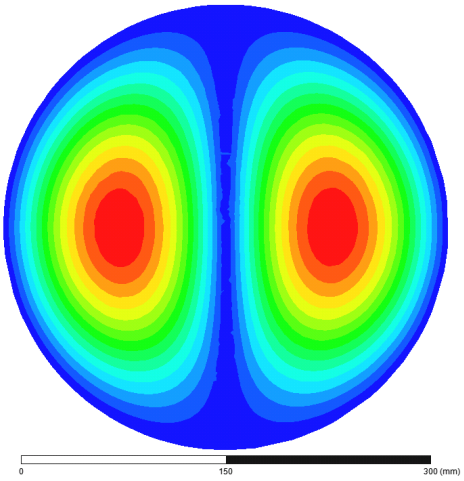

(a) Dipole mode without using symmetry planes.

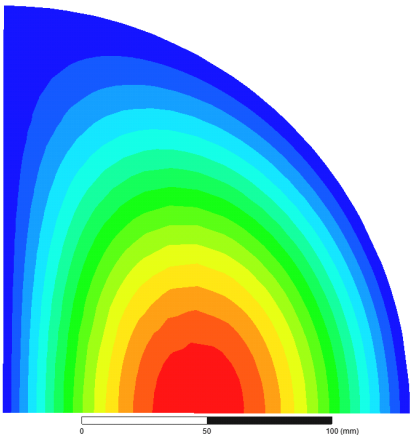

(b) Dipole mode using symmetry planes.

Figure 5.4: Example of a dipole mode being simulated both with and without the use of symmetry planes in ANSYS HFSS. Red corresponds to regions of high field and blue to regions of low field.

In the simulation of dipole modes particular care must be taken as the electric-magnetic symmetry condition allows other HOMs to be found, the first of which is sextupole modes to be simulated. Dipole modes must therefore be identified

using a combination of inspection and plotting the loss factor as a function of offset. When plotting the loss factor, a function of the form Ax^{2m} is fitted (for a dipole $m = 1$). An example of this is illustrated in figure 5.5.

Due to the significant variation of the loss factor with offset great care is taken to align the beam such that it passes through the electrical centre. The electrical centre is defined as the line through which the transverse wakefield is minimised which in an ideal cavity is usually the cavity axis. Dipole modes can additionally be parametrised by the kick factor (equation 2.47) which removes the dependence of the loss factor on offset. The kick factor for the same mode is potted in figure 5.6 and it is clear that the value does not vary as a function of offset.

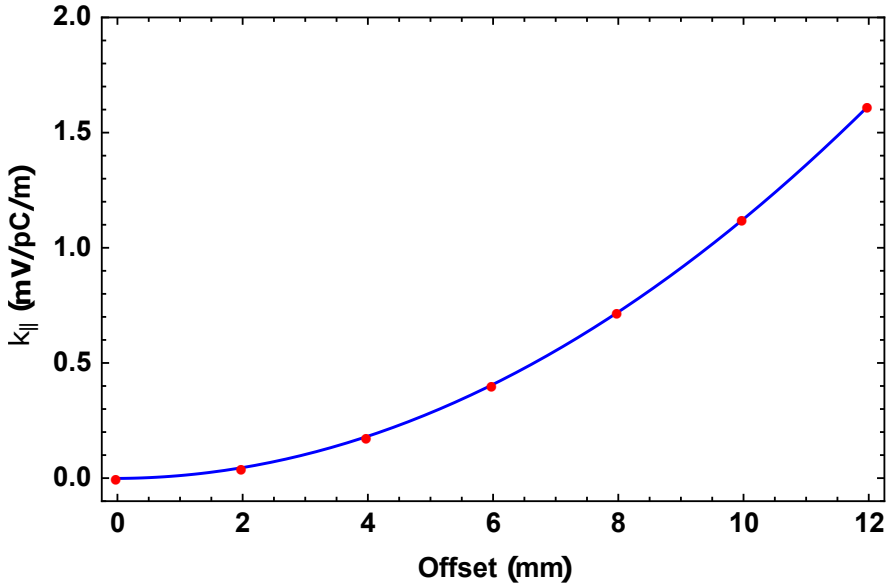

Figure 5.5: Variation of the loss factor for a dipole mode in a pillbox cavity with offset.

5.2.3 Floquet's Theorem

Most cavities are not single cells but a series of cells with opening which allow the cells to weakly couple so that a more efficient use of space is possible. This

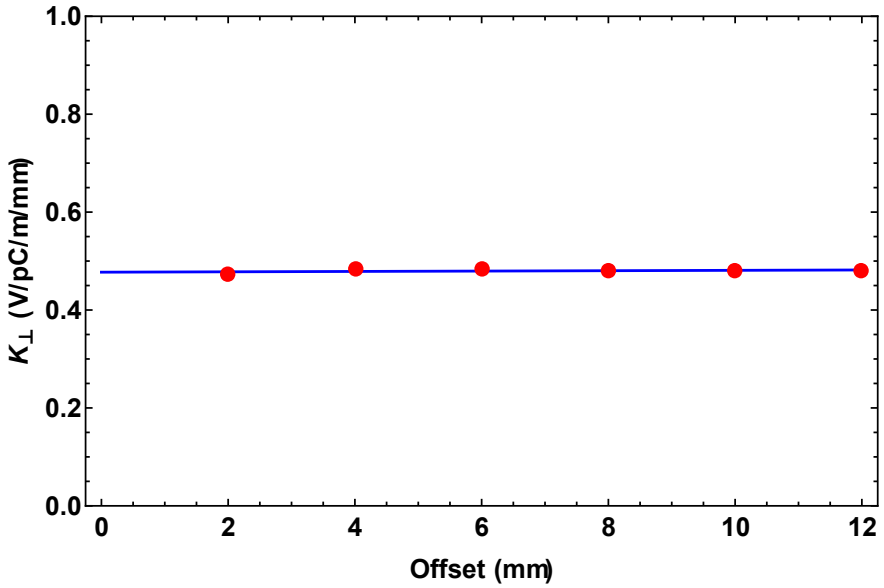

Figure 5.6: Variation of the kick factor for a dipole mode in a pillbox cavity with offset.

coupling leads to the breaking of the degeneracy of the modes and results in a passband forming [14]. In an infinitely long structure it is straightforward to see that the field can only vary by a complex phase, as when an infinite structure is shifted by a single cell length the field profile should not vary as the structure is unaltered by the transformation. This is known as Floquet's theorem and can be formally stated as

$$F_{n\pm1} = F_n e^{\pm i\phi} \tag{5.12}$$

where F_n is the periodic parameter and ϕ is the phase advance between adjacent components. Applying Floquet's theorem to the longitudinal electric field results in

$$E_z(r, \theta, z \pm L) = E_z(r, \theta, z) e^{\pm i\phi}, \tag{5.13}$$

which by applying the definition of the cosine function in terms of complex exponentials allows the phase advance per cell to be defined as

$$\cos(\phi) = \frac{E_Z(r,\theta,z+L) + E_z(r,\theta,z-L)}{2E_z(r,\theta,z)}. \tag{5.14}$$

An example of Floquet's theorem applied to the accelerating mode of a nine cell TESLA cavity is shown in figure 5.7. It can be seen that the field is flat and that the phase advance per cell in the structure is constant within the centre of the cavity. However in the end cell the phase advance changes as a result of the structures behaviour deviating form the infinite periodic behaviour seen in the mid cells due to the finite length of the structure.

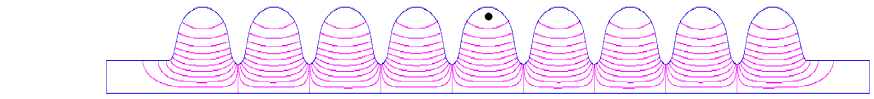

(a) Electric field profile

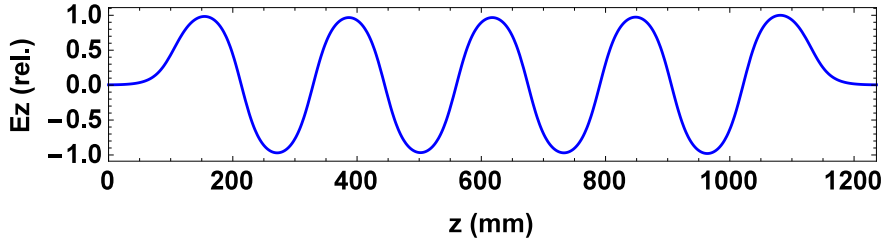

(b) $E_z(0,z)$

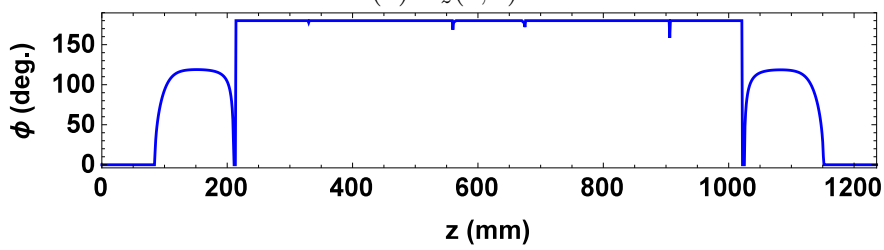

(c) Phase advance per cell along the nine-cell TESLA cavity.

Figure 5.7: Floquet's theorem applied to a nine-cell TESLA cavity simulated using the Superfish code.

5.3 The ESS Cavities

The SC section of the ESS linac (illustrated in figure 1.2) will consist of three families of SCRF cavities. Each of the three families of cavity are distinctly different and consequently have very different modal structures. It is important therefore to model each of these cavities accurately to determine the level at which beam excited HOMs are present. To this end a CAD model of each cavity obtained from colleagues at ESS [110] and is imported into the 3D EM solver HFSS and the HOM spectrum is found.

In each of the initial mode simulations the FPC is omitted as it is expected to have a minimal impact on the mode distributions and its damping effects can be accounted for by allowing Q_{ex} to be a free parameter in the first instance in the beam dynamics simulation in chapter 7.

In the proceeding sections details on the mode spectra and R/Q will be given for each cavity with the behaviour of modes within the accelerating passbands, HOMs with the largest R/Q and modes closest to harmonics of the bunch frequency being given particular attention.

Modes in the accelerating passband are expected to have a significant impact on the beam as they are close in frequency to the accelerating mode and can have R/Q's comparable to the accelerating mode in some cases. Further, it has been shown that if a HOM lies near to a harmonic of the bunch frequency then the beam can be degraded and/or have significant numbers of bunches being lost [85, 111]. In effect the instability in this case is resonantly driven.

In addition as $\beta \ll 1$ the variation of $R/Q(\beta)$ must be considered as it is possible that a mode is non-synchronous with the beam at β_g but may become synchronous at some point within a particular cavities velocity range.

5.3.1 The Spoke Cavity

The spoke section—which is the region of the accelerator containing spoke cavities—in the ESS linac will consist of 13 cryomodules, each housing two, 352.21 MHz double-spoke resonators with $\beta_g = 0.5$. Each cavity will operate with an accelerating gradient of up to 9 MV/m, however gradient's of up to 15.1 MV/m have been measured in vertical testing [112]. Figure 5.8 shows the accelerating mode of a two-spoke cavity simulated in Ansys HFSS.

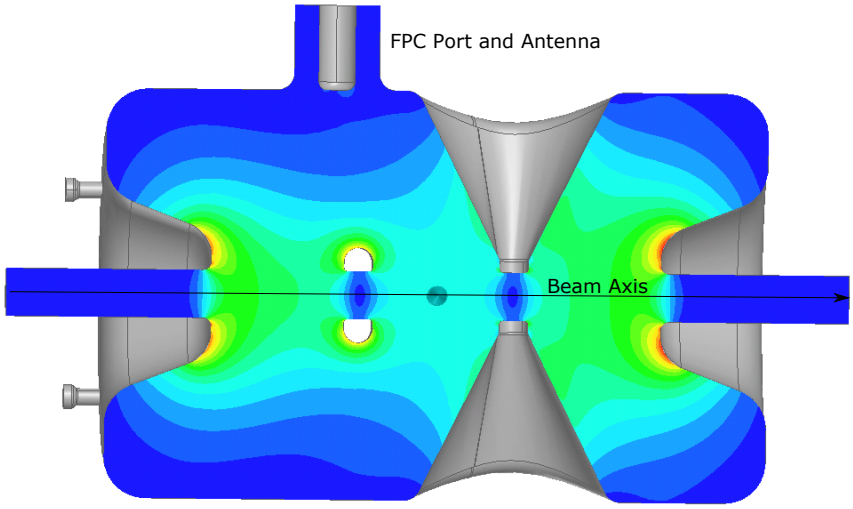

Figure 5.8: Electric field distribution of the accelerating mode in the ESS spoke cavity including the FPC antenna with high fields in red and low fields in blue.

The spoke cavities installed at ESS will be the first of their kind to be installed as a part of an operational machine. One of the main advantage of using spoke cavities at ESS is their large velocity acceptance which makes them particularly useful for accelerating low energy protons. This is due to the non-relativistic nature of protons at low energy resulting in significant velocity variations from cavity-to-cavity.

A modal analysis of the cavity has been performed in Ansys HFSS, from which the mode frequencies, loss parameters and R/Q's have been extracted. The

maximum longitudinal and transverse R/Q's are plotted in figures 5.9 and 5.10 for the first 100 modes of each type.

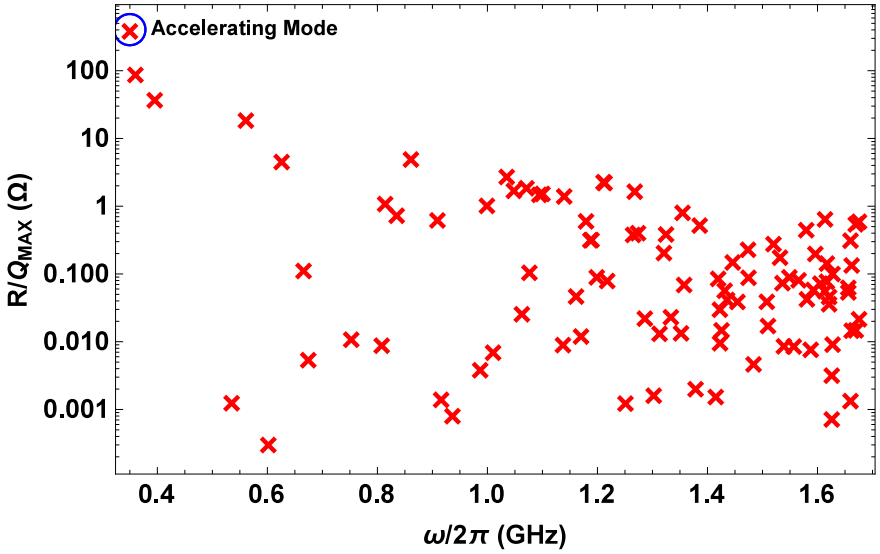

Figure 5.9: Maximum R/Q of the first 100 monopole modes in the two-spoke cavities at ESS.

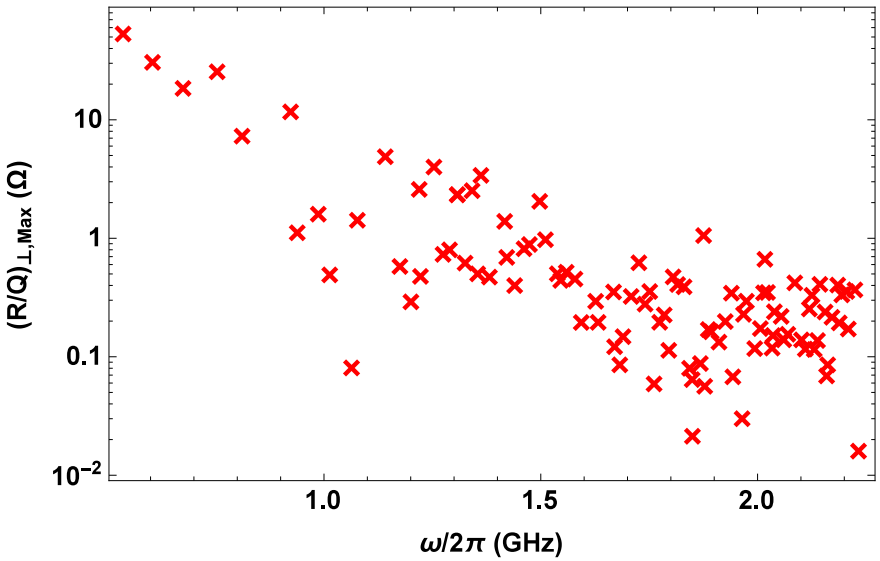

Figure 5.10: Maximum transverse R/Q of the first 100 transverse modes in the two-spoke cavities at ESS.

The accelerating mode stands out in figure 5.9 with significantly higher longitudinal R/Q compared to other modes. Aside from the passband modes, no

HOM has an R/Q greater than 30 Ω which is small when compared other SCRF cavities. For the transverse modes shown in figure 5.10 there are no modes which particularly stand out as having a significant R/Q, in addition it is clear there is a tendency for the R/Q to fall with increasing frequency. The most significant mode will be discussed in the next sections.

Spoke Cavity Passband Modes

Modes close to the accelerating mode, and with highest maximum R/Q are listed in table 5.3. The dependence of their R/Q on the bunch velocity is plotted in figure 5.11.

Mode	Freq. (MHz)	$\lvert f_n - f_\pi \rvert$ (MHz)	$R/Q(\beta_g)$ (Ω)	R/Q_{max} (Ω)
Acc. Mode	352.21	0.00	425.59	425.59
Mode 1	361.69	9.48	4.87	96.95
Mode 2	396.82	44.61	6.45	40.97

Table 5.3: Properties of the first three modes in the ESS spoke cavities.

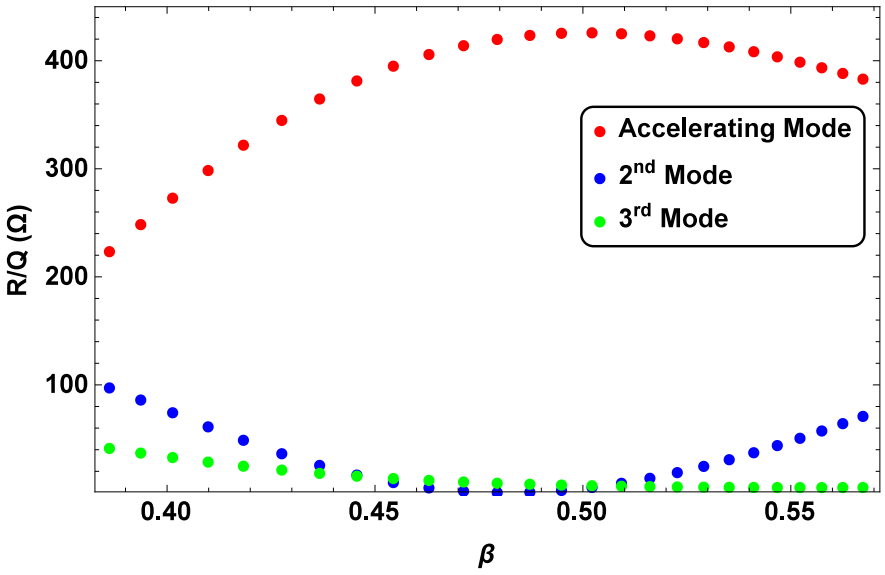

Figure 5.11: R/Q as a function of beam velocity in the spoke section of the ESS linac for the first three modes in the ESS spoke cavities.

The mode separation between the accelerating mode and the nearest neighbouring modes is large compared to what it would be in an elliptical cavities due to the high cell-to-cell coupling in the cavity. As a result of this the coherent effects from these modes which are often seen in elliptical cavities, should be of little concern in these cavities. At the start and end of the velocity range shown in figure 5.11 which corresponds to the spoke section of the ESS linac the 2nd mode in the cavities has a significant R/Q which is the same order of magnitude as the accelerating mode and as a result may impact on the beam.

Spoke Cavity HOMs

There are a large number of HOMs which can be present in a spoke cavity. The first 100 monopole modes have been simulated in HFSS and the properties of the modes with highest R/Q and those which are closest to harmonics of the bunch frequency are detailed in table 5.4. In addition details of the highest R/Q transverse modes are given in table 5.5.

Freq. (MHz)	$\lvert f_n - f_{ML} \rvert$ (MHz)	R/Q_{Max} (Ω)	$\sum R/Q$ (Ω)
562.52	141.90	20.52	238.73
1049.63	7.00	1.88	23.57
1064.22	7.59	0.03	0.48
1416.64	7.80	0.002	0.02

Table 5.4: Properties of the longitudinal modes in the ESS spoke cavities which are of most concern for machine operation.

Freq. (MHz)	$R/Q_{\perp}(\beta_g)$ (Ω)	$R/Q_{\perp,max}$ (Ω)	$\sum R/Q_{\perp}$ (Ω)
539.2	55.81	56.36	1329.48
607.25	23.91	32.45	521.58
756.32	9.31	27.03	271.93
677.67	1.66	19.56	139.55

Table 5.5: Details of the transverse HOMs of concern in the spoke cavity cavity.

The R/Q of the HOMs in this spoke cavity are relatively low in comparison

to the modes in other types of cavity which means they are expected to have little effect on the beam. There are several modes within 10 MHz of a machine harmonic which may be of concern. However, there is less risk associated with these due to the relative insensitivity of the HOMs to geometric perturbations due to the large cell-to-cell coupling of the cavity and also due to its low frequency.

5.3.2 The Medium-β Cavities

The medium-β section of the ESS linac will consist of nine cryomodules each containing four SCRF six-cell elliptical cavities operating at 704.42 MHz with a β_g of 0.67. The key parameters of the cavity are summarised in table 1.2 and further details of the design can be found in [113, 114]. Figure 5.12 shows the accelerating mode of the medium-β cavity simulated in Ansys HFSS. Figure 5.13

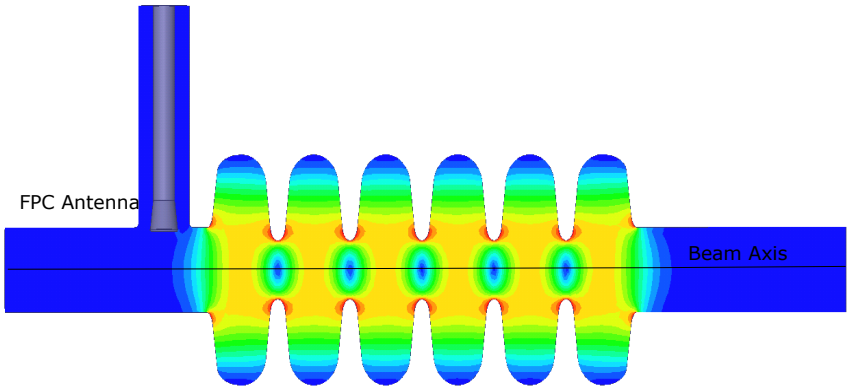

Figure 5.12: Magnitude of the electric field distribution of the accelerating mode in the ESS medium-β cavity including the FPC antenna. Regions of high field are shown in red and low field in blue.

shows the dispersion curves for the first 60 monopole and dipole like modes in the medium-β cavity simulated in HFSS without the FPC as its impact on the simulations is expected to be minimal. It can be seen that the accelerating mode is synchronous with the light line at the design velocity as expected.

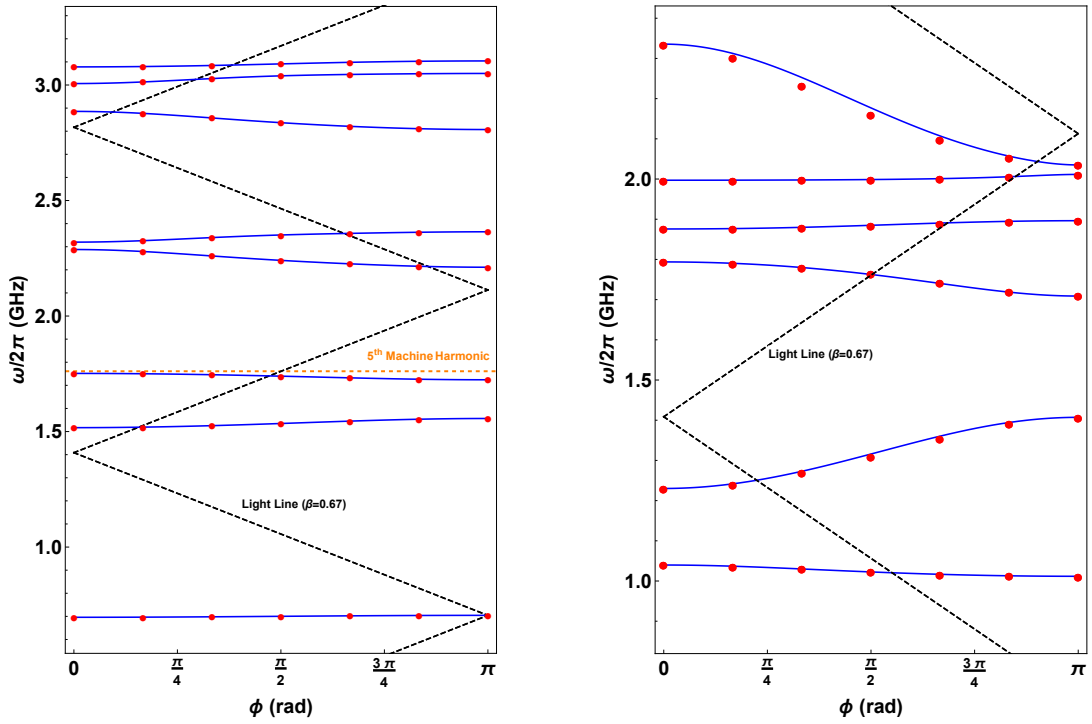

(a) Monopole (b) Dipole

Figure 5.13: Dispersion curves for the monopole and dipole modes of the ESS medium-β cavity. Full structure simulation are shown as blue triangles, single cell simulations as red circles and the solid line is the circuit model applied with infinite periodic conditions.

It is important to note that a mode in the third band is close to the 5^{th} harmonic of the bunch frequency (1761.05 MHz) and could potentially be shifted to lie on the 5^{th} harmonic due to manufacturing errors. The maximum R/Q value for each of the monopole modes is given in figure 5.14 and for transverse modes in figure 5.15. A more detailed summary of the modes of interest in terms of beam dynamics at ESS are given in sections 5.3.2 and 5.3.2.

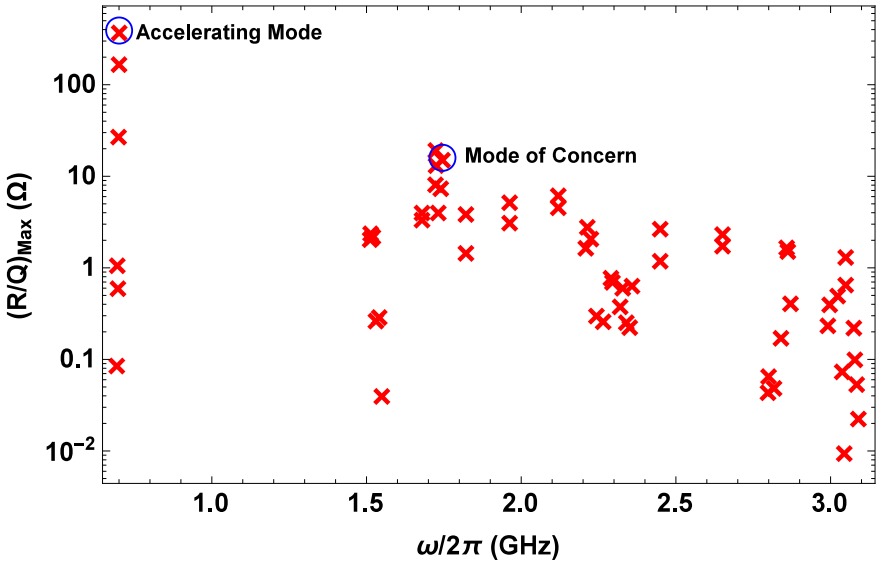

Figure 5.14: Maximum R/Q values for the first 60 monopole modes in the ESS medium-β cavity.

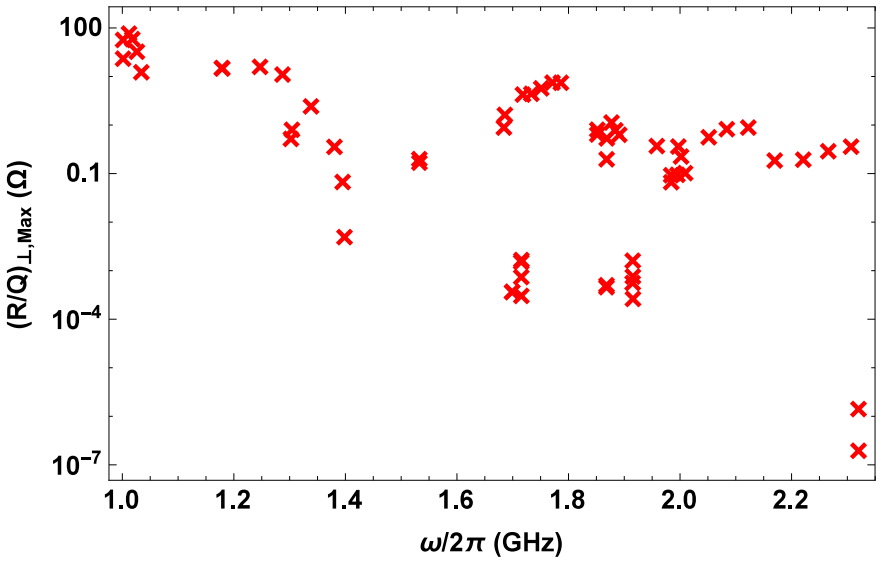

Figure 5.15: Maximum R/Q values for the first 60 dipole-like modes in the ESS medium-β cavity.

The Medium-β Cavity Passband Modes

The first monopole modes passband in the medium-β cavity contains six modes—one for each cell. Details of these modes are given in table 5.6 and the variation

of each modes R/Q with beam velocity is shown in figure 5.16.

Mode	Freq. (MHz)	$\lvert f_n - f_\pi \rvert$ (MHz)	$R/Q(\beta_g)$ (Ω)	R/Q_{max} (Ω)
$TM_{010,\pi/6}$	696.65	7.77	0.04	0.09
$TM_{010,2\pi/6}$	698.23	6.19	0.37	1.14
$TM_{010,3\pi/6}$	700.35	4.07	0.25	0.64
$TM_{010,4\pi/6}$	702.41	2.01	1.21	28.97
$TM_{010,5\pi/6}$	703.89	0.53	0.48	179.28
$TM_{010,\pi}$	704.42	0.00	366.84	397.77

Table 5.6: The frequency, R/Q and maximum R/Q in the medium-β cavity of the modes in the accelerating modes passband.

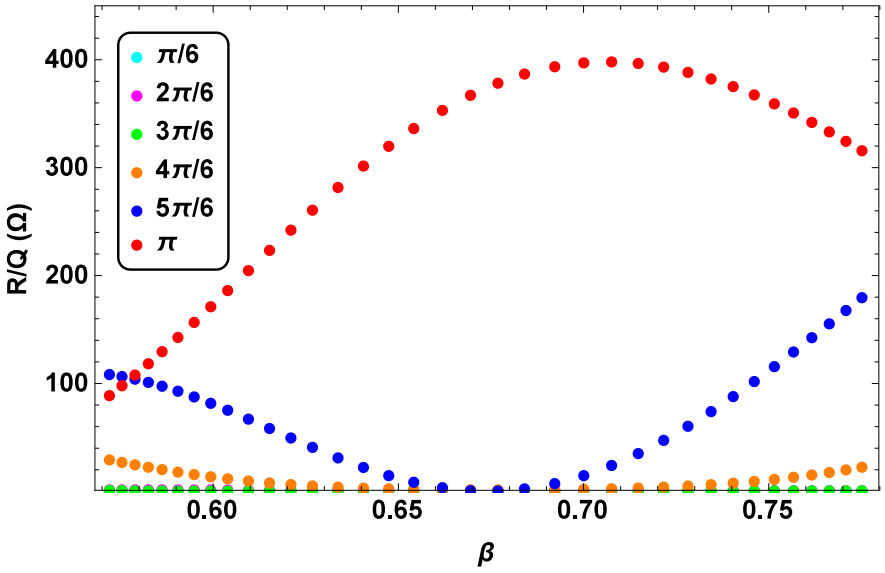

Figure 5.16: Variation of R/Q as a function of β for modes in the accelerating passband.

In table 5.6 the R/Q of the $5\pi/6$ mode is largest besides the accelerating mode. The variation of the R/Q of the passband modes is significant as shown in figure 5.16, in particular for the $5\pi/6$ mode. This mode has an R/Q comparable to the accelerating mode towards the start and end of the medium-β section of the linac. As a result of the small frequency separation and the high R/Q this mode has the potential to detrimentally affect the ESS beam.

The Medium-β Cavity Higher Order Modes

Details of the HOMs of concern in the medium-β cavity are given in table 5.7 for the longitudinal HOMs and table 5.8 for the transverse HOMs.

Freq. (MHz)	$\lvert f_n - f_{ML} \rvert$ (MHz)	R/Q_{max} (Ω)	$\sum R/Q$ (Ω)
1727.74	33.3	20.68	307.53
1749.57	11.5	16.21	119.55
1728.60	32.5	14.14	167.69
1726.87	34.2	8.74	110.35

Table 5.7: Details of the monopole HOMs of concern in the medium-β cavity.

Freq. (MHz)	$R/Q_{\perp}(\beta_g)$ (Ω)	$R/Q_{\perp,max}$ (Ω)	$\sum R/Q_{\perp}$ (Ω)
1014.17	16.56	88.66	1035.7
1003.65	0.19	77.22	786.02
1020.18	60.38	68.344	1570.8
1028.36	26.45	37.54	756.81

Table 5.8: Details of the transverse HOMs of concern in the medium β cavity.

The modes which have been identified are those which have the highest R/Q in the longitudinal and transverse planes, as well as the monopole modes which lie closest to a harmonic of the bunch frequency. Of the monopole modes identified, none have a particularly high R/Q and hence should have only a small effect on the beam. However the 1749.57 MHz mode is only 11 MHz away from the 5^{th} harmonic of the bunch frequency and if it shifts onto the 5^{th} harmonic it may pose beam dynamics issues as it would be resonantly excited.

All of the dipole modes identified have relatively low R/Q values so it is expected that the transverse wakefield excited would be very small and have little impact on the beam. This will be confirmed with beam dynamics simulation in chapter 7.

5.3.3 The High-β Cavity

The high-β section of the ESS linac will be made up of 84 five-cell elliptical SCRF cavities arranged into 21 cryomodules each containing four cavities. These cryomodules have been designed to be almost identical to those in the medium-β section, this is possible as the cavity lengths are almost identical. The high-β cavities will operate at a frequency of 704.42 MHz with a β_g of 0.86. Further details of the design of the cavities and of the prototype testing can be found in [114, 115]. The field profile of the accelerating mode in the high-β cavity is shown in figure 5.17.

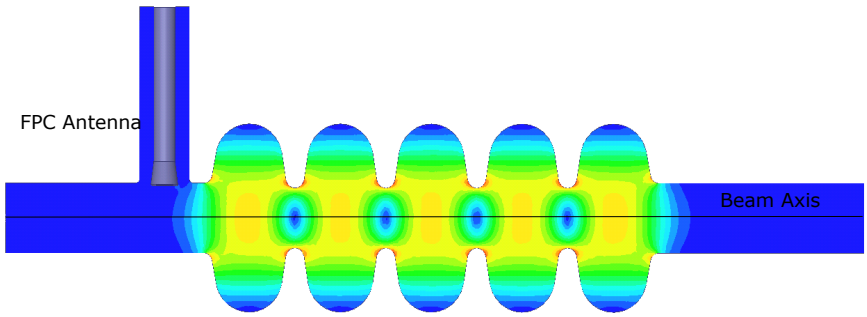

Figure 5.17: Magnitude of the electric field distribution calculated using HFSS, of the accelerating mode in the ESS high-β cavity including the FPC antenna. Regions of high field are shown in red and low field in blue.

The first 60 longitudinal and transverse modes have been simulated using HFSS without the FPC to allow for faster calculation through the use of symmetry planes. Dispersion curves for the lowest seven pass bands are displayed in figure 5.18.

The maximum values of R/Q for each longitudinal and transverse mode were calculated and plotted in figures 5.19 and 5.20 respectively.

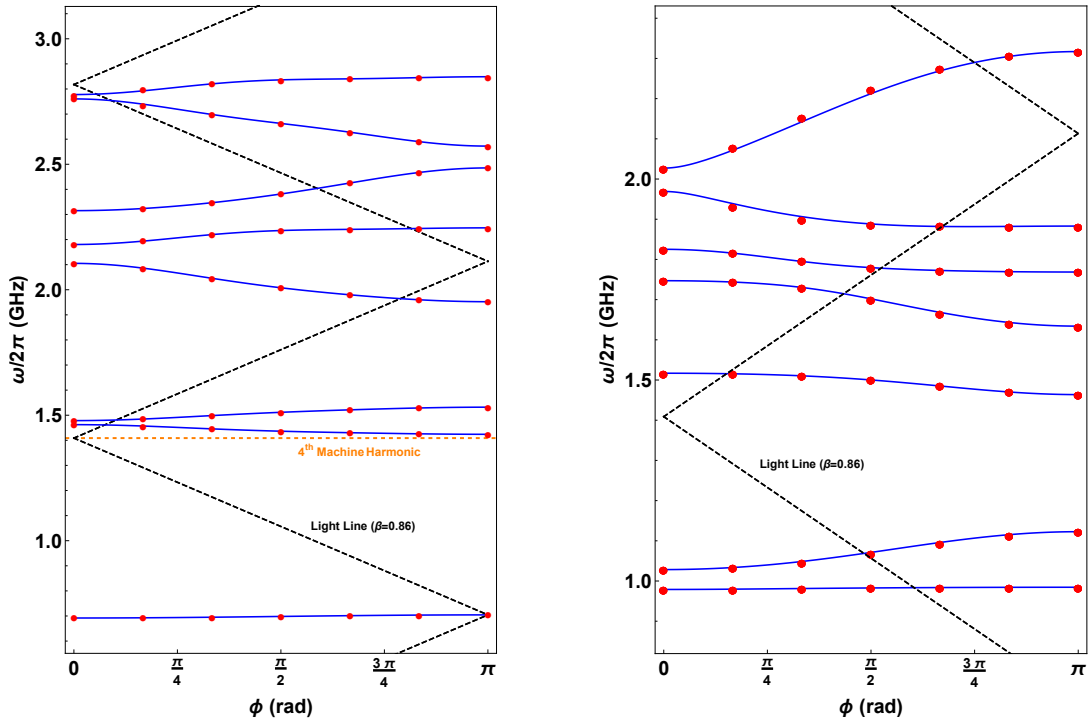

(a) Monopole (b) Dipole

Figure 5.18: Dispersion curves for the monopole (left) and dipole (right) modes of the ESS high-β cavity. Single cell simulations are displayed as red circles and the solid line indicated the circuit model applied with infinite periodic conditions. The 4$^{\text{th}}$ harmonic of the bunch frequency is highlighted as a dashed orange line.

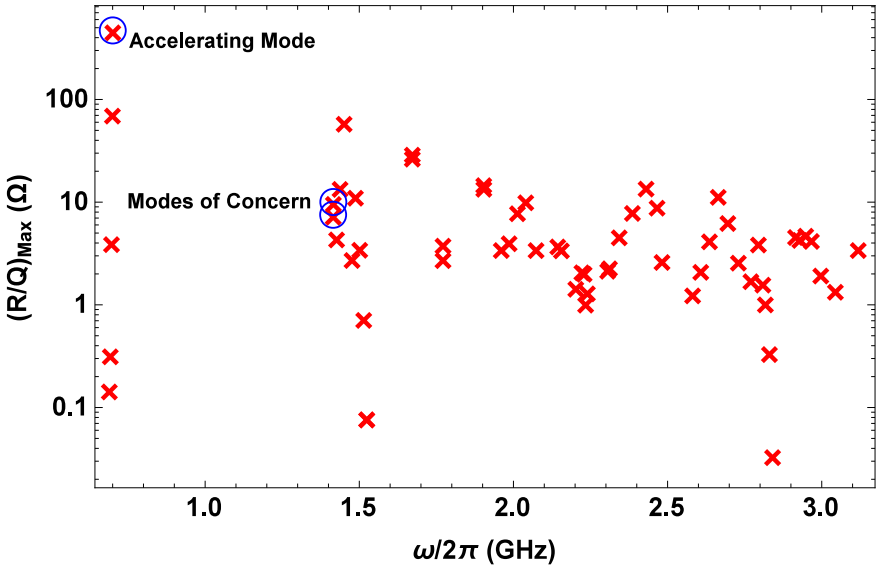

Figure 5.19: Maximum R/Q values for the first 60 monopole modes in the ESS medium-β cavity.

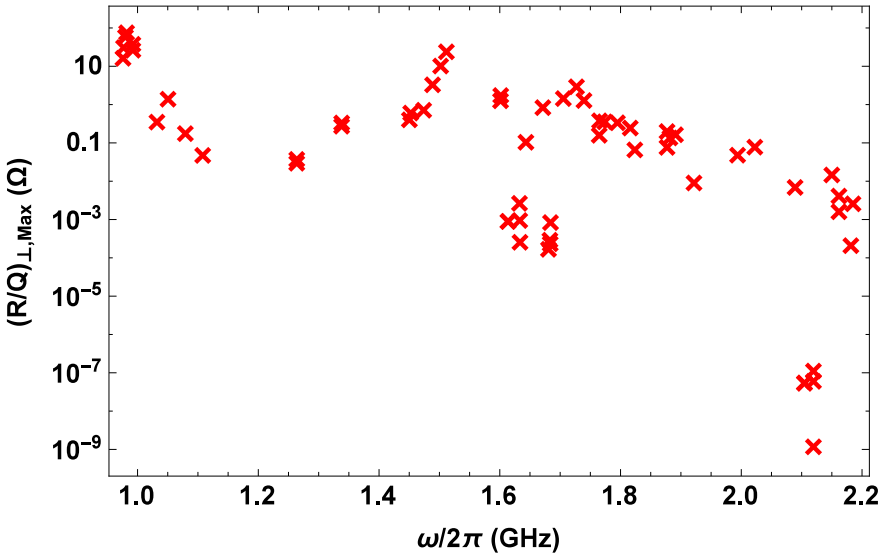

Figure 5.20: Maximum R/Q values for the first 60 dipole like modes in the ESS medium-β cavity.

The dispersion curve in figure 5.18 shows the 2$^{\text{nd}}$ monopole band is close to the 4$^{\text{th}}$ harmonic of the bunch frequency (1408.84 MHz). Modes in this region could potentially be resonantly driven if a HOM shifts closer to the 4$^{\text{th}}$ harmonic and hence these modes are of particular interest.

The High-β Cavity Passband Modes

The passband of the accelerating mode in the high-β cavity contains five modes. Details of these modes are given in table 5.9. The R/Q of the $4\pi/5$ mode is the largest by a significant margin and will have the most impact on the beam.

Mode	Freq. (MHz)	$\lvert f_n - f_\pi \rvert$ (MHz)	$R/Q(\beta_g)$ (Ω)	R/Q_{max} (Ω)
$TM_{010,\pi/5}$	693.14	11.28	0.02	0.15
$TM_{010,2\pi/5}$	696.26	8.16	0.07	0.33
$TM_{010,3\pi/5}$	700.12	4.31	0.22	4.14
$TM_{010,4\pi/5}$	703.22	1.20	0.15	73.86
$TM_{010,\pi}$	704.40	0	435.84	477.87

Table 5.9: The frequency, R/Q and maximum R/Q in the high-β cavity of the modes in the accelerating modes passband.

The variation of the R/Q of the passband modes with the beam velocity within the high beta section of the ESS linac are illustrated in figure 5.21. Throughout the velocity range, the R/Q's are always well below that of the accelerating mode and are small compared to that of the medium-β cavities passband modes. The reduced R/Q in conjunction with the larger frequency separation, compared to the medium-β cavities means the impact of this mode is expected to be smaller than that of the $5\pi/6$ mode in the medium-β cavity.

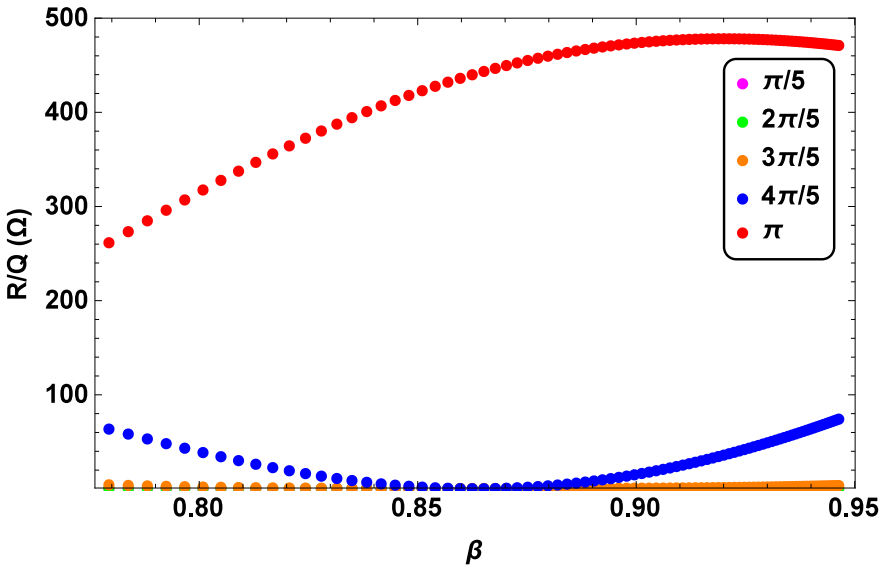

Figure 5.21: Variation of R/Q as a function of β for modes in the accelerating modes passband.

The High-β Cavity Higher Order Modes

Details of the HOMs of concern in the high-β cavity are given in tables 5.10 and 5.11. The R/Q of the longitudinal modes are relatively small and are anticipated to have only a limited impact on the beam. However, there are two modes which lie close to the 4^{th} harmonic of the bunch frequency (1408.84 MHz) which may be of concern. The transverse modes have very small R/Q values compared to higher frequency cavities.

Freq. (MHz)	$\lvert f_n - f_{ML} \rvert$ (MHz)	R/Q_{max} (Ω)	$\sum R/Q$ (Ω)
1454.67	45.85	61.50	4120.86
1675.91	85.14	30.77	1529.21
1419.23	10.39	7.65	390.97
1419.82	10.98	10.19	354.65

Table 5.10: Details of the monopole HOMs of concern in the high-β cavity.

Freq. (MHz)	$R/Q_{\perp}(\beta_g)$ (Ω)	$R/Q_{\perp,max}$ (Ω)	$\sum R/Q_{\perp}$ (Ω)
982.06	70.27	70.27	5284.72
983.93	41.28	90.52	4949.48
994.29	22.91	23.59	1785.51
1513.71	18.44	28.79	1865.23

Table 5.11: Details of the transverse HOMs of concern in the high-β cavity.

5.4 Wakefields in the ESS Cavities

The wakefield of a cavity can be investigated using either a wakefield solver—such as CST or GdfidL—or through the modal summation method [116]. Wakefield solver calculations, most of which assume $v = c$ are computationally expensive and ultimately limited by the simulation time. Further, simulations for $\beta < 1$ are even more time consuming—due to the presence of static fields in the vicinity of the bunch itself—and there are fewer available codes for this purpose. One of the few solvers able to perform these calculations is CST MWS. The modal summation technique however, allows for the calculation of the wakefield at any β once $k_{\parallel/\perp,n}(\beta)$ is known for the dominant modes at a particular β by applying equations 3.6 and 3.8. This method has been shown to be valid for all β once the exciting charge has left the cavity [116]. The envelope of the long range transverse and longitudinal wakefields of each of the ESS cavities calculated from the magnitudes of equations 3.6 and 3.8 are shown in figure 5.22 for a Q_L of 10^6.

The magnitude of the wakefield in each cavity of ESS is small in comparison to that of the higher frequency cavities commonly seen which operate at frequencies

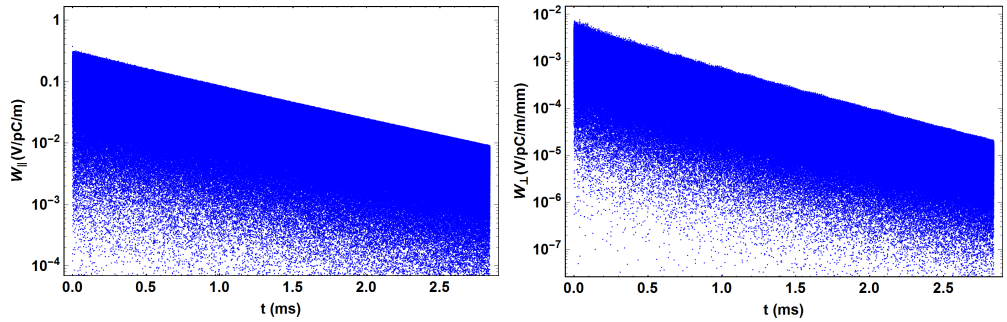

(a) $W_{\parallel}$ spoke cavity

(b) $W_{\perp}$ spoke cavity

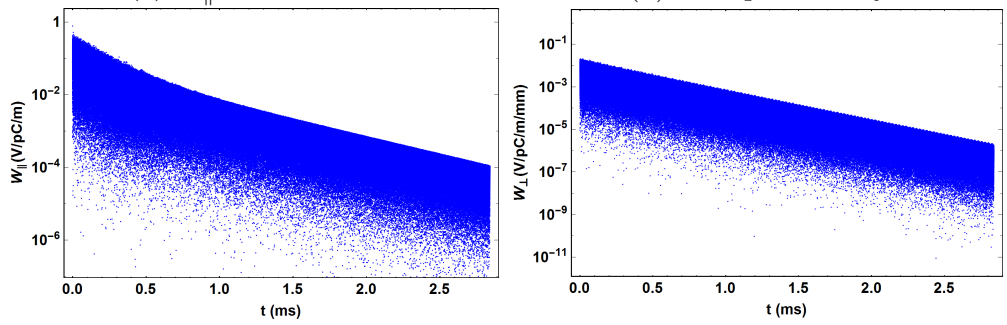

(c) $W_{\parallel}$ medium-β cavity

(d) $W_{\perp}$ medium-β Cavity

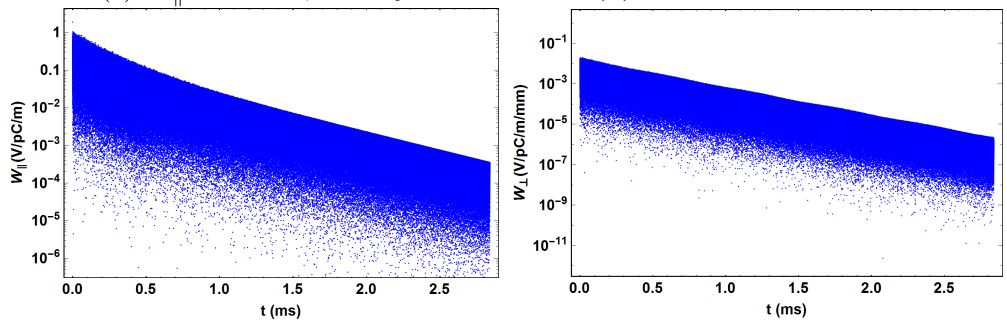

(e) $W_{\parallel}$ high-β Cavity

(f) $W_{\perp}$ high-β Cavity

Figure 5.22: Envelope of the wakefield in the ESS cavities sampled at the bunch spacing (1/352.21 MHz) over the length of the whole ESS bunch train of 1 million bunches with all modes having a $Q_{ex} = 10^6$ imposed.

of 1 GHz or more [16, 117]. This reduced amplitude is expected due to frequency scaling. The magnitude of the longitudinal wakefield scales with frequency as ω^2 and the transverse as ω^3 and is detailed in appendix C. The magnitude of the wakefield can be characterised by the looking at the sum of the loss/kick factors which are shown in table 5.12.

The total loss and kick factors are relatively low and for a worst case where

Parameter	Units	Spoke	Medium-β	High-β
f_{Acc}	MHz	352.21	704.42	704.42
k_{Acc}	V/pC/m	0.173	0.408	0.569
$\sum k_{n,\parallel}$	V/pC/m	0.358	1.02	1.51
$\sum K_{n,\perp}$	V/pC/m/mm	0.007	0.013	0.012

Table 5.12: The sum of the loss and kick factors (excluding the accelerating mode) in the ESS cavities when the sum of loss factors is greatest neglecting the accelerating mode.

in each ESS cavity the maximum loss factor was experienced this would result in a total energy loss for a bunch of 30 keV which is small compared to the spread in energy at injection and the accelerating voltages of each of the cavities. This would therefore have only a minimal impact on the exciting bunch itself at ESS.

However the impact of the excited field on trailing bunches is of much more interest as the driven excitation of modes could result in bunches at the tail of the bunch train experiencing high fields caused by bunches at the head of the train. This long-range driven wakefield has been investigated using the sum of the modal wakefield.

5.4.1 Sum Wakefield of the ESS Cavities

The sum wakefield allows for the summation of the phasors excited by individual bunches within the bunch train over the full length of the bunch train. This has been performed for the full ESS bunch train of 1 million bunches at a bunch frequency of 352.21 MHz with the first 60 modes included in both the longitudinal and transverse planes for the elliptical cavities. For the spoke cavities the first 100 modes have been included in each case. For the longitudinal calculations the accelerating mode has been omitted as in normal operation this is on a harmonic of the bunch frequency and will be resonantly driven resulting in a resonant growth which will hide the behaviour of the other mode. This is reasonable as

the beam loading in the accelerating mode is compensated for by controlling the power supplied to the cavities.

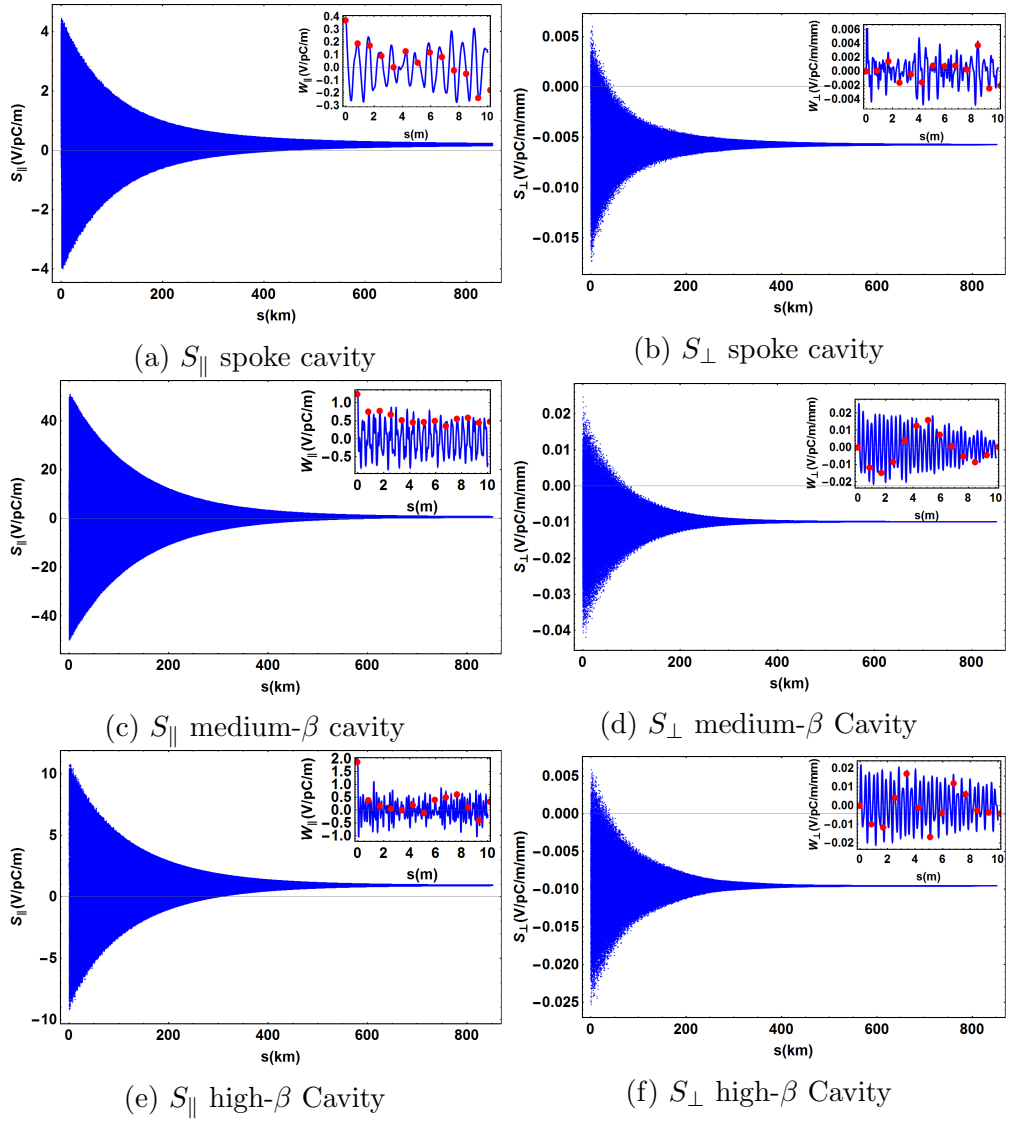

(a) $S_{\parallel}$ spoke cavity

(b) $S_{\perp}$ spoke cavity

(c) $S_{\parallel}$ medium-β cavity

(d) $S_{\perp}$ medium-β Cavity

(e) $S_{\parallel}$ high-β Cavity

(f) $S_{\perp}$ high-β Cavity

Figure 5.23: The sum wakefield in the ESS cavities sampled at the bunch spacing (0.86 m) over the length of the whole ESS bunch train of 1 million bunches with all modes having a $Q_{ex} = 10^6$. Inset is the wakefield excited by the first bunch with the arrival point of subsequent bunches as red dots.

The longitudinal and transverse sum wakefield for each type of cavities are shown in figure 5.23. In each case the value of the sum wakefield rises before oscillating towards a steady state at which the magnitude is almost constant. This

steady state is a result of the excited field from each of the bunches cancelling out and the time taken for this to occur is a consequence of both the bunch frequency and also the Q_{ex}.

In each case the amplitude of the transverse wakefield is particularly small and is at a level which would be expected to have a minimal impact on the beam. A similar thing can be seen in the case of the longitudinal sum wakefield where in this case the steady state magnitude is slightly higher but unlikely to have a significant impact on the beam. However in the elliptical cavities a significant voltage is present in the early part of the bunch train. This is caused by the mode closest to the accelerating mode in the first passband, which has a frequency close to that of the accelerating mode.

This analysis is in the ideal case where each bunch arrives at a fixed spacing and the excited HOMs are at well known frequencies which do not vary. For a real system the bunch arrival times will vary and also manufacturing errors may shift the frequencies of the HOMs. Further the frequency of each HOM will shift throughout each pulse as a result of Lorentz force detuning. These issues require much greater consideration and will be discussed in more detail in the following chapters.

5.5 Determination of the Q_{ex} in the Elliptical Cavities

The role of the FPC is to transfer RF power from the source to the cavity. This is achieved by matching the impedance of the coupler to the cavity-beam system thus minimising the power reflected by the cavity. The FPC in the case of the ESS elliptical cavities is located in the beam pipe. In addition to its role in

providing power to the accelerating mode it is likely that the FPC will couple to some degree to the beam-excited HOMs as well. This coupling will reduce the Q_{ex} of the HOMs and act as a damping mechanism and indeed may significantly reduce the impact of HOMs on the beam and the heat load of the cavity. In this section the Q_{ex} of the modes in the accelerating passband and the HOMs closest in frequency to harmonics of the bunch frequency are calculated. One means to calculate the Q_{ex} is the Balleyguier method.

5.5.1 The Balleyguier Method

The Balleyguier method [118, 119] enables the Q_{ex} to be calculated directly from eigenmode simulations of a closed cavity-coupler system. This method relies on using two eigenmode solutions to reconstruct the travelling wave in the coupler by changing the boundary conditions at the terminating plane. This is shown schematically in figure 5.24.

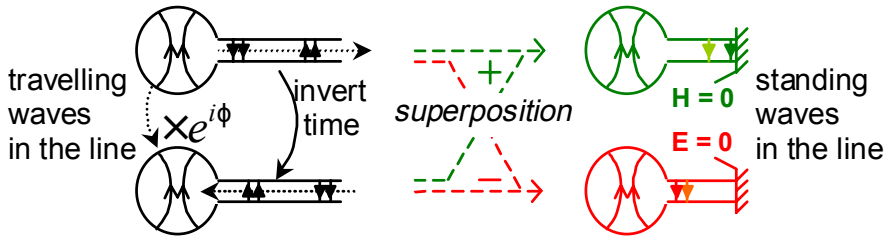

Figure 5.24: Superposition of two time inverted travelling wave solutions to form standing waves in the transmission line [118].

This method begins by considering a lossless cavity containing stored energy, U at the resonant frequency, ω. If the coupler is connected to an infinite transmission line then the cavity looses power, P to the line. The power can be calculated by

$$P = \frac{1}{2Z_0}\int_S |\vec{E}|^2 dS = \frac{Z_0}{2}\int_S |\vec{H}|^2 dS, \tag{5.15}$$

where $Z_0 = \sqrt{\mu_0/\epsilon_0}$ is the impedance of free space and the integrals are over the cross-section of the transmission line. The stored energy of the cavity is given by

$$U = \frac{\mu_0}{2}\int_V |\vec{H}|^2 dV = \frac{\epsilon_0}{2}\int_V |\vec{E}|^2 dV. \tag{5.16}$$

This lead to the definition of Q_{ex} as

$$Q_{ex} = \frac{\omega U}{P} = \frac{\omega \int_V |\vec{E}|^2 dV}{c\int_S |\vec{E}|^2 dS} = \frac{\omega \int_V |\vec{H}|^2 dV}{c\int_S |\vec{H}|^2 dS}, \tag{5.17}$$

for a TEM mode in the transmission line. In the transmission line two travelling waves transfer power in both directions where they interfere to form a standing wave. If the solution with the electric field at a maximum on the terminating plane is considered the amplitude of the wave is twice that of the individual travelling waves. The two fields inside the cavity have a phase difference ϕ, and the resulting amplitude is now $|1 + e^{j\phi}|$ larger than the original. The parameter Q_1 can then be defined as

$$Q_1 = \frac{\omega \int_V |\vec{E}|^2 dV}{c\int_S |\vec{E}|^2 dS} = \frac{|1 + e^{j\phi}|^2}{4} Q_{ex} \tag{5.18}$$

where the transmission line is shorted by a perfect magnetic boundary. This is readily calculable in an appropriate RF eigenmode code such as HFSS.

Now consider the same system with the magnetic field at a maximum on the terminating plane. The amplitude of the resulting field is now $|1 - e^{i\phi}|$ times the original and Q_2 can be defined as

$$Q_2 = \frac{\omega \int_V |\vec{H}|^2 dV}{c\int_S |\vec{H}|^2 dS} = \frac{|1 - e^{j\phi}|^2}{4} Q_{ex}. \tag{5.19}$$

The terminating plane in this case is a perfect electric wall and the solution is

again readily calculable in an appropriate code. The Q_{ex} can the be identified as the sum of these components,

$$Q_{ex} = Q_1 + Q_2 \tag{5.20}$$

which is independent of ϕ as $|1 + e^{j\phi}|^2 + |1 - e^{j\phi}|^2 = 4$. This method therefore requires two simulations in an RF solver to find the Q_{ex}.

In the next section the Balleyguier method is applied to the ESS elliptical cavities including the FPC as shown in figures 5.12 and 5.17.

5.5.2 The ESS Cavity Q_{ex}

Shown in tables 5.13 and 5.14 are the values for Q_{ex} for the modes in the first passband and also the HOMs which are closest to in frequency to harmonics of the bunch frequency. The Q_{ex} of the modes in the accelerating passband are all at the level of 7.5×10^5 which is specified for the accelerating mode [36]. This is as expected as the frequency of all of these modes are close to the accelerating modes frequency.

Freq. (MHz)	Q_{ex} Balleyguier Method	Q_{ex} PML Boundary
696.65	6.4×10^6	6.4×10^6
698.23	1.7×10^6	1.7×10^6
700.35	8.2×10^5	8.0×10^5
702.41	5.3×10^5	5.2×10^5
703.89	4.2×10^5	4.1×10^5
704.42	7.8×10^5	7.7×10^5
1749.57	2.2×10^6	3.1×10^5

Table 5.13: Q_{ex} of the medium-β cavity using the Balleyguier method and PML boundary.

For the HOM's in the medium-β cavity the $Q_{ex} > 10^6$ and the damping provided by coupling to the FPC is low. This is due to the fact that the field in

Freq. (MHz)	Q_{ex} Balleyguier Method	Q_{ex} PML Boundary
693.14	4.4×10^6	4.3×10^6
696.26	1.2×10^6	1.2×10^6
700.12	6.0×10^5	6.1×10^5
703.22	4.4×10^5	4.4×10^5
704.40	7.7×10^5	7.7×10^5
1419.25	3.7×10^3	7.4×10^3
1419.78	2.4×10^2	9.9×10^2

Table 5.14: Q_{ex} of the high-β cavity using the Balleyguier method and PML boundary.

this mode is concentrated in the central cells away from the coupler.

The case for the HOMs in the high-β cavity is different as the most of the field is in the end-cells and hence the coupling to te FPC is significant. This results in $Q_{ex} < 10^4$ which for an SCRF cavity is similar to that achieved using HOM couplers [14]. As a result there is a strong indication that damping from the coupler may be able to mitigate the impact of the HOMs.

It must be noted that these simulations are of the absolute best case when the transmission line is perfectly matched along an infinite length. In a real accelerator like ESS, there are additional pieces of RF equipment which will prevent this being the case. These include the doorknob transition which couples the coaxial line to the waveguide system, bends in the waveguide and the circulator which protects the RF amplifier, each of these is matched at 704.42 MHz but not necessarily at any other frequency.

5.5.3 The Doorknob Transition

The power from the source is transmitted to the elliptical cavities through a system of WR1150 waveguide [36], the power is then coupled to the cavity by a coaxial coupler. As a result there must be a waveguide-to-coax transition which in the case of ESS takes the form of a doorknob transition (see Figure 5.25). This

transition is narrow band and as such off-frequency power may have a significant impedance miss-match at the transition. Figure 5.25 shows a model in HFSS containing the high-β cavity, doorknob transition and a length of waveguide.

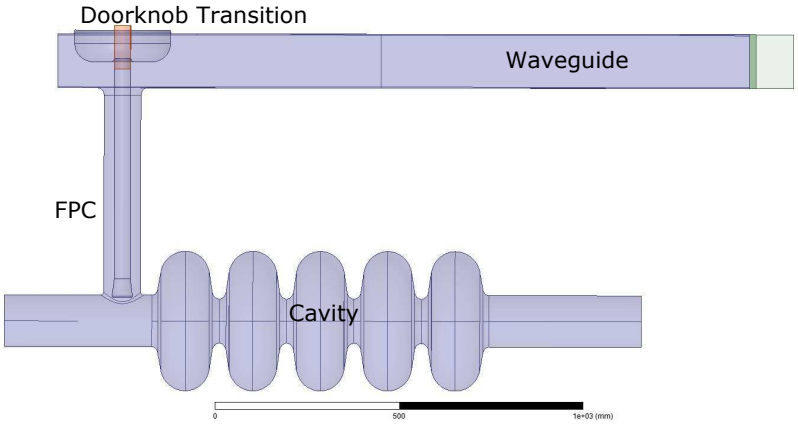

Figure 5.25: Model of the cavity-doorknob system drawn in HFSS [120].

To determine if the HOMs are able to be damped by the FPC the whole system is simulated, firstly for the accelerating mode to compare the accuracy as it should be perfectly matched and then for the HOMs. The waveguide used in the simulation is terminated with PML giving perfect matching. The real system contains an RF window and has some 30 m of waveguide terminated by a circulator going to an RF load which have not been included. As these have not been simulated the Q_{ex} values extracted from these simulations represent a best case scenario and could be subject to significant variation.

Freq. (MHz)	Q_{ex} PML Boundary
704.49	7.8×10^6
1419.46	6.4×10^3
1419.97	2.7×10^3

Table 5.15: Q_{ex} of the high-β cavity including the doorknob transition calculated by HFSS using PML to terminate the waveguide.

The Q_{ex}'s given in table 5.15 show only small changes from when the coax was assumed to be infinite. This suggests that there is a miss-match present

but power is still able to propagate through the system which strongly suggests significant damping is present. The only other calculation of these values is given in [90] where the RF window and bellows were included but not the doorknob. For the accelerating mode and the 1419.97 MHz mode the results are consistent. However, for the 1419.46 MHz mode they differ by over an order of magnitude. This therefore means the resulting numbers must be taken with some caution as with any Q_{ex} calculation. These numbers give an indication that damping is present but the level will ultimately need to be determined experimentally. In the next section the sensitivity of the HOM frequencies in the medium-β cavity to geometric errors will be analysed with both eigenmode simulation and with an equivalent circuit model.

5.6 Manufacturing Errors and Mode Sensitivity

The ESS linac accelerates a train of 1 million bunches. There is the potential for this bunch train to resonantly drive the voltage in each of the HOMs. In most cases this leads to the magnitude of the HOM voltage oscillating until a steady state is reached. However if the frequency of the HOM lies on a harmonic of the bunch frequency, the HOM voltage will continue to build. Due to the high Q_{ex} of HOMs in SCRF cavities—resulting from the lack of HOM couplers—resonant excitation can lead to very high HOM fields building up inside the cavity and this can severely degrade the beam quality.

As the ESS will not use HOM couplers, the cavities have been carefully designed such that all HOMs are more than 5 MHz away from the nearest machine harmonic. However in the process of manufacturing 146 SCRF cavities, manufacturing errors are unavoidable. The errors expected are appreciable due to the processes which are employed when shaping high purity niobium for RF appli-

cations. For example copper can be accurately machined to better than 10 μm with diamond point tooling, whereas the errors in the deep drawing process using niobium are expected to be in the 100's μm region. This issue was highlighted by the first prototypes of the high-β cavities which met the ESS requirements for the accelerating mode. However, the HOMs of concern in the 2$^{\text{nd}}$ passband were shifted to lie on the 4$^{\text{th}}$ machine harmonic [114]. This shift was result of a significant deviation in the geometry of the end cells. Mechanical geometric examination revealed that the cavity geometry was deviated by 1.2 mm from the design.

The errors resulting from the manufacturing process will be both random and systematic. Predictions regarding the frequency shifts are indeed statistical in nature and will require a full suite of simulations. To obtain the necessary data would be impractical with HFSS. Here we employ a circuit model which calculates the resonant frequencies and eigenmodes rapidly. In this method we can obtain the results for various errors including statistically distributed error quickly.

A circuit model has been used in conjunction with simulations performed using SF and ANSYS HFSS. In this analysis the focus has been the medium-β cavity which is expected to be the largest contribution to beam degradation due to its position in the linac and the fact that the R/Q is greater than for those in the high-β cavities.

5.6.1 Single Cell Sensitivity

In order to assess the frequency sensitivity of the design to manufacturing errors it is simplest to look at the frequency sensitivity on a single cell due to errors in the seven parameters which are used to define the geometry shown in figure 2.5. Here frequency sensitivity refers to the shift in the resonant frequency of the

mode due to specific geometric parameters of the design. To achieve this each of the seven parameters were varied in steps of 0.1 mm between ±2 mm around the design value in ANSYS HFSS. In these simulations a 10 degree slice of the cavity was simulated and the frequency of the first three monopole modes were recorded. The relative sensitivity of the modes to each parameter were found to be linear in this regime and the relative sensitivity of the first three bands is summarised in table 5.16.

Parameter	A	B	L	a	b	R_{eq}	R_I
Mode 1	-3.31	0.90	2.38	-2.46	0.39	-4.34	1.32
Mode 2	0.40	0.75	-2.04	1.15	0.04	-8.81	2.68
Mode 3	-18.7	2.67	-7.77	6.66	-0.26	-3.20	1.17

Table 5.16: Sensitivity of the modes in a single cell of the medium-β cavity with a phase advance of π applied to variations in the cavity geometry in MHz/mm.

The sensitivity of each of the HOMs is greater than that of the accelerating mode in most cases and is particularly large for the equator ellipse eccentricity A where the 3$^{\text{rd}}$ mode is six times more sensitive than the accelerating mode. In several parameters the HOM behaves in an opposite fashion to that of the accelerating mode (i.e. the frequency of the accelerating mode falls whilst the HOMs rises). This behaviour highlights that the accelerating mode could be tuned correctly whilst the HOM is shifted significantly in frequency towards a harmonic of the bunch frequency. This was found in the high-β prototypes [114].

These results can be illustrated by plotting the Slater parameter [121];

$$\frac{\delta\omega}{\omega} = -\frac{\int_{\Delta V} (\mu|H|^2 - \epsilon|E|^2)\, dV}{\int_V (\mu|H|^2 + \epsilon|E|^2)\, dV} \tag{5.21}$$

of each mode and looking at regions where this parameter is largest. The Slater parameter relates the frequency shift of a mode to the change in the electric and magnetic energy stored in the region which is added/removed. if the volume in

region with high magnetic field is contracted, the frequency will decrease whereas removing a region of high electric field will cause it to rise. The Slater parameters for the first three monopole modes are show in figure 5.26.

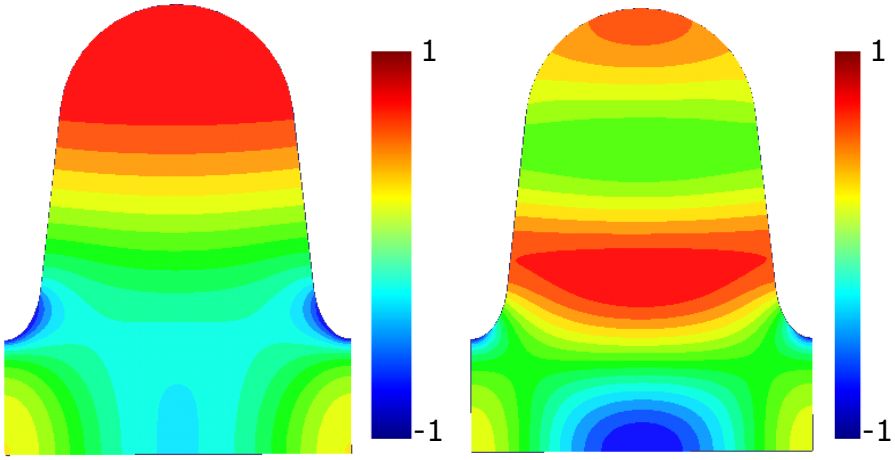

(a) Accelerating Mode (b) 2nd Mode

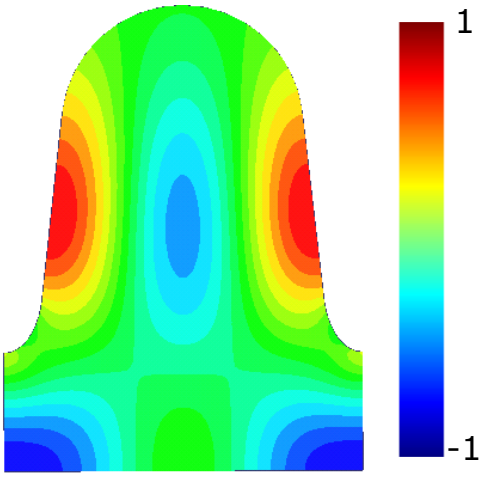

(c) 3rd Mode

Figure 5.26: Normalised Slater parameter plotted for the first three monopole modes.

From figure 5.26, regions where the Slater parameters behave very differently can be identified, particularly the behaviour of the 3rd mode near the cell wall compared to the accelerating mode. This suggests that there is a particular

sensitivity from the HOM to the wall angle. This is the mode which may shift to the machine line and hence it is important to be aware of this. The conclusions from simulations are supported by the Slater parameter in different regions.

5.6.2 Full Structure Sensitivity

In the single cell case there are 14 free parameters (seven per half cell) and only three modes need to be simulated. Whereas, in the case of a full six-cell cavity there are 74 free parameters and populating such a large parameter space is impractical. To allow some insight into the effects a simplified model is required and the circuit model of accelerating cavities is the tool that provides simplicity and speed of analysis. The circuit model used is described in section 4.3 and a comparison between the circuit model and HFSS is given in this section.

A circuit model was developed and the results fitted to the EM simulations of the single cells at fixed phase advances performed in HFSS. The result was then cast into matrix form and the end-cell coupling was found by minimising the difference between the eigenmodes of the full structure and the circuit predictions by varying only the beampipe coupling.

A comparison of the frequencies extracted from HFSS and the circuit model are given in tables 5.17 and 5.18. The field profiles and the eigenvectors are then shown in figures 5.27 and 5.28. Good agreement was found for the 2^{nd} band, with maximum frequency difference less than 0.31 MHz (0.02%). However in the 3^{rd} band the agreement was not as good, because the modes are above the beam pipe cut-off and no longer confined within the cavity. The $5\pi/6$ mode which is of interest in this band is however trapped, and the eigenvector and eigenvalue for this mode are in agreement with the full cavity simulations. Consequently information on the modes sensitivity to errors can still be gleaned from the circuit

model.

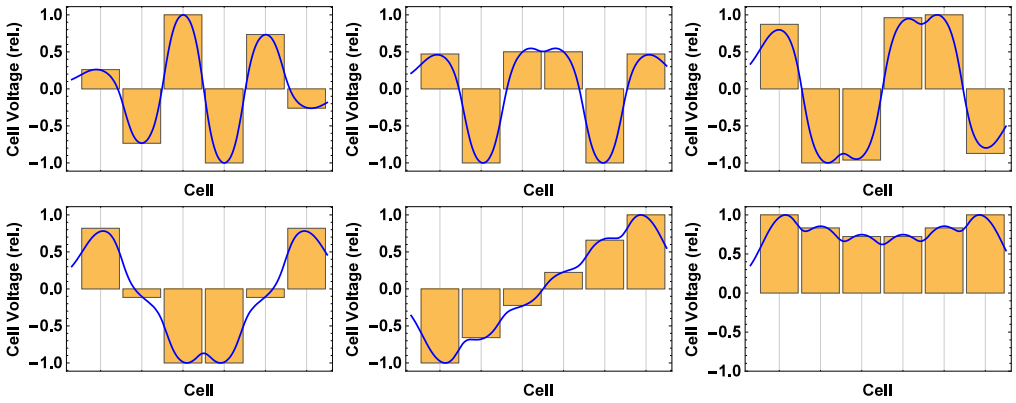

Figure 5.27: Comparison between normalized eigenvectors (blue lines) and circuit model (histogram) for the 2nd monopole band in the ESS medium -β cavity.

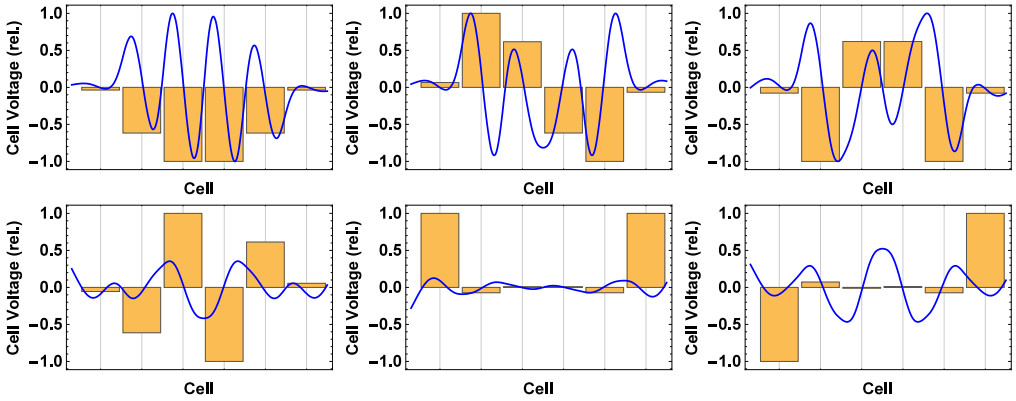

Figure 5.28: Comparison between normalized eigenvectors (blue lines) and circuit model (histogram) for the 3rd monopole band in the ESS medium-β cavity.

Mode	f_{HFSS} (MHz)	f_{CM} (MHz)	$\lvert f_{HFSS} - f_{CM} \rvert$ (MHz)
1	1515.67	1515.66	0.01
2	1517.22	1517.17	0.05
3	1524.37	1524.43	0.05
4	1534.25	1534.49	0.24
5	1544.87	1545.18	0.31
6	1553.29	1553.39	0.11

Table 5.17: Comparisons of mode frequencies from HFSS and the circuit model for the 2nd band of the ESS medium-β cavity.

Mode	f_{HFSS} (MHz)	f_{CM} (MHz)	$\lvert f_{HFSS} - f_{CM} \rvert$ (MHz)
1	1726.87	1724.33	2.53
2	1727.74	1726.60	1.13
3	1728.60	1732.17	3.57
4	1735.72	1739.26	3.54
5	1743.83	1745.73	1.89
6	1749.57	1750.06	0.49

Table 5.18: Comparisons of mode frequencies from HFSS and the circuit model for the 3$^{\text{rd}}$ band of the ESS medium-β cavity.

When the circuit model has been used the only parameter which has been allowed to vary is the cell resonant frequency. This does however mean that there is only one variable with which to fix the capacitive and inductive contributions to the error in the model. Consequently a statistical approach to filling the 2D space is taken using the purely capacitive and inductive error cases to constrain the parameters.

Implication of Random Errors on Mode Frequencies

To use the circuit model effectively to predict the mode frequency error a measurement of how the individual cell frequencies vary as a function of the geometric errors is required. This was achieved by using randomly generating uniformly distributed errors on all of the cell parameters, and calculating frequencies of each mode of interest using Superfish. To achieve a sample which is statistically significant this was done 500 times for errors from 100-1,000 μm in steps of 100 μm. An example histogram of the results and a plot of the variation of the standard deviation with the magnitude of the errors applied are shown in figure 5.29.

The behaviour of the cell frequencies with errors is Gaussian as would be expected for a case where random errors applied with the width increasing linearly with the magnitude of the applied errors. The fits extracted to the histograms

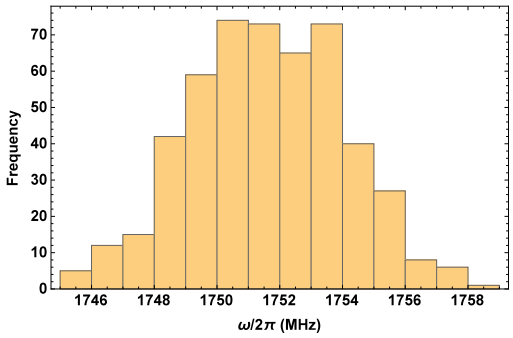

(a) Histogram of frequency errors to all seven cell parameters for the 3rd mode due to uniform errors of $\sigma = 300$ μm.

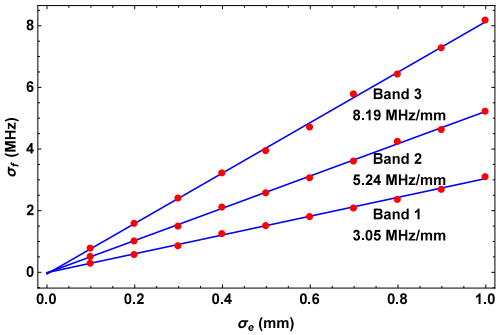

(b) Variation of standard deviation of HOM frequency error spread with magnitude of the random errors applied.

Figure 5.29: Frequency spread of single cell modes as a function of the magnitude of applied errors, σ_e.

can then be used to generate a random frequency distribution that can be used in the circuit model to look at the behaviour of the full structure modes.

Full Structure Frequency Sensitivity

To predict the possible spread in mode frequencies due to manufacturing errors the circuit model is used. This is done using the circuit model described in section 4.3 with the errors in the capacitance and inductance taken from the errors found in section 5.6.2.

Using the information found from the single cell studies, errors were randomly generated in the inductance and capacitance of each cell. These are then fed into the circuit model, the resulting eigenvalues are found and the process is repeated 10,000 times for each various magnitudes of geometric error. The resulting average frequencies are plotted in figure 5.30.

It can be seen in figure 5.30 there is a tendency for the modes furthest away from a phase advance of $\pi/2$ to shift further away from the $\pi/2$ frequency. This is a well known phenomena in cavity design [122] and is the reason that $\pi/2$ struc-

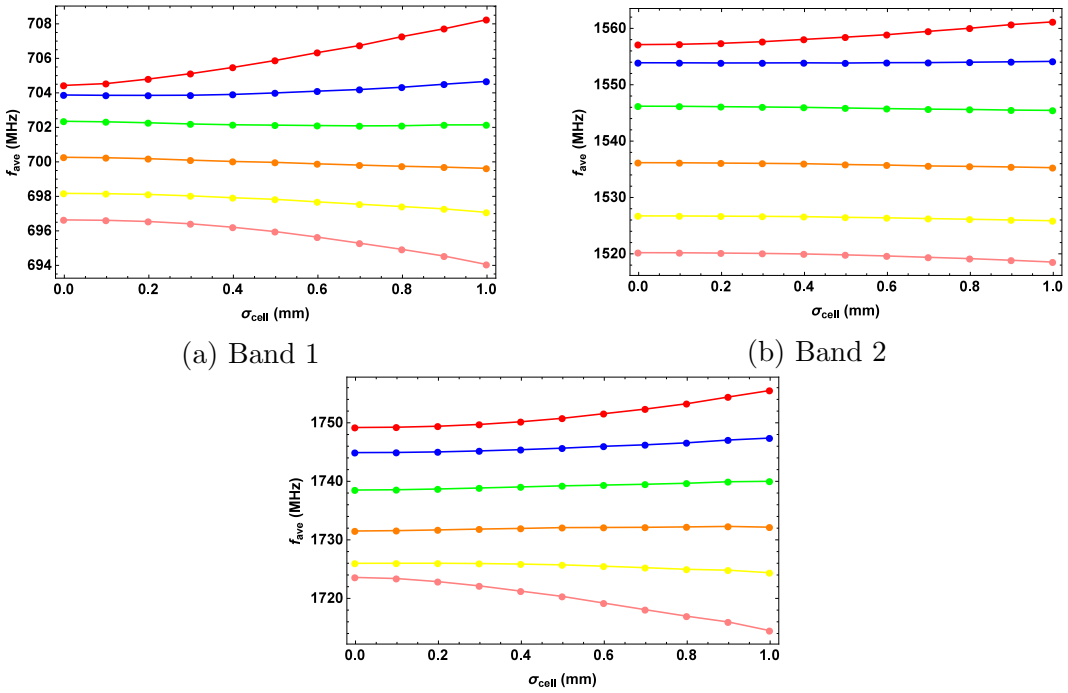

(a) Band 1

(b) Band 2

(c) Band 3

Figure 5.30: Application of circuit model to predict the average mode frequencies in the first three bands of the ESS medium-β cavity.

tures are used in accelerators which require reduced sensitivity to manufacturing errors.

Further, this also highlights an additional feature which is that in a high bandwidth HOMs that the π/N and π modes are most sensitive. As these are likely to be the modes closest to harmonics of the bunch frequency if a cavity is designed to avoid them it is of paramount importance to consider.

The mean frequency only reveals part of the information about the frequency variation. Most of the important information comes from the predicted spread in the mode frequencies and to this end the fraction of cavities with a mode within 5 MHz of the nearest machine harmonic in the third band have been plotted in figure 5.31. It can be seen that for small errors there are no cavities found within 5 MHz of the 5^{th} harmonic of the bunch frequency. However, for errors in the

region of 400 μm there is the potential to shift the HOM frequency to an harmonic of the bunch frequency. ESS has set a tolerance of $\pm$300 μm on deviations from the design this study indicates that these HOMs are unlikely to be resonantly driven.

Another important feature of that can be investigated with the circuit model is the relative sensitivity of the $5\pi/6$ mode to errors in a particular cell of the structure. To investigate this, errors in the range of $\pm$10 MHz have been applied to each cell individually and the corresponding relative shifts in cavity mode frequencies are shown in figure 5.32.

It is clear that the $\pi/6$ mode in the 3$^{\text{rd}}$ band is more sensitive to errors in the central cells. This is in agreement with what can be observed by plotting the Slater parameter (shown in figure 5.33) which clearly show a higher sensitivity in the central cells compared to the others. This also means that three dumbbells are responsible for the bulk of the frequency shift which could occur in this mode.

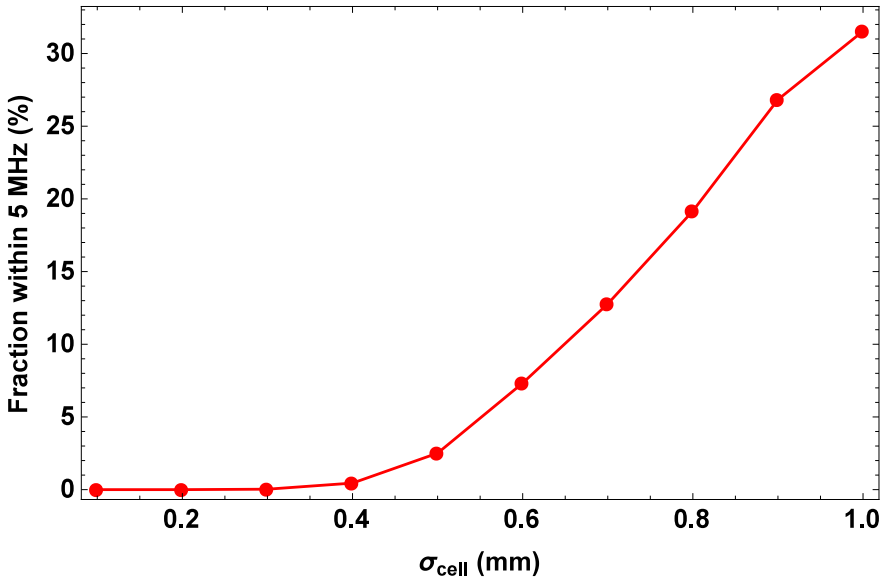

Figure 5.31: Fraction of cavities predicted to be within 5 MHz of the 5$^{\text{th}}$ machine harmonic in the 3$^{\text{rd}}$ band of the ESS medium-β cavity by the circuit model.

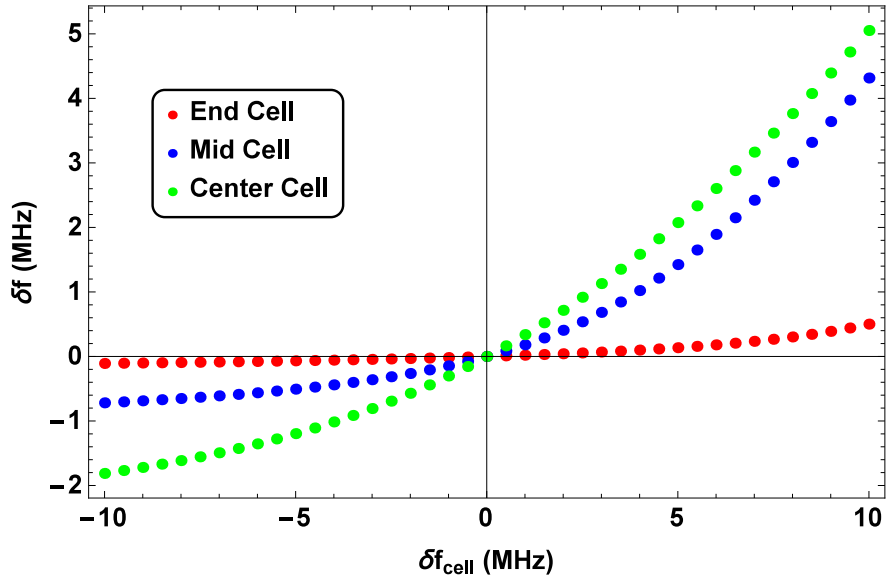

Figure 5.32: Relative sensitivity of the $\pi/6$ mode in the 3$^{\text{rd}}$ monopole band to errors in each cell. Only three cells are shown as the other three are equivalent due to the symmetry of the problem.

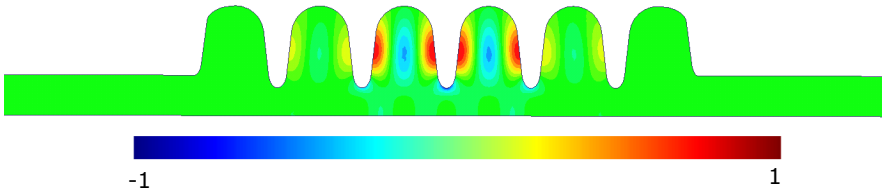

Figure 5.33: Normalised Slater parameter (equation 5.21) for the $\pi/6$ mode in the 3$^{\text{rd}}$ band of the ESS medium-β cavity.

5.7 Redesign of the ESS High-β Cavity

It has been discussed previously that when prototypes of the current ESS designs have been manufactured that although they have met the ESS requirements for the accelerating mode [36], they have failed to meet the specification that HOMs below cut-off should be 5 MHz away from harmonics of the bunch frequency. As such the cavities would not be accepted by ESS and this suggests that the 11 MHz separation from the nearest harmonic may not be enough to ensure the cavities pass the requirement upon construction.

Therefore if it is possible to increase the frequency of the first two modes in the 2nd monopole band it would be beneficial. However, for this to viable the properties of the accelerating mode must not change significantly and the final cavity must be plug compatible with the current design. In figure 5.34 it is clear that the modes are particularly sensitive in the end cells and as such only these need to be modified to change the HOM frequency.

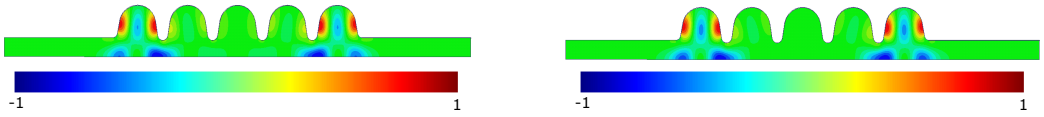

(a) 1419.22 MHz mode (b) 1419.82 MHz mode

Figure 5.34: Normalised Slaters parameter (equation 5.21) for the first two modes in the 2nd monopole band of the ESS high-β cavity.

A key feature for obtaining a field flat cavity is to tune the end-cells such that the coupling to the beam pipe is twice that of the inter-cell coupling. This is achieved by tuning the frequency of the end-cell with the beam pipe included and the process used in this redesign is given in the following sections.

5.7.1 End Cell Sensitivity

It has been identified that the end-cells must be changed to modify the frequency of the two HOMs closest to harmonics of the bunch frequency. To this end the original geometry has been extracted from CAD files [110] and the cavity was re-simulated to check that the extracted geometry was consistent with the expected parameters. The properties of the accelerating mode found using this method are detailed in table 5.19 and it can be seen that they are in reasonable agreement with the values expected from published work [36, 115]. In addition to this the mid-cell of the cavity was simulated and it was found to have a π mode frequency of 704.42 MHz and bandwidth of 1.2% as specified. This means it is likely that

the small error in frequency and field flatness are a result of the end-cells not being exactly the same as the design, however as these are what will be modified in the following analysis it is of little concern.

Parameter	Value	Unit
Freq.	704.40	MHz
Maximum R/Q	477	Ω
B_{pk}/E_a	4.31	mT/MV/m
E_{pk}/E_a	2.25	-
Geometric Factor	241.8	Ω
Field Flatness	99	%

Table 5.19: Properties of the accelerating mode in the reconstructed cavity.

As the design of the cryomodule and RF system is almost completed any changes must be plug compatible with the current design to avoid making wholesale changes. Therefore the mid-cell geometry was fixed as well as the cell length, radius and beam pipe radius. To investigate the relevant sensitivities of the end-cell to changes the cell without the beam pipe was simulated and varied the parameters over several mm. The relative sensitivity of the first two band was extracted and is given in table 5.20

Parameter	Band 1	Band 2	Units
A	-1.15	-4.39	MHz/mm
B	0.38	0.90	MHz/mm
a	-0.43	2.61	MHz/mm
b	0.09	-0.44	MHz/mm

Table 5.20: Sensitivity of the end cell to geometric changes.

Form the data it is clear that a and A are the most sensitive parameters for both the accelerating mode and the HOM. It is also important to note that the behaviour of the frequencies to changes in a as in opposite directions to changes in A which would enable the HOM to be pushed further away from the harmonic of the bunch frequency as the accelerating mode is brought back onto frequency.

It is therefore the parameters a and A which have been varied to create a final design.

5.7.2 Final Cavity Design

Compared to the original design by CEA Saclay the geometry has been changed by reducing the equator ellipse eccentricity A by 1.7 mm and increasing the iris ellipse eccentricity a by 3.0 mm. This results in a cavity which is very similar in almost all ways but with a significantly improved HOM spectrum. The properties of the accelerating mode found when the cavity is simulated in CST MWS and HFSS are given in table 5.21.

Parameter	HFSS	CST MWS	Unit
Freq.	704.42	704.42	MHz
Maximum R/Q	475.53	474.8	Ω
B_{pk}/E_a	4.33	4.36	mT/MV/m
E_{pk}/E_a	2.26	2.27	-
Geometric Factor	277.21	-	Ω
Field Flatness	99.5	99.4	%

Table 5.21: Properties of the accelerating mode with the redesigned end cells.

Parameter	Orig. Design	New Design	Unit	Difference (%)
Freq.	704.40	704.42	MHz	N/A
Maximum R/Q	477	475.53	Ω	-0.3
B_{pk}/E_a	4.31	4.33	mT/MV/m	+0.6
E_{pk}/E_a	2.25	2.26	-	+0.4
Geometric Factor	241.8	277.21	Ω	+15
Field Flatness	99	99.5	%	+0.5

Table 5.22: Comparison of main cavity properties in from HFSS.

There is a small decrease in the R/Q by 0.3% whilst the peak surface fields increase by 0.6% and 0.4% for the magnetic and electric fields respectively. These changes are small and unlikely to have any noticeable effect on the performance of the cavity. In addition there is an increase in the geometric factor by 15%

which will cause the Q_0 to raise by an equal amount improving the performance of the cavity. Most important by far in this analysis is the impact on the HOM spectrum which has been simulated with both HFSS and CST with the results given in tables 5.23 and 5.24.

In the tables it is clear that the results from both codes are consistent with each other with differences expected due to the different numerical methods and meshes used. The most important feature however is that the first two modes in the 2^{nd} monopole band are moved to 1426.79 MHz and 1430.25 MHz (From HFSS) which is an increase in the frequency separation from 4^{th} machine harmonic by 7.57 MHz which is an increase of 70%. This change is significant as the margin of separation from the ESS limit of 5 MHz to the closest machine harmonic has increased by 140% from 5.38 MHz to 12.95 MHz.

HFSS Freq. (MHz)	Max R/Q (Ω)	$\lvert f_n - f_{ML} \rvert$ (MHz)
693.19	0.11	11.23
696.28	0.28	8.14
700.12	3.31	4.30
703.22	76.73	1.20
704.42	475.53	0
1426.79	0.53	17.95
1430.25	1.97	21.41
1437.12	3.85	28.28
1447.00	15.88	38.16
1458.22	69.01	49.38
1481.17	3.11	72.33
1492.53	10.91	83.69
1506.03	3.43	97.19
1518.68	1.10	109.45
1528.06	0.18	119.22

Table 5.23: Properties of the accelerating mode with the redesigned end cells in HFSS.

Freq. (MHz)	Max R/Q (Ω)	$\lvert f_n - f_{ML} \rvert$ (MHz)
693.18	0.12	11.24
696.28	0.28	8.14
700.12	3.32	4.30
703.22	76.44	1.20
704.42	474.8	0
1426.75	0.54	17.95
1430.22	2.08	21.38
1437.08	3.94	28.24
1446.97	16.45	38.14
1458.12	67.97	49.38
1481.18	3.69	72.29
1492.53	10.83	83.69
1506.03	3.33	97.19
1518.69	0.87	109.46
1528.07	0.10	119.23

Table 5.24: Properties of the accelerating mode with the redesigned end cells in CST.

5.7.3 Fundamental Power Coupler

In both the high-β and medium-β cavities ESS has opted to use the same design for the FPC but with different penetration depth. To check if this is possible with this redesigned cavity the system is simulated with the original FPC present at exactly the same distance from the cavity. The penetration depth was then varied to see how the Q_{ex} changed as a function of the penetration depth, which is take as the distance from the base of the antenna to the beam axis. The behaviour of the Q_{ex} is shown in figure 5.35 .

To match the specified Q_{ex} of 7.6×10^5 a penetration depth of 62.56 mm is required which is 1.85 mm lower than in the original design.

My redesign of the cavity entailed shifting the HOM frequencies away from the 4^{th} harmonic of the bunch frequency. This has been achieved through only changing the end-cell geometry and it results in an accelerating mode with almost identical properties to the ESS baseline design with a small reduction in R/Q and

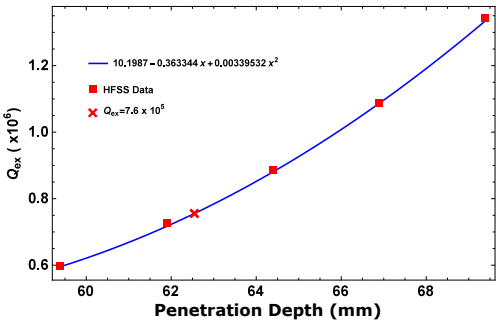

(a) Q_{ex} against coupler penetration depth.

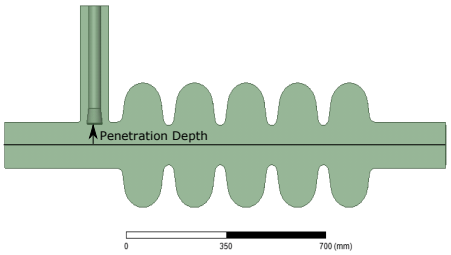

(b) Definition of coupler penetration depth

Figure 5.35: Variation in Q_{ex} with the penetration depth of the coupler.

small increases in the peak surface fields. As the changes in my design are small the FPC can be matched without changing its shape or position.

5.8 Cavity Mode Analysis Summary

The modal structure of each of the SCRF cavity types in the ESS accelerator have been analysed using the finite element code ANSYS HFSS v16.2. The first 100 modes in the spoke cavities have been analysed in detail and the properties of both longitudinal and transverse modes have been given.

For the elliptical cavities the first 60 monopole and transverse modes have been analysed. I found the amplitude of the loss/kick factors for all modes are smaller compared to the usual higher frequency cavities commonly used as expected from frequency scaling arguments. This is an indication that the impact on the beam may be small. However I noted that a two modes in the high-β cavity and one in the medium-β cavity lie close to harmonics of the bunch frequency. These modes have the potential to shift in frequency, due to manufacturing errors, to lie on a machine harmonic and hence be resonantly driven by the beam.

To assess the likelihood of this, I performed a detailed analysis using Superfish

in conjunction with a circuit model, focusing on the medium-β cavity. It was found that the mode of interest at 1749 MHz was particularly sensitive to errors in the parameters A and L. In both of these parameters the frequency was much more sensitive than the accelerating mode by a factor of 5.6 and 3.3 respectively, with the L causing the frequency to shift in the opposite direction to the accelerating mode. The sensitivity to random errors was then analysed and fed into the circuit model to predict the possible frequency spread, which showed that random errors of above 400 μm could shift the HOM onto the nearest machine harmonic. The use of the circuit model allowed for calculations of the potential frequency shifts to be performed quickly compared to full cavity simulations of the large parameter space present. This speed comes at a cost due to the truncation of the problem to fewer degrees of freedom. As a result the ability to accurately determine the effects of a specific error in a cavity is lost but the ability to predict the potential spread in frequencies is still present. The methodology adopted has the potential to be applied to the linac in machines such as X-FEL and the ILC will facilitate the frequency and field flatness of the accelerating mode and HOMs to be rapidly analysed in detail prior to cavity production and potential pitfalls spotted.

Further the relative sensitivity of the $\pi/6$ mode to errors in individual cell was investigated and it was found that the middle cells are particularly sensitive. This increased sensitivity in the middle cells is in agreement with work carried out at CEA Saclay, Gif-Sur-Yvette, France by E. Cenni [113] where individual dumbbells are tested and the best of them are selected for the centre cells.

In addition it has been shown that the separation of the two closest modes to the 4^{th} harmonic of the bunch frequency in the high-β cavity can be increased through modifying the end-cell geometry. My new design entails varying the parameters A and a, which results in the mode separation increasing by 7.57 MHz

with only a slight reduction in R/Q and a slight increase in the peak surface fields. However these changes have increased the geometric factor by 15% which results in an increase in the Q_0 of the cavity by the same amount. This is a result of a reduction in the surface fields integrated over the cavity walls and will result in improved cavity performance compared to the original design. As this cavity is at a frequency which is being increasingly used in high intensity proton linacs the design could easily be used in other machines which require a 704.42 MHz cavity.

Although the results of this chapter apply directly to the ESS linac and its cavities the methodology used to analyse the impact of manufacturing errors can readily be applied to other cavities. This include the frequency sensitivity simulations and the extension to the circuit model to looking at the distributions of expected frequencies and also at the particular sensitivity of individual cells.

In the next chapter the wakefield in low-β cavities will be compared to that which is known analytically for $\beta = 1$ structure to show that no additional modifications are required. In addition a comparison between the wakefield predicted by the modal summation method and finite difference simulations are given at various β's.

Chapter 6

The Wakefield in Low Beta Cavities

When a charged particle traverses an RF cavity it inevitably excites field inside the cavity known as a wakefield. The theory behind beam-excited wakefields is well understood for the case where the beam is ultra-relativistic ($v \approx c$) and this has been discussed at length in chapter 3.

In the case of $v < c$ fields exist in front of the exciting charge without breaking the principle of causality. This opens up the possibility that a wakefield may exist ahead of the drive charge however, testing if this is true is non-trivial. It has been shown by Bane [116] that once the exciting charge has left the cavity the theory for $v = c$ and $v < c$ are consistent once changes in the modal loss factors due to the transit-time factor are accounted for (cf. equation 2.35).

In low-β structure the fact that the wakefield behaves as it does in the $v = c$ case is often assumed and there is little recorded data which gives evidence for this assumption. It is possible that when two bunches are within the same cavity that the wakefield is in a transient state between the $v = c$ behaviour which is assumed

and the space charge fields from the exciting bunches. Therefore a detailed study of the phenomena present in low-β cavities is required to gain confidence in later simulations which require this to be the case. The final analysis will allow the practical limits of this assumption to be tested in general which has application to proton linacs, electron guns and low energy electron cavities. A detailed analysis of the physics in the low velocity case has not been detailed in literature therefore this analysis will provide insight into the behaviour of the wakefield in low-β structure which is currently undocumented. The analysis will be applied directly to the ESS cavities as a specific example giving data from $\beta = 0.5$ to $\beta = 0.86$. This phenomena could have a significant effect on machines which have a high bunch charge with small bunch separations where multiple bunches within a pulse are contained within the same cavity at $v < c$. In addition, in an electron gun—where $\beta < 1$—the effects of the short range wakefield on trailing bunches has the potential to dilute the emittance of the beam and this will impact the overall operation of a state of the art light source or linear collider.

In this chapter the $v = c$ wakefield for a pillbox cavity will be analysed using the analytical solution derived by Weiland and Zotter [123], and simulations performed in CST MWS. The theory is then extended to the of a $v < c$ bunch passing through the same pillbox cavity and compared in the long range to show consistency with Bane's analytic result once the exciting bunch has left the cavity. Finally, the short range wakefield is investigated using CST MWS which is then compared to the analytic results to highlight features which may differ due to fields ahead of the drive bunch.

6.1 Wakefield in a Pillbox for $v = c$

The longitudinal wakefield for $v = c$ has been shown to be

$$W_z(s) = \sum_n^{\infty} k_{\parallel,n} \cos\left(\frac{\omega_n s}{c}\right) \begin{cases} 0 & s < 0 \\ 1 & s = 0 \\ 2 & s > 0 \end{cases} \tag{6.1}$$

for a arbitrarily shaped closed cavity, where $k_{\parallel,n}$ is the modal loss factor. For pillbox cavity of length g and radius R the modal loss factor of the monopole modes are given by

$$k_{n,p} = \frac{1}{\pi\epsilon_0 g} \frac{1 - (-1)^p \cos\left(\omega_{n,p}\frac{g}{c}\right)}{j_n^2 J_1^2\left(j_n\right)} \tag{6.2}$$

where j_n is the n$^{\text{th}}$ zero of the first Bessel function of the 1$^{\text{st}}$ kind, J_1 is the 2$^{\text{nd}}$ Bessel function of the first kind and $\omega_{n,p}$ is the angular frequency of the mode give by

$$\omega_{n,p} = c\sqrt{\left(\frac{j_n}{R}\right)^2 + \left(\frac{\pi p}{g}\right)^2}.$$

The wakefield in this form is completely analytic based purely on the Condon method.

As a result there should be complete agreement between this and simulations for a $v = c$ bunch passing through a cavity. However, most codes require a bunch of finite length to truncate the frequency spectrum excited by the bunch, therefore the wakefield for a Gaussian bunch of known length is required. The

wakefield from an arbitrary bunch distribution can be written as

$$W_z(s) = -\sum_{\mu} j_\lambda\left(\omega_\mu, s\right) k_\mu e^{-i\omega_\mu s/c} \tag{6.3}$$

where ω_μ is the angular frequency, μ is a valid n,p combination and j_λ is given by

$$j_\lambda(\omega, s) = \int_{-\infty}^{s/c} j_\lambda(t) e^{i\omega t}\, dt. \tag{6.4}$$

$j_\lambda(t)$ is the shape of the exciting charge in the time domain. Using this formula the wakefield for an arbitrary bunch in any closed cavity can be calculated. This is based on the Green's function method where the point charge wakefield acts as the Green's function. This calculation has been performed for a cavity of $R = 50$ mm and $g = 100$ mm. A comparison between CST MWS with a $\sigma = 25$ mm bunch and the analytic model with 400 modes is shown in figure 6.1.

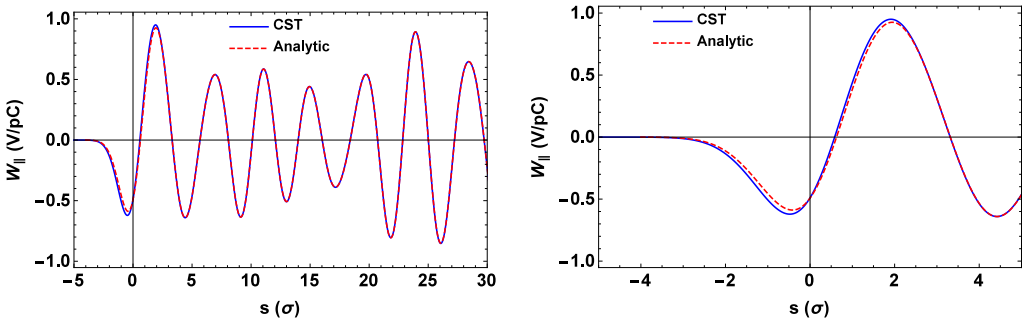

(a) Long Range Wakefield (b) Short Range Wakefield

Figure 6.1: A comparison between the analytic wakefield and CST MWS for a pill box cavity of radius 50 mm and length 100 mm with an exciting Gaussian charge of σ =25 mm

There is also an expected error as the solver in CST MWS requires that the bunch enters and leaves via a port, this meant that beam pipes have to be added. By keeping the beam pipes very small (r=0.5 mm) in comparison to the radius of the cavity a minimal impact on the results can be obtained.

In figure 6.1 it is clear that in the long range the wakefield from CST is in excellent agreement with the wakefield from the analytic model. However, in the short range the agreement is poorer as a result of the errors due to high frequency components which have not been included due to both truncation of the sum in the analytic model and limited meshing in CST MWS. These issues have been documented by T. Weiland and B. Zotter [123] where it was shown that increasing the mesh density and number of modes results in the solutions tending towards agreement at an intermediate value.

This is shown in figure 6.2 where the short range wakefield is plotted for an increasing number of modes and mesh densities. As the number of modes and mesh are increased, the difference between the wakefield curves from analytic and CST calculations decreases, as the curves are pulled towards each other. Though the difference does not vanish completely, as the wakes calculated even with 4000 modes and 10 million mesh cells showed maximum difference of 0.5% and 0.1% in short and long range respectively.

This can also be illustrated by plotting the contribution to the final solution from each of the component modes in the modal summation. The first nine of which are shown in figure 6.3 and it is clear that for the higher frequency modes there is a significant contribution within the bunch. However, in the long range the contributions are quite small compared to the lower frequency modes.

6.2 Long Range Wakefield in a Pillbox for $v < c$

When the velocity of the bunch is less than the speed of light the assumption that field may not exist in front of the drive charge is no longer valid and the theory is not necessarily correct whilst the exciting charge is inside the cavity. However, it has been shown by Bane [116] that once the exciting charge has left

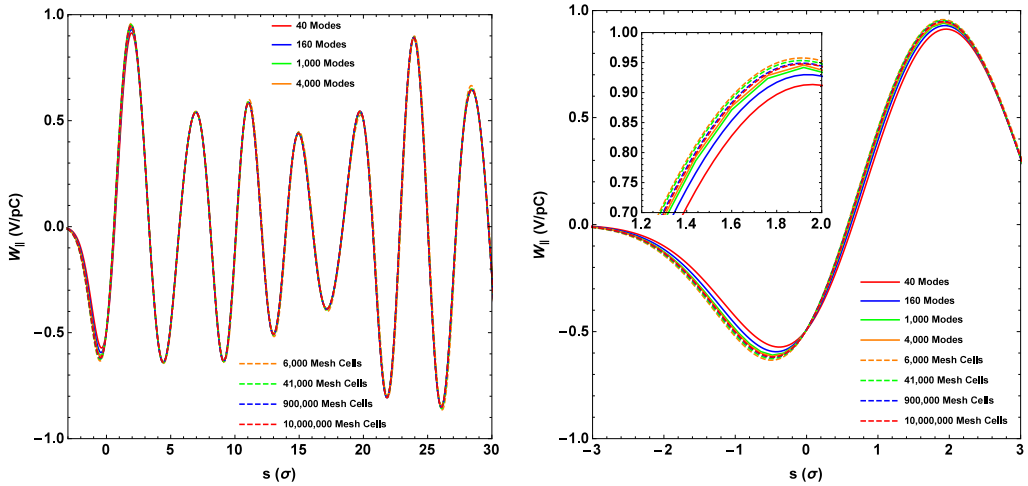

(a) Long Range Wakefield (b) Short Range Wakefield

Figure 6.2: A comparison between the short range wakefield from CST MWS and the modal summation method for varying mesh densities and numbers of modes. The cavity is a pill box cavity of radius 50 mm and length 100 mm with an exciting Gaussian charge of σ =25 mm.

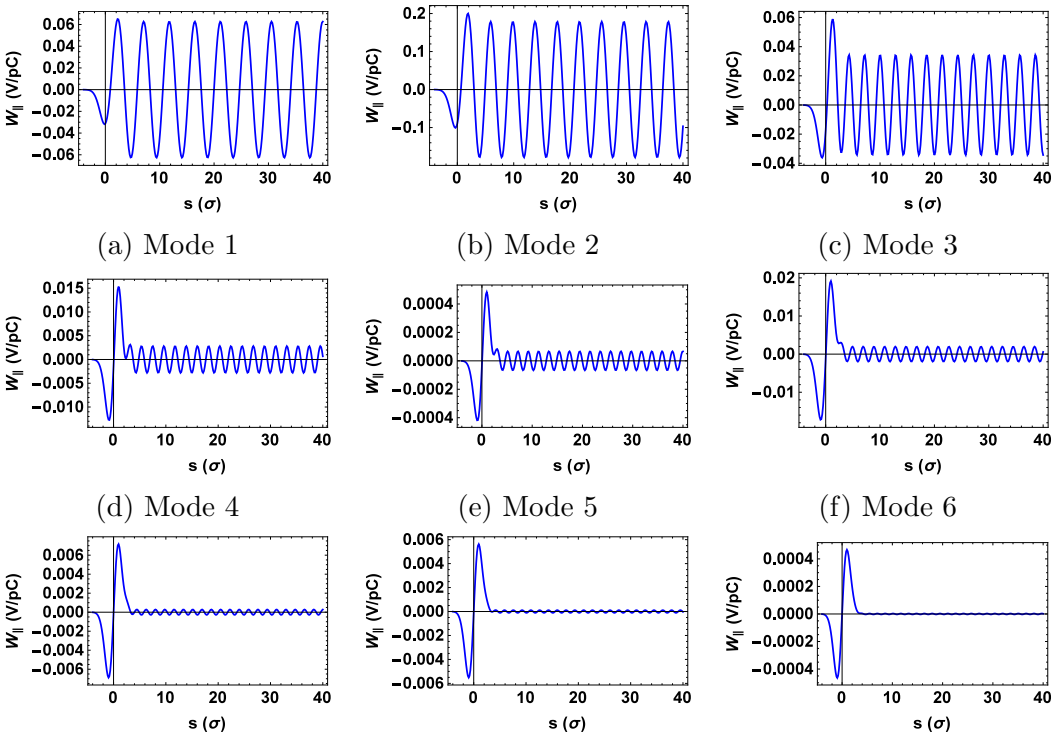

(a) Mode 1 (b) Mode 2 (c) Mode 3

(d) Mode 4 (e) Mode 5 (f) Mode 6

(g) Mode 7 (h) Mode 8 (i) Mode 9

Figure 6.3: Modal components of the wakefield in figure 6.1.

the cavity the wakefield becomes identical to the solution expected for $v = c$ with some modifications to the loss factors as a result of changing transit time factors. The loss factor for a pillbox cavity of arbitrary radius and length, for bunches of $v < c$ is given by

$$k_n(n,p) = \frac{2\left(\frac{j_n B}{R(A^2+B^2)}\right)^2 [1-(-1)^p \cos(Bg)]}{\pi\epsilon_0 \left(\frac{\omega}{c}\right)^2 g R^2 J_1(j_n)}, \tag{6.5}$$

where $A = \frac{p\pi}{g}$ and $B = \frac{\omega}{\beta c}$. The derivation of equation 6.5 is given in appendix D. By applying equation 6.3 for a known bunch with the loss factors given by equation 6.5 the wakefield should be consistent with the theory once the bunch has left the cavity.

Figure 6.4 shows that the agreement in the long range wakefield is very good regardless of the velocity of the exciting bunch. This in itself shows that the wakefield at the arrival of subsequent bunches in the ESS accelerator should be given by the traditional theory.

In the short range, $s < 5\sigma$ there is a significant deviation from the model. In this case it is clearly not viable to assume the theory holds. In the next section the phenomena in the short range will be investigated in more detail.

6.3 Short Range Wakefield in $v < c$ Cavities

In the case of $\beta = 1$ the wakefield decelerates the charge which induces the wakefield and hence has the opposite sign to the charge. However, in the case of $\beta < 1$ the wakefield clearly has the same sign as the charge (positive in this case), this is an indication that the field is not a wakefield per-say but a static field associated with the exciting bunch, as the wakefield itself must be decelerating to preserve energy conservation (c.f. section 3.1.2).

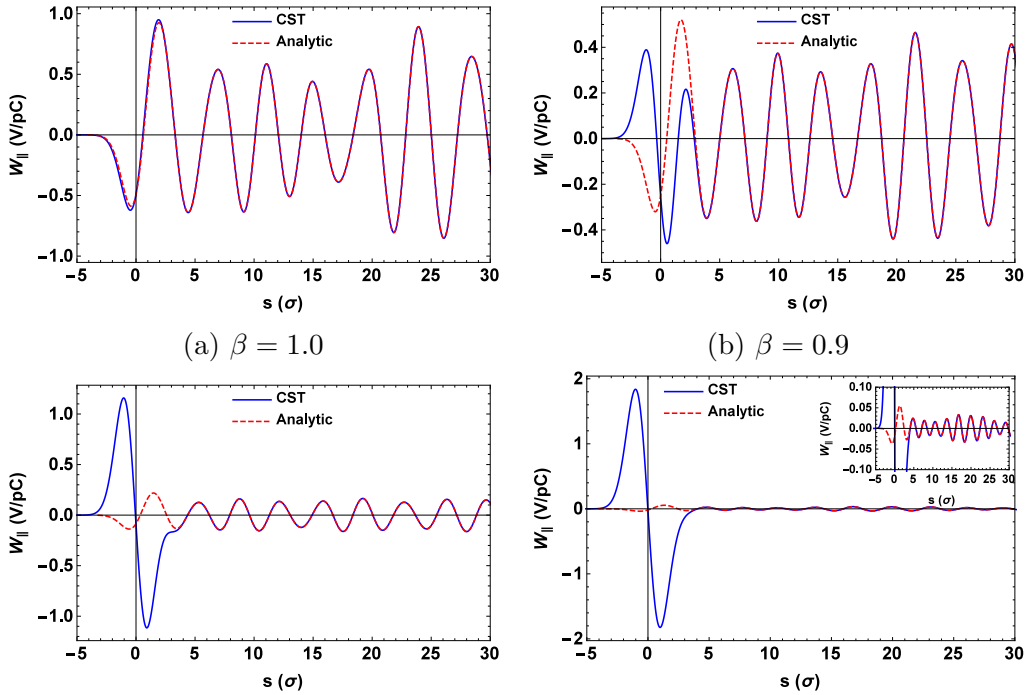

(a) $\beta = 1.0$ (b) $\beta = 0.9$

(c) $\beta = 0.8$ (d) $\beta = 0.7$

Figure 6.4: Comparison of the long range wakefield for a pillbox cavity simulated in CST MWS with the analytic model for beams at various velocities.

To test this hypothesis the wakefield can be calculated at various offsets, if as suspected the field is static its amplitude should fall off in a similar way to Coulomb's law $|\vec{E}| \propto r^{-2}$. To achieve this the magnitude of the cavity fields must be changed consistent with the radial behaviour. This is tested using a $v = c$ bunch and is shown in figure 6.5.

In figure 6.5 the agreement between the long range wakefields is again good which is an indication that the analytic model is behaving correctly when the radial variation is included. The agreement in short range is good at smaller offsets, but at larger offsets the CST wakefield begins to lag behind the analytic calculations. This appears temporal delay and could be a result of causality with 30 mm offset equivalent to 10 ns off delay. The same simulations were performed with a $v < c$ bunch and the resulting data is shown in figure 6.6 and 6.7 for

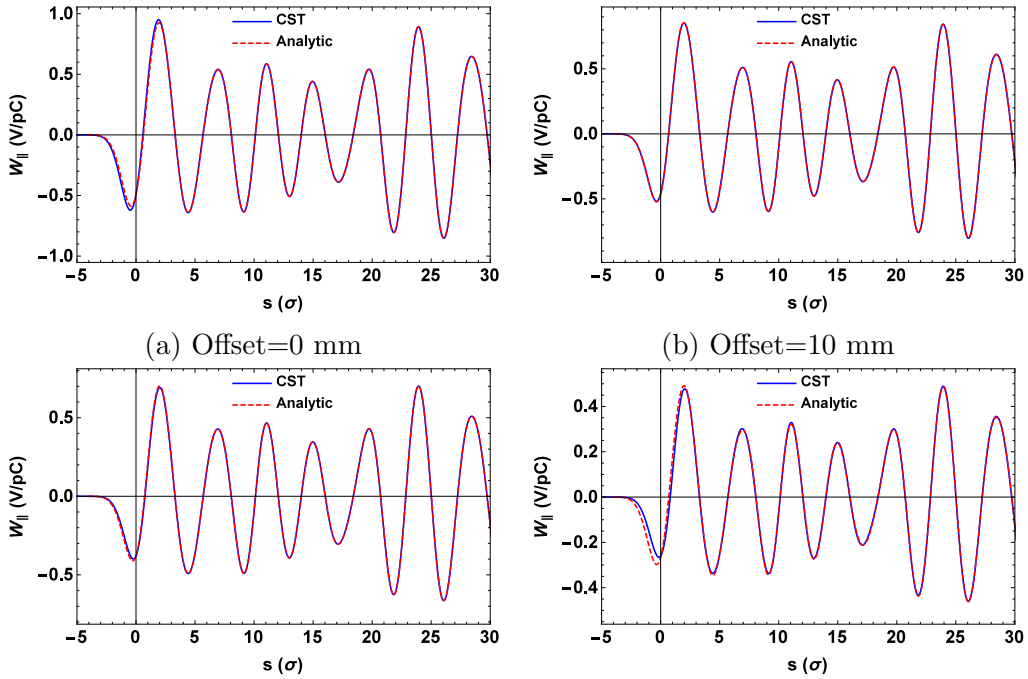

(a) Offset=0 mm

(b) Offset=10 mm

(c) Offset=20 mm

(d) Offset=30 mm

Figure 6.5: Variation of the wakefield with offset compared to the analytic model including this behaviour at various offsets for $\beta = 1$.

different values of v.

In both cases there is good agreement between the long range wakefields from CST MWS and the analytic model. In the short range however the agreement on-axis is poor. When the wakefield is analysed off-axis however the agreement improves which suggests the dominant contributor to the difference is static fields from the exciting charge. Again though, at larger offsets there is a similar temporal delay as seen in the $v = c$ case.

This study gives a clear indication that the modal summation method is valid for $v < c$ wakefield like those that will be present at ESS. In addition it also highlighted the space charge like fields being dominant contributors in the short range wakefield and that causal effects are present off axis. These effects meant it was not possible to determine if there was a wakefield excited ahead of the

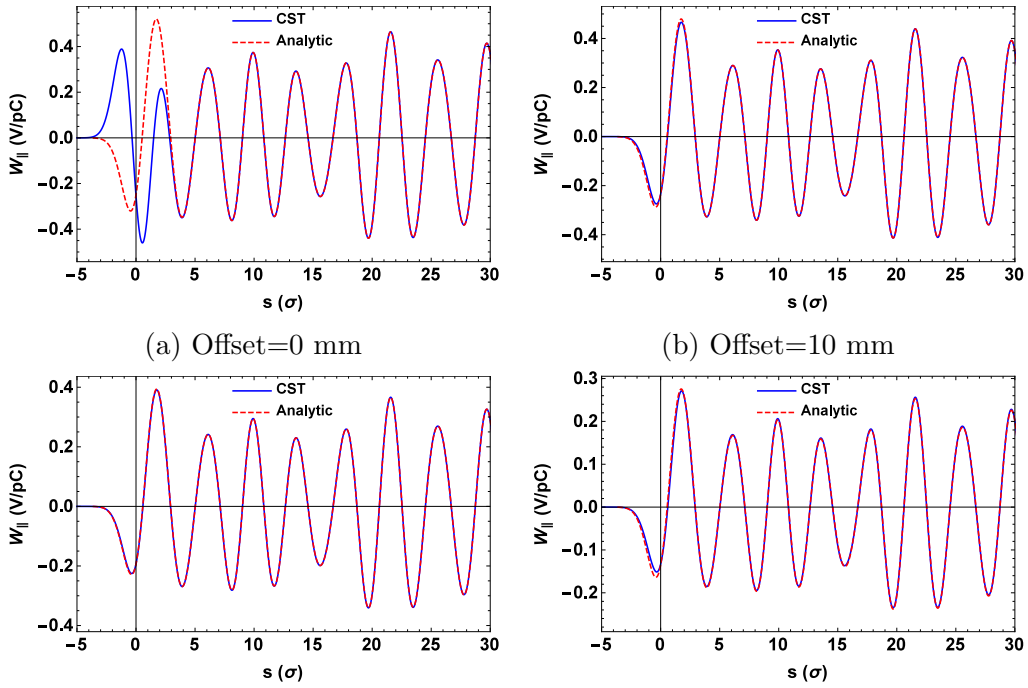

(a) Offset=0 mm

(b) Offset=10 mm

(c) Offset=20 mm

(d) Offset=30 mm

Figure 6.6: Variation of the wakefield with offset compared to the analytic model including this behaviour at various offsets for $\beta = 0.9$.

exciting charge.

In the next section the wakefield of the three types of cavity at ESS will be analysed using CST MWS and a comparison to the modal summation method will be made using loss factors extracted from HFSS simulations detailed in chapter 5.

6.4 The Wakefield in the ESS cavities

The bunch spacing at ESS is given by the reciprocal of the bunch frequency which is 2.84 ns or 0.86 m at $v = c$. Bunch separation shorter than the cavity length means that two bunches will be in a cavity simultaneously. Therefore accurate simulation of the wakefield should be performed which can show the magnitude of the wakefield at the bunch separation.

Each of the ESS cavities have been imported into CST from SAT files [110].

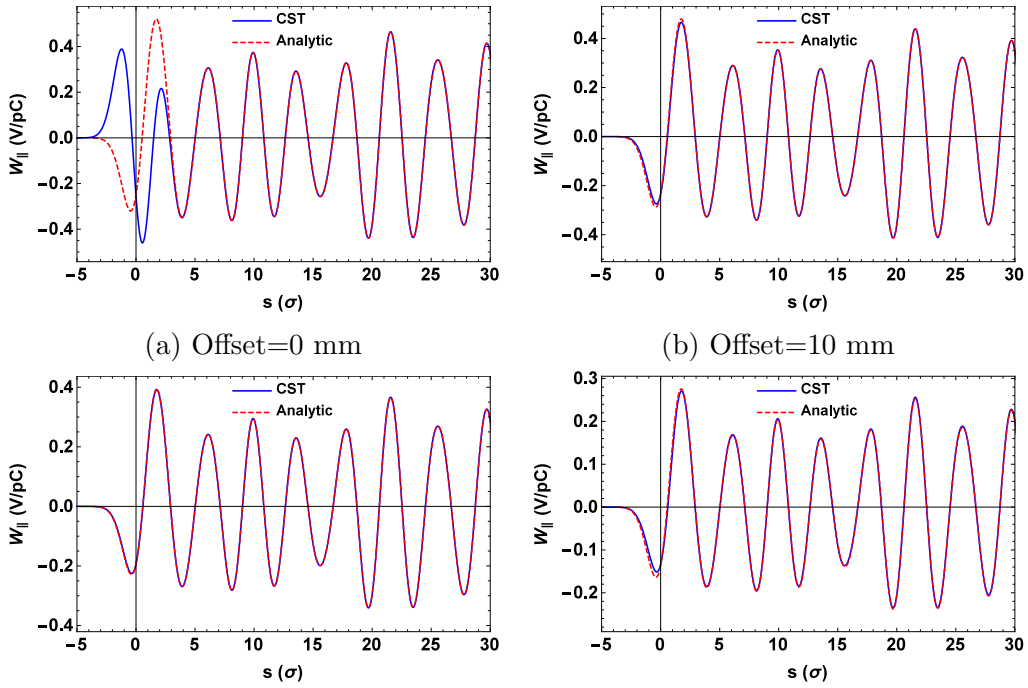

(a) Offset=0 mm

(b) Offset=10 mm

(c) Offset=20 mm

(d) Offset=30 mm

Figure 6.7: Variation of the wakefield with offset compared to the analytic model including this behaviour at various offsets for $\beta = 0.8$.

The input couplers on each cavity have been removed as the damping of the HOMs is strongly dependent on the behaviour beyond the antenna which is not considered here. EM symmetry planes are applied to reduce computational volume. The simulations are performed at the geometric beta of the cavities (0.5,0.67 and 0.86 respectively) with a bunch length of $\sigma = 25$ mm. This is much longer than the bunch length at ESS (3-12 mm at 5σ) and is used to truncate the problem to only modes which are below the beam pipe cut-off to prevent the problems becoming to large to efficiently solve. For a $\sigma = 1$ mm length bunch the frequency spectrum is $\sigma \approx 95$ GHz wide which would require many modes for the modal summation and also 100's μm level mesh which for such large cavities, therefore a longer bunch must be used. A 25 mm bunch has a frequency spectrum of $\sigma \approx 4$ GHz which is closer to the frequencies of the modes considered in

these cavities. The reason for this is that in the long range high frequency modes readily become out of phase with the wakefield which is dominated by the most strongly excited modes which are at lower frequencies. In addition, the $TE_{1,1}$ cut-off frequency for the beam pipes at ESS are 1.64 GHz in the elliptical cavities and 4.10 GHz in the spoke cavities and this means many modes above 4 GHz are propagating modes. These propagating modes are likely to couple between cavities and also have a strong possibility of being damped by the FPC and/or other normal conducting components.

The longitudinal wakefields extracted from CST are compared to the same calculated using modal sum method in figure 6.8.

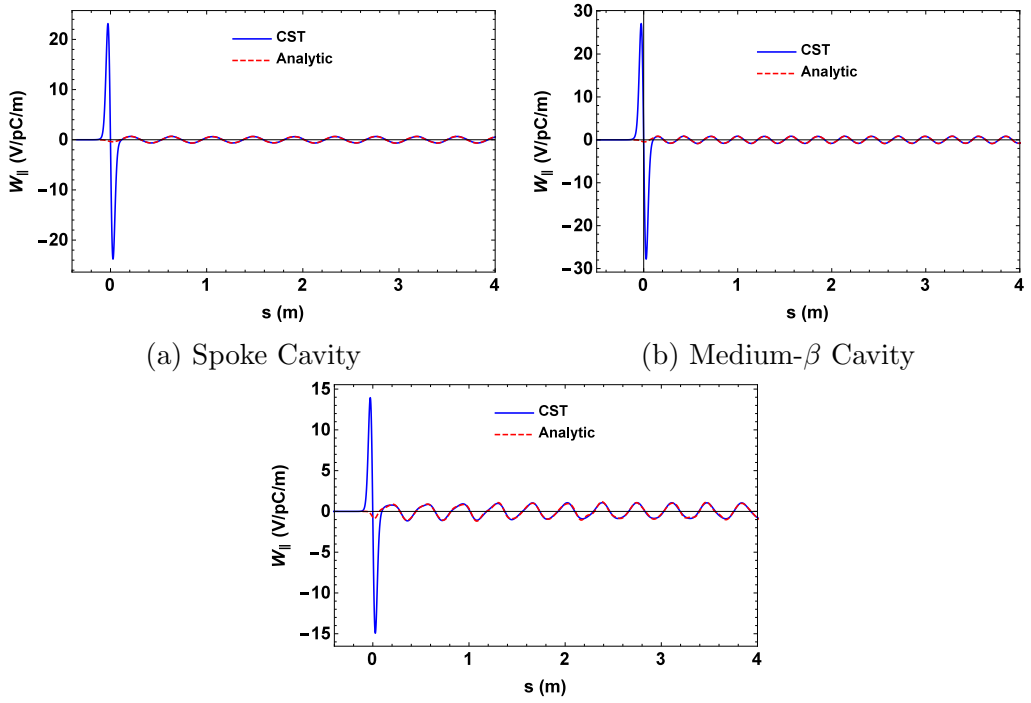

(a) Spoke Cavity

(b) Medium-β Cavity

(c) High-β Cavity

Figure 6.8: Longitudinal wakefield simulation performed using CST MWS wakefield solver for each of the ESS cavity types at their geometric β for a bunch length of $\sigma = 25$ mm.

The long range wake for all cavities are in good agreement with each other

for all cavities, with a slight disagreement in the amplitude of some of the peaks in the high-β cavity. For the short range wakefield there is the presence of the static field from the bunch and it is important that these do not extend to the bunch separation of s/β in the plots. In addition as the true bunch length is much smaller than that simulated the space charge effect will be further reduced. This means there will not be any significant contribution to the interaction with the trailing bunches from the static fields of the exciting charge.

6.5 Summary

In the area of wakefield analysis much of the early and current work has focussed on the case of an ultra-relativistic beam. This has a consequence that there is little literature with regards to the phenomena of the wakefield within structure which accelerate particles of $v \ll c$ such as the ever more common high intensity proton linac. Due to the increased presence of these machines a detailed understanding of the phenomena is required. In an attempt to do so this work has taken ideas developed for $v \approx c$ and extended them to the $v \ll c$ to test their validity in this alternate regime.

It has been shown that the numerical code CST MWS produces results consistent with the analytical description provided by T. Weiland and B. Zotter for $v = c$. This has been extended to include beams with $v < c$. It was found that there was good agreement between CST and the model in the long range wakefield, however in the short range the agreement was not particularly good and it was deduced that this was due to static space charge like fields. This has been corroborated by simulations of the off-axis wakefield. The study also highlighted that there is a causal time delay in the wakefield for test paths which lie off-axis.

Further the longitudinal wakefields for each of the ESS cavities obtained in

CST MWS at the geometric beta of the structure have been shown to be in agreement with the modal summation at the bunch spacing of the machine. These simulations suggest that the traditional modal summation is valid at the for beam velocities of $\beta > 0.5$ for bunch spacings of less than the cavity length. This therefore lends confidence to the use of the modal summation method in simulations of similar low energy machines such as proton linacs and electron guns.

This result validates the use of the modal representation of the wakefield in the drift-kick-drift codes used to analyse the effects of HOMs on many proton linacs [51, 52]. Further it also suggests the methodology may be applicable in regions where the bunch spacing is further reduced from value in the ESS cavities.

In the next chapter the impact of beam-excited mode of the beam quality at ESS is discussed in detail.

Chapter 7

Beam Dynamics Simulations of the ESS Linac

In this chapter the main focus will be on the impact of beam-excited HOMs on the beam dynamics of the ESS machine. The primary goal of this chapter is to ascertain if the measures adopted by ESS with regards to HOM mitigation are in the first instance appropriate and in the second, if there is scope to reduce the tolerances. This is a particularly important as ESS has made the decision to break with usual convention of using HOM couplers to damp beam excited HOMs [52, 85]. As a result it is possible for significant voltages to build up in HOMs, which due to the lack of active damping may be long lived and can hence impact on trailing bunches. HOMs that lie on or close to an integer multiple of the bunch frequency may be resonantly driven, resulting in large voltages building up within a particular mode. The code "HOMDynamics" [52] has been used and adapted to confirm and extend the work performed by Ainsworth [52] in analysing the impact of HOMs on the ESS linac. During this study several modules were added to the "HOMDynamics" code to enable the impact of additional cavity,

cryomodules and magnet alignment errors and these additional routines can be applied to any linac which is imported into the code.

Although the work in this chapter is primarily aimed at the impact of HOMs on the beam at ESS it will also highlights general trends in the behaviour of high power proton beams under the influence of HOMs in cavities with accelerating frequencies below 1 GHz. This is a result of several more general investigations where the R/Q, Q and the resonance frequencies have been varied whist using the ESS linac layout as a basis. The result of this is a series of general trends from which the behaviour in similar machines may be drawn.

In a beam dynamics analysis, a particle is usually characterised by its position and momentum relative to the synchronous particle, that is one travelling the ideal path defined by the design of the beam line. In practice particles within a bunch have positions and momenta which differ from the design values and the difference from the synchronous particle is usually written in terms of a 6D phase space containing a momentum and position in each plane of motion. By projecting these parameters in each plane independently, the size of the beam in phase space can be calculated. In the absence of cross-coupling between planes, each is independent and the beam tends to be elliptical in each 2D plane, the area of the ellipse or emittance can be calculated as

$$\epsilon_n = \pi \sqrt{\langle \Delta x_n^2 \rangle \langle \Delta x_n'^2 \rangle - \langle x_n x_n' \rangle^2}, \tag{7.1}$$

where Δx_n is the position and $\Delta x_n'$ is the momentum in one of the planes relative to the synchronous particle. In the longitudinal plane phase and energy are used in place of position and momentum. In an accelerator the parameters used in the phase space are usually the transverse positions and momenta as well as the energy and phase in the direction the beam is travelling.

In this study as the bunch length (3-12 mm) is much smaller than the wavelength of the RF (426 mm), each bunch is considered as a point charge which has its position relative to a synchronous bunch in the same 6D space. By using an analogous system to characterise the position of the bunch in phase space the emittance can also be defined in the same way as for particle within a bunch.

7.1 Beam Physics

In this section the parameters used to track the behaviour of the beam excited HOMs when the linac is modelled are defined. In the ESS design, the bunch length ($\mathcal{O}$mm) is much smaller than the wavelength ($\mathcal{O}$100's mm) of any of the HOMs under consideration, hence the bunches can be treated as point 'like' in the first instance.

When a point charge q, traverses a cavity it excites a voltage in each longitudinal HOM n, according to the fundamental theorem of beam loading [97] given by

$$\Delta V_{q,n} = -q\frac{\omega_n}{2}(R/Q)_n(\beta). \tag{7.2}$$

The voltage excited is damped by lossy processes inside the cavity system caused by couplers and/or resistive materials such as the beam pipe and bellows. The voltage decays according to

$$V_n(t) = \Delta V_{q,n} e^{-t/T_{d,n}} e^{j\omega_n t}, \tag{7.3}$$

where $T_{d,n} = 2Q_{L,n}/\omega_n$ is the decay constant with $Q_{L,n}$ being the loaded quality factor given in terms of the external quality factor Q_{ex} and the quality factor Q_0

by

$$\frac{1}{Q_{L,n}} = \frac{1}{Q_{ex,n}} + \frac{1}{Q_{0,n}}. \tag{7.4}$$

For SCRF cavities such as those at ESS, Q_0 is $\mathcal{O}(10^{10})$ meaning $Q_{L,n} \approx Q_{ex,n}$.

Dipole modes exhibit field profiles which have a zero on-axis electric field, which means that an on axis bunch may not excite a field or experience a kick from these modes. The presence of transverse HOMs will cause a bunch to receive a transverse momentum kick which using the Panofsky-Wenzel theorem [63] is given by

$$\Delta p_{\perp,n} = j\frac{q}{\omega_n}\frac{dV_{z,n}}{dx} = q\frac{V_{\perp,n}}{c}. \tag{7.5}$$

The transverse kick is dominated by the contribution of dipole modes which have an electric field that scales linearly with x. Using this information the transverse voltage for a dipole mode can be written as

$$V_{\perp,n} = j\frac{c}{\omega_n x}V_{\parallel,n}(x,\beta). \tag{7.6}$$

This allows the transverse R/Q to be written as

$$R/Q_{\perp,n}(\beta) = \frac{|V_{\perp,n}|}{\omega_n U_n}. \tag{7.7}$$

Therefore the transverse voltage induced by a bunch can be written as

$$\Delta V_{\perp,n} = \frac{1}{2}jxq\frac{\omega_n^2}{c}R/Q_{\perp,n}(\beta). \tag{7.8}$$

The fact that this voltage is complex means that the exciting charge does not experience the transverse field which it excites—as it is $\pi/2$ out of phase with the excited voltage. For a finite length bunch however it is possible for the tail of a

bunch to experience the transverse fields excited by the head of the bunch. The parameters which have been defined are used when tracking the behaviour of the bunches including HOMs is performed. In following sections the interaction of bunches with the RF system and HOMs is discussed.

7.1.1 The Monopole Interaction

To excite a voltage in a mode the bunch must loose energy to ensure energy conservation is obeyed. The bunch will also be accelerated by any fields already present within the cavity. With these factors considered the energy change of a bunch can be written as

$$\Delta U_n = q\left(\Re(V_n)\cos\left(\omega_n dt\right) - \Im(V_n)\sin\left(\omega_n dt\right)\right) - \frac{1}{2}\Delta V_{q,n} \tag{7.9}$$

where $\Re(V_n)$ and $\Im(V_n)$ are the real and imaginary parts of the HOM voltage already present in the cavity prior to the bunch arrival, taking the phase of the bunch relative to the HOM. The last term is the contribution from the fundamental theorem of beam loading [97] described in appendix A.

7.1.2 The Dipole Interaction

If a complex transverse voltage is present in a HOM a transverse kick will be given to the bunch which is described by

$$\Delta p_x = q\frac{V_{\perp,n}}{c}. \tag{7.10}$$

This momentum kick gives a change in transverse trajectory of

$$\Delta x' = \frac{\Delta p_x}{p_\parallel} = q\frac{V_{\perp,n}}{cp_\parallel} \tag{7.11}$$

where $p_\parallel$ is the longitudinal momentum and $\Re(V_{\perp,n})$ is the real part of the transverse voltage. It is worth noting that there is no analogous effect to the fundamental theorem of beam loading (section 3.1.2) as the exciting bunch is always out of phase with the transverse field.

7.1.3 RF Errors

The voltage inside the accelerating mode of a cavity is not always constant; fluctuations in both amplitude and phase are present even when a LLRF feedback loop is present [36]. The difference in energy gain of the bunch from the synchronous particle is given by

$$\Delta U_{RF} = qV^*_{RF}\cos\left(\phi^*_s + \omega_{RF}dt\right) - qV_0\cos\left(\phi_s\right) \tag{7.12}$$

where V_0 is the nominal RF voltage and V^*_{RF} is the voltage including amplitude errors, ϕ_s is the phase of the synchronous particle and ϕ^*_s is the phase including phase errors caused by jitter from the RF source.

7.1.4 The Drift-Kick-Drift Method

In order to simplify the model whilst still retaining the relevant physics the accelerator is divided up into a series of drifts and kicks as illustrated in figure 7.1. At the mid-plane of each cavity the interaction of the bunch with the HOMs and RF system is calculated as detailed in section 7.1.1. The bunch then gains

the calculated kick and is propagated to the next cavity. The voltage induced is added to the voltage already present and its evolution from bunch-to-bunch is tracked. The drifts used correspond to the spacing of the components in the ESS lattice.

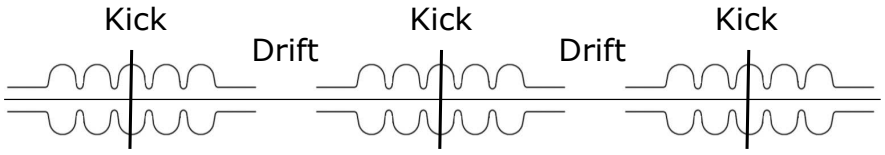

Figure 7.1: Schematic of the Drift-Kick-Drift Scheme.

The total energy change created by the bunches interaction with a cavity m is given by;

$$\Delta E^{(m+1)} = \Delta E^{(m)} + \Delta U_{RF}^{(m)} + \sum_{n} \Delta U_{n}^{(m)}, \tag{7.13}$$

which is the summation of the initial energy error and the addition errors induced by RF errors and HOMs.

This energy error will result in a time arrival error when arriving at the next cavity. This is given by

$$\Delta t^{(m+1)} = \Delta t^{(m)} + \left(\frac{dt}{dE}\right)_{E} \Delta E^{(m)}, \tag{7.14}$$

where the gradient of the time error is dependent on the length of the drift, L, the mass of the particle m_0 and the relativistic factor γ of the particle,

$$\left(\frac{dt}{dE}\right) = -\frac{L^{(m)}}{m_0 c^3 \left(\gamma^2 - 1\right)^{3/2}}. \tag{7.15}$$

A similar scheme can be used in the transverse plane, where the associated transfer matrices are used to track the bunch between the cavity mid-planes.

7.2 Implementation of the Drift-Kick-Drift Scheme

The full ESS bunch train of approximately 1 million bunches is tracked through the linac, at each stage the position of the particles in both the longitudinal and transverse phase space is tracked. Each plane is assumed to be uncoupled and as result each plane can be considered separately. In each simulation a check on the conservation of emittance for the baseline simulation is performed provided only conservative forces are present to ensure the code is obeying Liouvilles theorem [12] and behaving in the expected manner. When additional non-conservative effects are included (such as wakefields) Liouvilles theorem no longer holds and hence no check of this kind is applied in this circumstance. Finally the change in the HOM voltages are tracked and the evolution from bunch-to-bunch is calculated.

7.2.1 Longitudinal Plane

For the design of the ESS linac the cavity voltages and synchronous phases have been calculated from the lattice using the computer code TraceWin. TraceWin is used for linear and non-linear calculations for 2D or 3D ion or electron beams [124]. The information from this is combined with data from cavity simulations given in chapter 5. In the simulations a particle is defined as lost if it is outside the range

$$2\phi_s < \phi < -\phi_s \tag{7.16}$$

where ϕ_s is the synchronous phase which in the linac convention is negative. This range of stable phase can be calculated analytically and is shown in [125]. In the simulation of longitudinal effects the behaviour of the beam in the transverse plane is neglected because it is assumed that the planes are uncoupled.

7.2.2 Transverse Plane

In the transverse plane only, the x-plane is considered and the transfer of the particles from cavity-to-cavity is performed using 2D transfer maps extracted from TraceWin by collaborators at ESS [126]. The transfer map describes the evolution of a particles position and momentum through each accelerator element.

Initially the case where no alignment issues are present is considered, unless stated otherwise. In the later analysis inclusion of alignment errors is discussed in detail.

7.2.3 The Beam Dynamics Tracking Code

The code was originally written in the Python programming language by R. Ainsworth [52, 85] based on work by M. Schuh et al. [127] and used in the design stage for ESS with the results included in the ESS technical design report [36]. I have added several features to the code to allow for additional errors to be included and to allow the manipulation of individual properties of the cavities and HOMs. In particular these include the ability to offset cavities, cryomodules and the beam axis in the transverse plane as well as to introduce errors in the quadrupole magnets alignment. Further routines were introduced to allow greater control of the HOM frequencies and R/Q's which are the primary inputs for the control of the HOM behaviour.

The simulations have been performed in a parallel manner with early simulations being run on local machines with 48 cores and 128 Gb of RAM. This was extended for use on the University of Manchester Engineering and Physical Sciences HTCondor pool [128] which allows access to over 3,000 CPU cores with approximately 4 Gb of RAM each. This has allowed many simulations to be performed which allows for samples with a statistical significance of $\sim 3\sigma$ to be

obtained when random errors are included.

7.2.4 Mode Frequency Spread

Due to the limited manufacturing accuracy attainable when producing SCRF cavities through the deep drawing process, a spread in the cavity frequency spectrum from the design values is inevitable [129]. In the case of the accelerating mode the frequency is tuned by deforming the cavity. However the shape may still differ from the design which can result in a large spread in mode frequencies for all other modes from the design values.

An empirical formula derived by Sundalin and discussed by Molloy [129] indicates that the standard deviation in measured frequencies for the n^{th} mode within the accelerating mode's passband is given by

$$\sigma_n = 1.09 \times 10^{-3} \times |f_n - f_\pi|, \tag{7.17}$$

where f_n is the simulated frequency and f_π is the frequency of the accelerating mode. From Sundalin's study modes in all bands other than the accelerating modes band will have a maximum frequency shift of 0.38% from the simulated value. This study was based on empirical evidence from previous cavities for use in SNL and was confirmed during the production of the cavities for SNS [129]. These formula are applied to both the longitudinal and transverse beam dynamics simulations as the maximum frequency deviation.

7.2.5 Statistical Distributions

Throughout this analysis liberal use of statistically generated numbers have been made to allow bunch distributions and errors in cavity parameters to be generated.

The first statistical distributions which has been primarily used is the normal or Gaussian distribution

$$P(x) \propto e^{(x-\mu)^2/2\sigma^2}, \tag{7.18}$$

where μ is the mean and σ is the standard deviation. The other distribution is the uniform or top-hat distribution given by

$$P(x) \propto \begin{cases} 0 & x < -\sigma \\ 1 & -\sigma < x < \sigma \\ 0 & x > \sigma \end{cases} \tag{7.19}$$

where σ is the half-width of the distribution. Both the uniform and Gaussian distributions are displayed in figure 7.2.

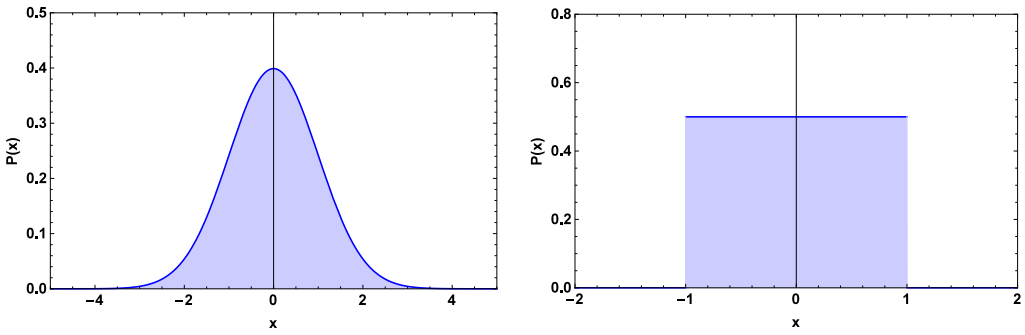

(a) Gaussian Distribution (b) Uniform Distribution

Figure 7.2: The normal and uniform distributions both with a $\sigma = 1$ and $\mu = 0$.

The Gaussian distribution is the most common distribution found when looking at random errors and is heavily used in statistical analysis. The only issue with the Gaussian distribution in this application is that in principle the tails of the distribution extend to infinity with ever decreasing probability of occurring. However in most applications here this is not the case, therefore the distribution is truncated to $\pm 3\sigma$ containing 99.7% of the data due to the low population of the

tails. In the uniform distribution all values within $\pm\sigma$ are equally likely to occur right up to the boundary. For a random statistical sample of a normally distributed system a sample size of 1,000—which is used in most of the simulations in the following chapters—has a statistical significance of 2.5σ.

7.3 Longitudinal Dynamics

The longitudinal dynamics of the ESS linac under the influence of monopole HOMs are considered independently from the transverse plane. The initial state of the beam is assumed to be Gaussian with a RMS energy and phase spread of 79 keV and 5 degrees in phase at 704 MHz. In each simulation the bunch distribution are generated using the Mersenne-Twister generator [130] and beam current errors of 1% are included.

Simulations of the impact of RF errors on the emittance of the beam at the level of 0.1% in amplitude and 0.1 degrees in phase are used as a baseline from which the growth under the influence of HOMs is compared.

In the following subsections the influences of modes in the accelerating passband and HOMs will be discussed.

7.3.1 RF Errors

RF errors are predominately caused by fluctuations in amplitude and phase from the RF source. Jitter in the phase and amplitude of the RF system can lead to significant growth in the energy and phase spread of the beam. The fluctuations in the system are constantly monitored using the Low Level RF (LLRF) [131] and is anticipated that control of the RF at the 0.1% amplitude and 0.1 degree in phase level will be achieved. To assess the impact of this level of fluctuation

1,000 simulations have been performed, an example of the input and output distributions are given in figure 7.3.

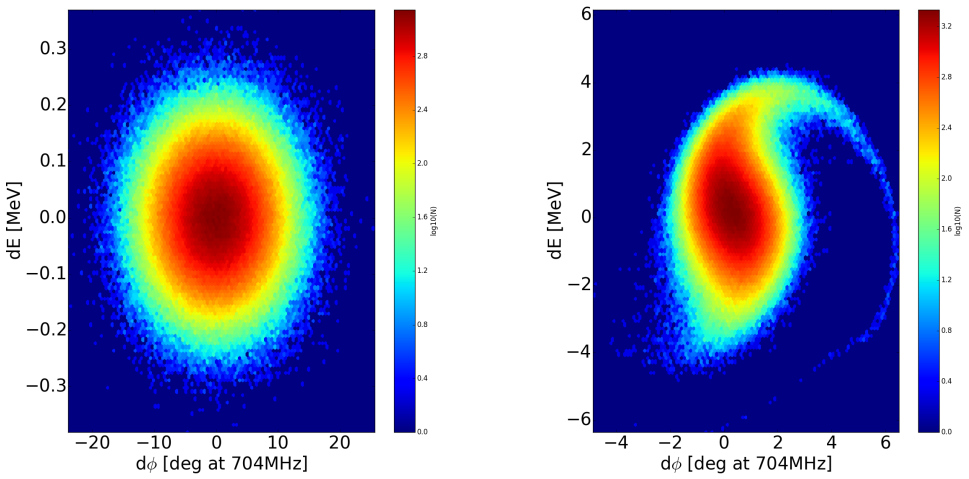

(a) Input Distribution (b) Distribution at the end of linac

Figure 7.3: Examples of the input distribution and output distributions of the longitudinal beam profiles under the influence of RF errors of 0.1% and 0.1 degrees in amplitude and phase.

The average growth observed was as the 17% level and will be used as a base line for measuring the effect of beam excited modes.

7.3.2 The Influence of Passband Modes

The beam is tracked through the linac with one passband mode included per cavity. The frequency of each mode is randomly varied according to the formula calculated by Sundalin (Equation 7.17), details of each mode used are given in table 7.1.

This process is repeated 1,000 times for various beam currents and damping levels without RF errors included. The average and maximum growths observed are displayed in figure 7.4.

In figure 7.4 the growth at $Q_{ex} < 3 \times 10^6$ is negligible, however at large Q_{ex}

Cavity	Spoke	Medium-β	High-β
Mode	0	$5\pi/6$	$4\pi/5$
Frequency (MHz)	362.70	703.89	703.22
σ_f (MHz)	0.011	0.0013	0.0013
Max R/Q (Ω)	96.95	179.28	73.86

Table 7.1: Summary of cavity parameters used in passband mode simulations.

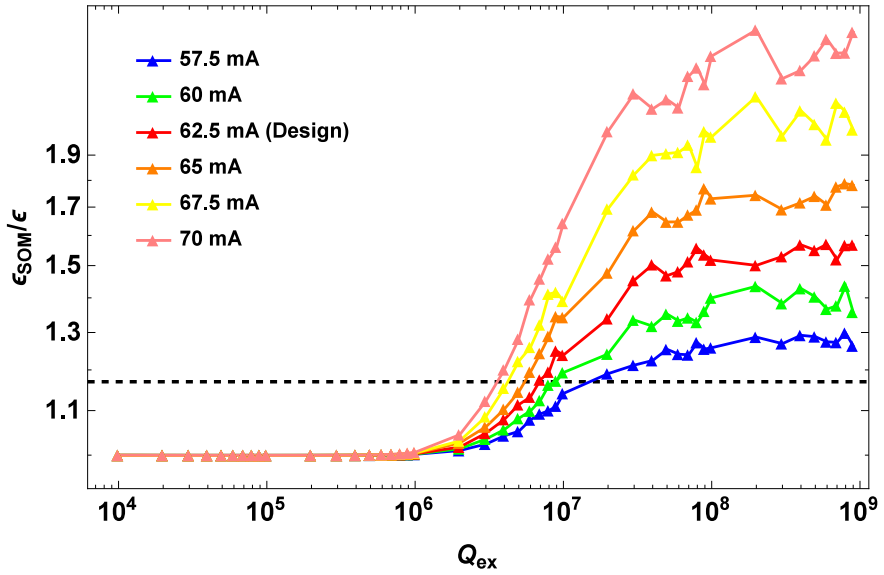

Figure 7.4: The average growth observed due to the influence of passband modes at various currents and damping levels. The dashed line is the dilution due to only RF errors.

the growth can be very significant. As a result the Q_{ex} of around 10^6 should be considered a the maximum allowed for these modes. It is anticipated that the damping of passband modes will be at a similar level to the accelerating mode as they are close enough in frequency that they should be damped at a similar level by the FPC. For each cavity the $Q_{ex} < 8 \times 10^5$ [36] and hence passband modes should not have a significant impact on the beam at ESS.

7.3.3 Impact of Longitudinal HOMs

To assess the impact of longitudinal HOMs on the ESS beam the accelerator was simulated including the HOMs with the highest R/Q in each cavity at various currents and damping levels. This was performed for a series of Q_{ex} and beam currents and the results are illustrated in figure 7.5. In addition this was repeated including the six highest R/Q modes in each cavity and the results are plotted in the same figure.

The growth observed in these simulations is negligible and hence HOMs are of little concern. This is primarily due to the low R/Q values of HOMs associated with cavities of low operating frequency and large irises, as expected due to the scaling of the longitudinal wakefield with frequency, which is $W_{\parallel} \propto \omega^2$ detailed in appendix C.

The exception to this is if a mode is resonantly corresponding to excitation at a harmonic of the bunch frequency (352.21 MHz). The impact of resonantly driven HOM on the beam will be discussed in detail in section 7.5.

7.4 Transverse Dynamics

The transverse dynamics have been modelled using 2D transfer maps extracted in TraceWin [124]. The spread in the mode frequencies was calculated using Sundalin's formula (see section 7.2.4) as in the case of longitudinal HOMs. All simulations use an input distribution of Gaussian profile with widths of 1 mm in x and 0.5 mrad in x'. In this section the impact of transverse HOMs will be analysed and the effects of various miss-alignments will be detailed.

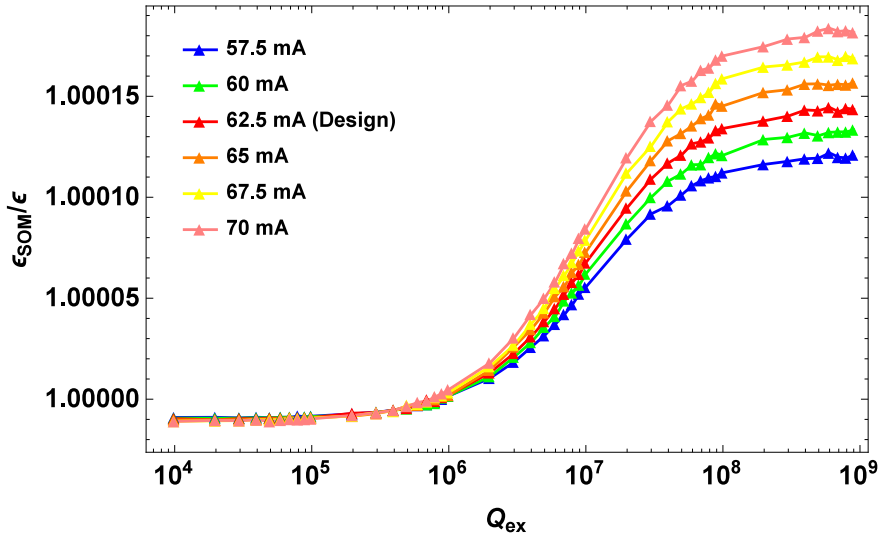

(a) Highest R/Q mode

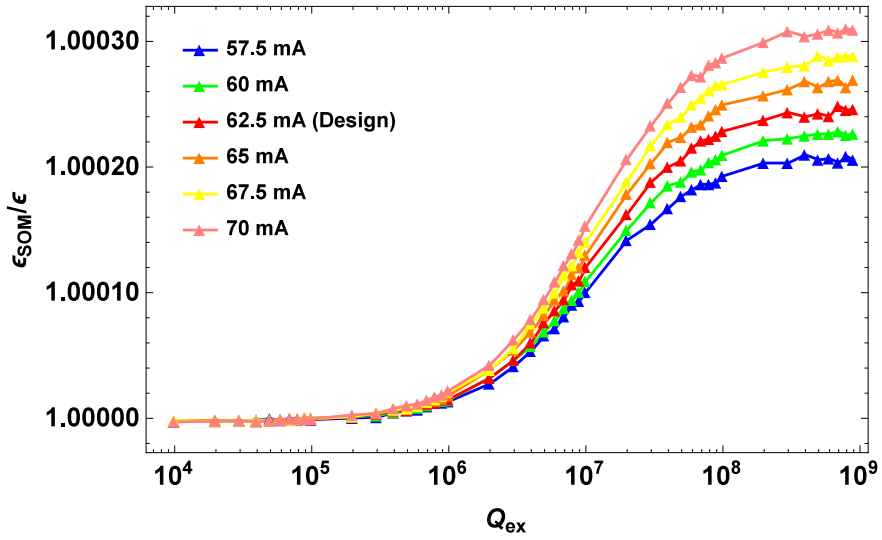

(b) Highest six R/Q modes

Figure 7.5: The average growth observed due to the influence of longitudinal HOMs at various currents and damping levels.

7.4.1 Transverse HOMs

In these simulations the modes which have the highest $(R/Q)_\perp$ in each cavity have been used and the damping factors and currents are varied. The results of the simulations are shown in figure 7.6 where each data point is the average value of 1,000 simulations. This was repeated including the six highest R/Q modes

which account for over 70% of the total kick factor of the first 60 modes and the results are also shown in figure 7.6.

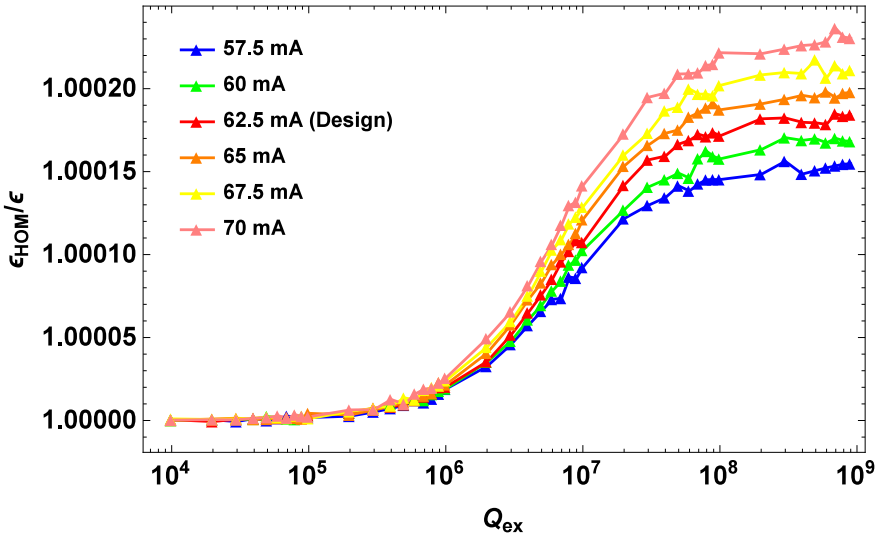

(a) Highest R/Q mode

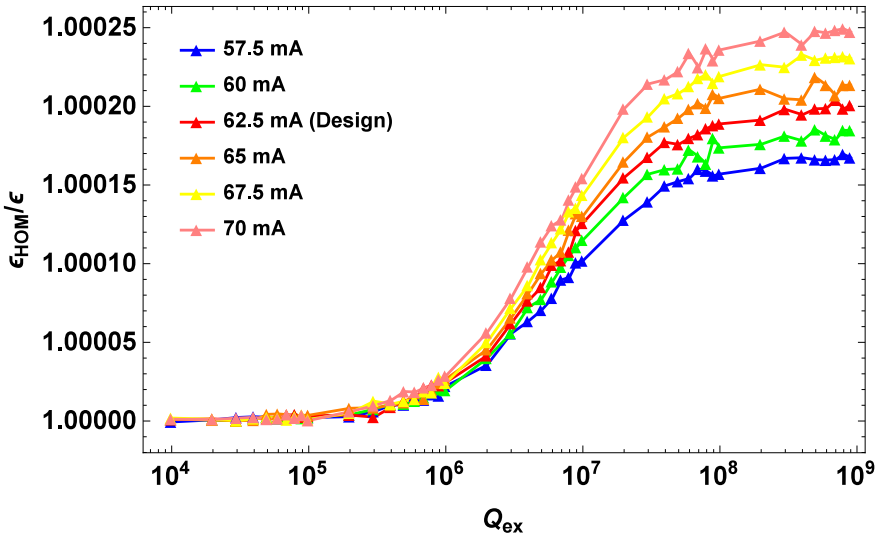

(b) Highest six R/Q modes

Figure 7.6: The average growth observed due to the influence of transverse HOMs at various currents and damping levels.

In figure 7.6 the growth in all cases is negligible and corresponds to little more than numerical noise. As a result of this it is not expected that transverse HOM will be a problem for ESS. This again consistent with what is anticipated

due to the scaling of the transverse wakefield with frequency which is detailed in appendix C.

Further unlike longitudinal HOMs which can build up large voltages which effect the beam when resonantly driven which can impact the beam the transverse HOMs cannot. This is due to the excited voltage being out of phase with the beam as the excited voltage is imaginary. Although this can have no impact on the beam it is possible that such a voltage could build up and have implications in terms of cavity performance through providing additional heat load on the cavity.

7.4.2 Cavity and Cryomodule Alignment

There is a finite accuracy attainable when aligning each of the components of the accelerator. If a cavity is transversely misaligned then each bunch will pass through the cavity off-axis and will excited dipole fields which can degrade the beam quality. Further the cavity may be aligned such that there is an angle between the beam axis and the cavity axis, this can lead to a transverse kick due to the accelerating mode which can affect the beam. In the following sections these effects will be considered and a comparison to the impact of misalignments in the quadrupole magnets is given.

In order to assess the impact of misalignment errors on the emittance dilution I added random errors to the beam dynamics simulations. The errors added to the cavity alignment followed a Uniform (or Top-Hat) distribution of various widths. The beam was then tracked through the linac under the influence of the six highest $(R/Q)_\perp$ HOMs in each cavity, with frequency errors included with a $Q_L = 10^8$. For each magnitude of errors 1,000 simulations are performed and the dilution is taken. The mean growth in the transverse beam size is shown in

figure 7.7.

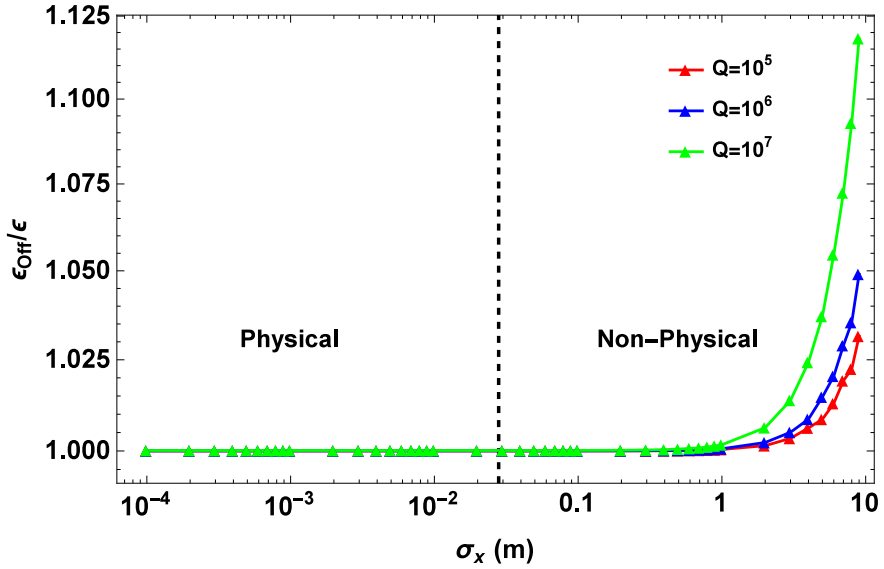

Figure 7.7: The average emittance growth observed due to the influence of transverse HOMs including cavity misalignments.

For all possible alignments situations almost no growth is observed, however by allowing the beam to be offset beyond the cavity iris growth is observed which shows that although the codes is not showing any dilutions in the case at hand it is possible for there to be growth if the R/Q and/or offsets were larger. The reason for this lack of degradation is that the kick factors for the modes are so small that at any physical offset only an insignificant voltage is present.

To test if more systematic shifts result in larger emittance dilution, misalignments of each cryomodule are incorporated. This means that in the spoke section, pairs of cavities are shifted by equal amounts and in the elliptical cryomodules four cavities are shifted equally. The rest of the setup is the same as for individual cavity misalignments and the result are shown in figure 7.8.

In figure 7.8 little growth is seen again which suggests that transverse alignment errors have little impact on the beam when only the behaviour of HOMs is considered. This supports the decision to operate ESS without HOM coupler

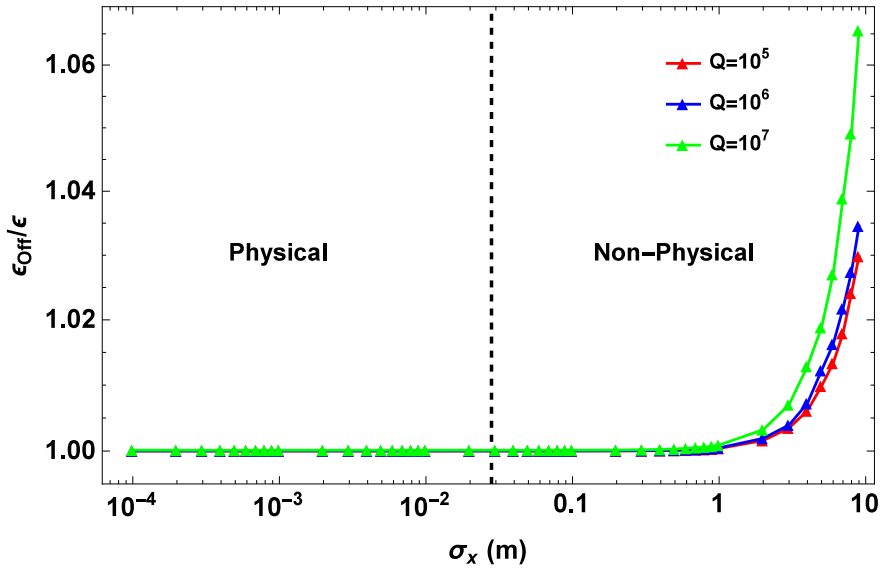

Figure 7.8: The average emittance growth observed due to the influence of transverse HOMs including cryomudule misalignments.

being incorporated to damp the beam excited fields.

Magnet Misalignments

To set the size of the effect of cavity misalignments in context, errors have been applied to the quadrupole magnets in the linac. This was achieved by adding a misalignment factor δ to the transfer matrices of the quadrupole magnets. The was achieved by replacing the quadrupole matrices with

$$\begin{pmatrix} M_{11} & M_{12} & 0 \\ M_{21} & M_{22} & 0 \\ 0 & 0 & 1 \end{pmatrix} \begin{pmatrix} x \\ x' \\ 1 \end{pmatrix} \Longrightarrow \begin{pmatrix} 1 & 0 & \delta \\ 0 & 1 & 0 \\ 0 & 0 & 1 \end{pmatrix} \begin{pmatrix} M_{11} & M_{12} & 0 \\ M_{21} & M_{22} & 0 \\ 0 & 0 & 1 \end{pmatrix} \begin{pmatrix} 1 & 0 & -\delta \\ 0 & 1 & 0 \\ 0 & 0 & 1 \end{pmatrix} \begin{pmatrix} x \\ x' \\ 1 \end{pmatrix} \tag{7.20}$$

where δ is the misalignment. This method amounts to shifting the beam in x, by δ and then applying the transfer matrix of the quadrupole before shifting the beam back. This method is equivalent to moving the quadrupole itself off axis, which is the effect of interest. This was not in the original code but has been

added by me and is implemented as an optional sub-routine.

In the simulations uniform random errors are applied to each magnets position and the beam is tracked trough the linac with no other effects included. This is repeated 1,000 times for each alignment and the mean growth is shown in figure 7.9.

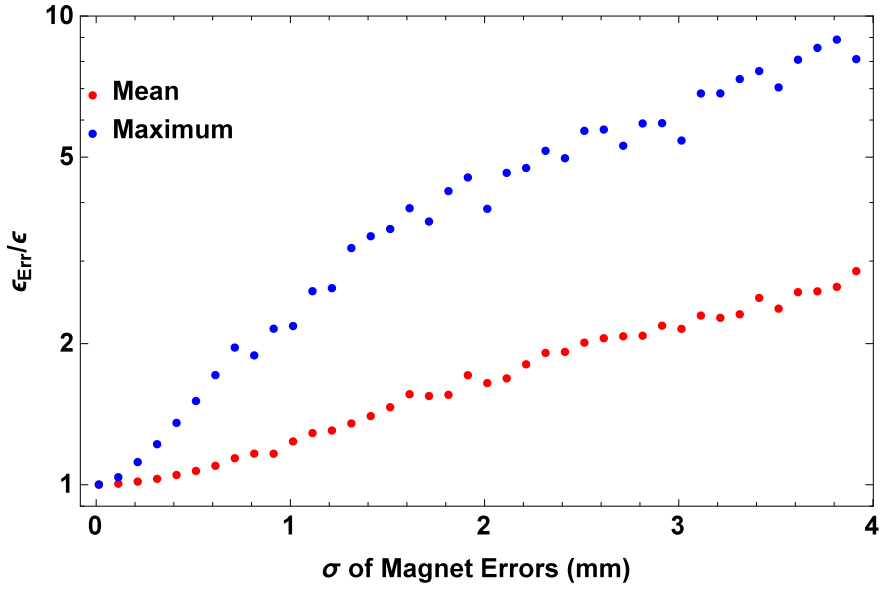

Figure 7.9: The average growth observed due to magnet misalignment errors.

The errors observed due to magnets errors are at a much greater level than due to transverse HOMs with the same magnitude of errors. This is a strong indication that magnet alignment is much more crucial to the operation of ESS than cavity alignment.

Angular Misalignment

If a cavity is placed at an angle within the cryomodule the accelerating field of the cavity will contain a transverse component, which to first approximation will be given by

$$V_{\perp} = V_{acc} \sin(\theta) \approx V_{acc}\theta, \tag{7.21}$$

where the small angle approximation ($\sin\theta \approx \theta$) has been used. This is valid as the values of θ involved are small for example; to achieve 1% error in voltage an angle of 0.24 radians must be used, for a 1 m cavity this corresponds to displacements of ±120 mm. An error of ±0.5 mm at either end of the cavity correspond to a maximum angle of 1 mrad for a 1 m cavity. In a cavity at a 1 mrad angle the transverse component of a 18 MV/m cavity is 18 kV/m which is a significant transverse voltage when compared to the voltage which is present in beam-excited transverse HOMs.

In these simulations, errors following a uniform distribution of fixed width have been applied to each cavity and 1,000 simulations performed at each set of errors. The results of which are shown in figure 7.10.

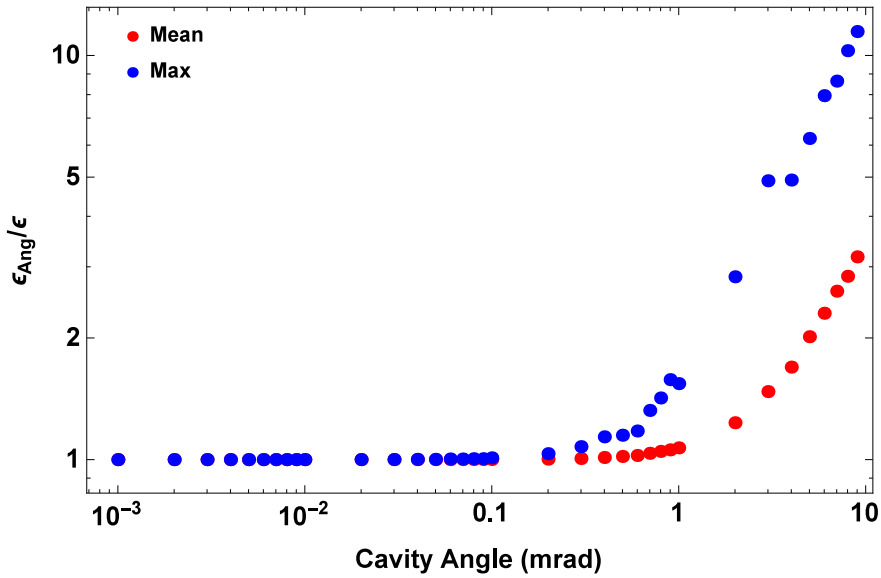

Figure 7.10: The average emittance growth observed due to angular misalignment errors on the cavities.

Even for relatively small angular errors the growth in emittance can be significant and is much greater than due to HOMs. With errors of the order of 1 mrad being likely it is almost certain that the contribution from angular alignments will be the dominant contributor to transverse growth due to the cavities.

7.4.3 Transverse Dynamics Summary

The impact of dipole HOMs on the beam at ESS is negligible even if the HOM is resonantly driven due to the low kick factors of every mode resulting from the low cavity frequency and large irises. In addition when the cavities are subjected to transverse misalignments negligible additional emittance dilution is present.

This is in contrast to the situation with transverse alignment errors in the magnets (section 7.4.2) or angular alignment errors on the cavities (section 7.4.2) which can cause significant degradation of the beam. As such angular alignment of the cavities and transverse alignment of the magnets should be given significant consideration at ESS.

Due to the lack of influence of dipole modes on the beam no additional damping should be required to mitigate their effects. Hence this is a confirmation and extension of the work carried out in [85] on the early linac designs.

7.5 HOMs Near Machine Resonances

The baseline ESS design opted to dispense with HOM couplers and this is based primarily on the results obtained in [85], which indicated no adverse effects on the beam due to HOMs. This decision relies on the low R/Q of both longitudinal and transverse HOMs resulting minimal impact on the beam. It was shown that resonantly driven HOMs can significantly degrade the beam in [36, 85] and as such ESS took steps to prevent its occurrence by placing a requirement that HOMs be at least 5 MHz from harmonics of the bunch frequency.

This requirement has been met in the design stage for each cavity with a margin of about 10 MHz in each cavity which has been shown in chapter 5. This amount of separation from the machine resonance allows for a 5 MHz shift due

to manufacturing errors towards the nearest harmonic of the bunch frequency compared to the designs.

In the first two prototype high beta cavities, the final requirement of 5 MHz was not met and these cavities would of course have been rejected by ESS. The reason for such large shifts was due to a significant error in the end-cells of the cavity which were 1.2 mm from the design [114]. As it has been shown practically that cavities can fail to meet this criteria it is a real concern during cavity production. As a result of this data, a detailed assessment of the ESS limit of 5 MHz was required.

7.5.1 Analytical Analysis of HOM Voltages

The growth in the HOM voltage for modes in the ESS cavities can be calculated analytically using the sum wakefield defined in section 3.5. As the modal expansion of the wakefield is used the sum wakefield can be truncated to include only a single mode which is of most concern allowing for faster calculation times.

It was shown in figure 5.23 that the sum wakefield for each of the cavities does not reach a magnitude that would be of concern in terms of beam dynamics. However if the frequency of a mode shifts then this may no longer be the case. To investigate this, the mode which is closest to a harmonic of the bunch frequency was shifted to lie exactly on the harmonic. The sum wakefield for the resonantly driven HOM in the last medium-β cavity is shown in figure 7.11 for various values of damping.

It can be seen in figure 7.11 that unless strong damping is present the voltage in the HOM can build quickly as the bunch train traverses the cavity. In the worst case this can result in 10's kV/pC/m of voltage being excited. This is the worst case, where the mode lies exactly on a harmonic of the bunch frequency

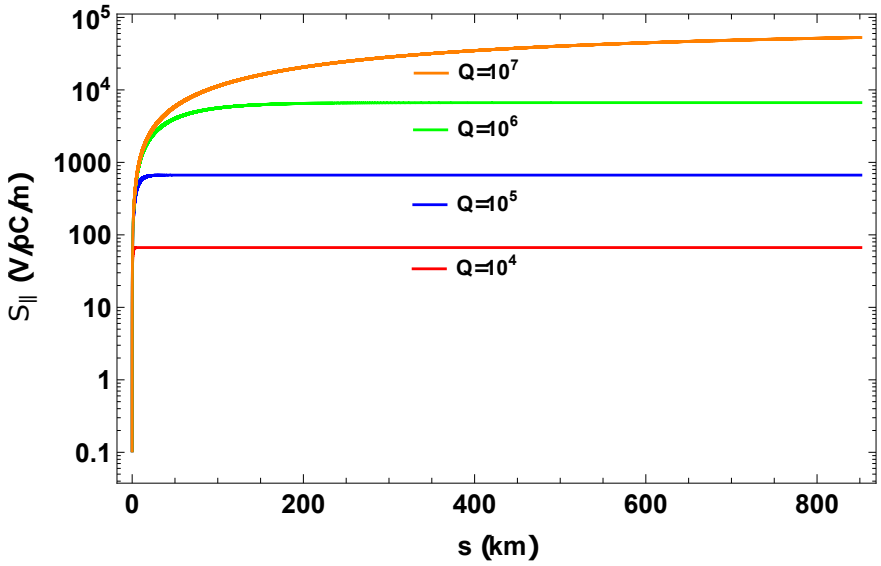

Figure 7.11: The sum wakefield at various values of Q_L for resonantly driven HOMs in the ESS elliptical cavities.

and there is no spread in the phase of the bunches. However it is clear indicator that further in depth study of this behaviour was required.

The effect of resonant growth is a function of the driving frequency, amplitude and damping level of the system. The bandwidth of a resonance is given by

$$\Delta\omega = \frac{\omega_r}{2Q}. \tag{7.22}$$

Typically frequencies in the ESS cavities are on the order of 1 GHz with $10^4 < Q_L < 10^7$ which means the width of the resonance is in the range of 0.5 to 300 kHz. This is much narrower than the current ESS limit of 5 MHz and suggests a reduction in this tolerance may be possible. To test if this reduction is possible in practise, simulations of the effects of reducing the frequency tolerance on the beam are required and are detailed in the following section.

In this study the effects of random frequency errors and variation in the values of R/Q and Q were focused on prior to looking in detail at the degradation caused

when the frequency of each HOM of concern in each cavity is shifted away from the harmonic of the bunch frequency.

7.5.2 Growth With Random Frequency Errors

The simplest approach to investigate the effects of cavities near to harmonics of the bunch frequency, is to adopt a statistical approach as performed in [85]. In this approach, the linac is simulated many times with the frequency of the HOMs varied according to a known distribution. This approach was performed initially with the frequency of the HOM of concern in the medium-β section of the linac shifted to lie on the 5^{th} harmonic of the bunch frequency and then for the first mode in the 3^{rd} passband and in the high-β section the 1^{st} mode in the 2^{nd} passband is shifted to the 4^{th} harmonic.

To these new central frequencies, a Gaussian distribution of frequency errors of width 1 MHz have been applied with the Q_L of the mode set to between 10^5 and 10^8 in logarithmic steps. The data taken from 10,000 of these simulations at each setting is summarised in tables 7.2 and 7.3. In addition, a summary of the maximum and average dilutions is shown in figure 7.12.

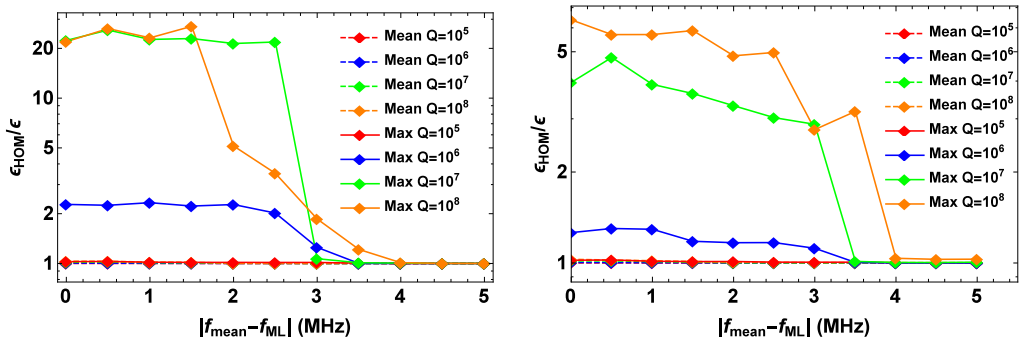

(a) Medium-β section (b) High-β section

Figure 7.12: Frequency separation from machine resonances that the dilution becomes negligible in each of the elliptical cavities at ESS.

The data shows a significant number of linacs which exhibit large growth

$\lvert f_{ave} - f_{ML} \rvert$	$Q = 10^5$	$Q = 10^6$	$Q = 10^7$	$Q = 10^8$
0.0	0	90	70	105
0.5	0	71	67	105
1.0	0	43	36	62
1.5	0	27	27	47
2.0	0	9	3	9
2.5	0	4	3	3
3.0	0	1	0	2
3.5	0	0	0	1
4.0	0	0	0	0
4.5	0	0	0	0
5.0	0	0	0	0

Table 7.2: Number of events which exhibited a growth of more than 17% when the 1749.59 MHz mode frequency in the medium-β cavity is shifted away from the nearest machine harmonic.

$\lvert f_{ave} - f_{ML} \rvert$	$Q = 10^5$	$Q = 10^6$	$Q = 10^7$	$Q = 10^8$
0.0	0	11	157	208
0.5	0	12	152	189
1.0	0	6	90	126
1.5	0	3	57	66
2.0	0	0	16	30
2.5	0	0	7	13
3.0	0	0	4	3
3.5	0	0	0	1
4.0	0	0	0	0
4.5	0	0	0	0
5.0	0	0	0	0

Table 7.3: Number of events which exhibited a growth of more than 17% when the 1408.84 MHz mode frequency in the high-β cavity is shifted away from the nearest machine harmonic.

which is consistent with the study performed in [85]. However, this study has 100 times more events making it statistically more significant sample and hence more detailed analysis of the results is possible. One key point is that the average growth seen is negligible even though the maximum values are large. This is an indicator that only in very rare instances does significant growth occur. The numbers in both tables are consistent with what is expected if we consider the

number of modes within around 1-10 kHz of the machine line, using a purely statistical approach through the use of cumulative distribution functions. This clearly indicates that only modes which lie very close (< 5 kHz) to the machine harmonic contribute to the dilution. A more systematic approach which will clearly illustrate this is found in the next section.

7.5.3 Impact of Reducing the ESS Limit

The ESS has set a hard limit of 5 MHz of separation between all longitudinal HOM frequencies and the nearest harmonic of the bunch frequency. This tolerance was set based on work carried out in [52, 85] which indicated that at least 5 MHz was required to mitigate any effects. This tolerance has proved problematic in the first high-β prototype cavities [114] which had HOM frequency shift of $\sim$ 10 MHz to lie right on top of the 4^{th} harmonic of the bunch frequency. As a result of this the manufactures of the cavities will take greater care to prevent deviations form the designs. For example by selecting the best cells for the centre of the cavity the first medium-β prototype has achieved a frequency separation of 20 MHz, which is 10 MHz more than the design [113].

The methods that have been adopted should reduce the chance of the HOMs shifting onto the resonance of the bunch frequency, however in producing 120 elliptical cavities large shifts are still a distinct possibility. Having cavities which fail to meet this tolerance could have a significant impact on the construction time scale of the project and machine performance, if problem is not detected.

To test if it is possible to reduce the tolerance each HOM of concern is shifted one-by-one onto the nearest harmonic of the bunch frequency and shifted away in steps of 100 Hz at several values of Q_{ex}. Plotted in figure 7.13 is the frequency difference at which the HOM in each cavity causes degradation below the 1%

level.

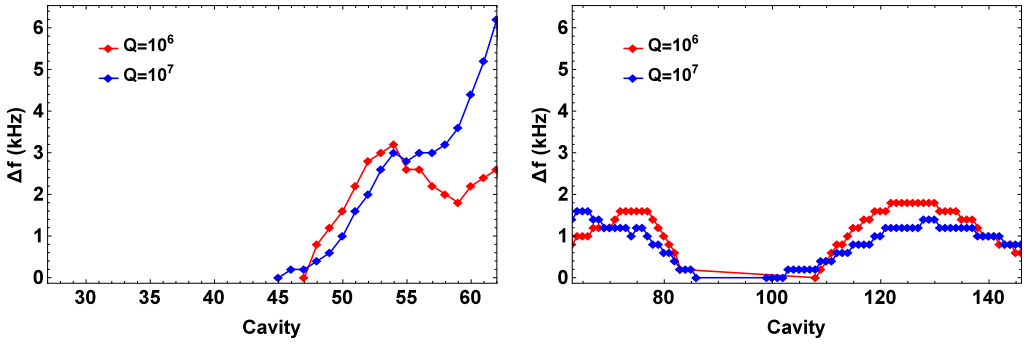

(a) Medium-β section (b) High-β section

Figure 7.13: Frequency separation from machine resonances that the dilution becomes less than 1% in each of the elliptical cavities at ESS.

In figure 7.13 when a HOM is 6 kHz away from the nearest harmonic of the bunch frequency the resulting dilution is negligible. This value is nearly three orders of magnitude lower than the current ESS tolerance of 5 MHz and is a strong indicator that the tolerance is stricter than necessary and could be reduced to the kHz level if the frequency did not vary during operation.

There is a finite limit on how much the tolerance can be reduced due to the possibility of the HOM frequency shifting during operation as a result of the cavity tuners. Consequently the HOM tolerance must include this as a criteria and any change to the tolerance must clearly state what the separation must be at the extremes of the cavity tuning system. For example the tuning sensitivity of the HOM in the medium-β cavity is approximately 800 kHz/mm [132] compared to the 200 kHz/mm for the accelerating mode and the tuning range is ± 3 mm [36]. This results in a HOM tuning range of ± 2.4 MHz at the maximum extension of the tuner, therefore the HOM should be at a minimum of 2.5 MHz from the harmonic of the bunch frequency to eliminate any risk of tuning the frequency onto it.

7.5.4 Impact of the Cavities Position in the Linac

As the beam progresses down the length of the linac both its velocity and the shape of its longitudinal phase space change significantly. In particular when the phase space is wider the excited voltage may be out of phase with the voltage excited by previous bunches resulting in a reduced effect. The variation in the bunch velocity result in a significant variation of the R/Q from cavity-to-cavity. As a result the impact of the cavity on the beam may vary from cavity-to-cavity, which leads to the possibility of regions where a reduced impact on the beam may be present.

To analyse this effect the linac has been simulated 50 times with a single cavity lying exactly on the machine harmonic. The mean growth of the emittance at various Q_L has been plotted as a function of β with the R/Q also shown in figure 7.14.

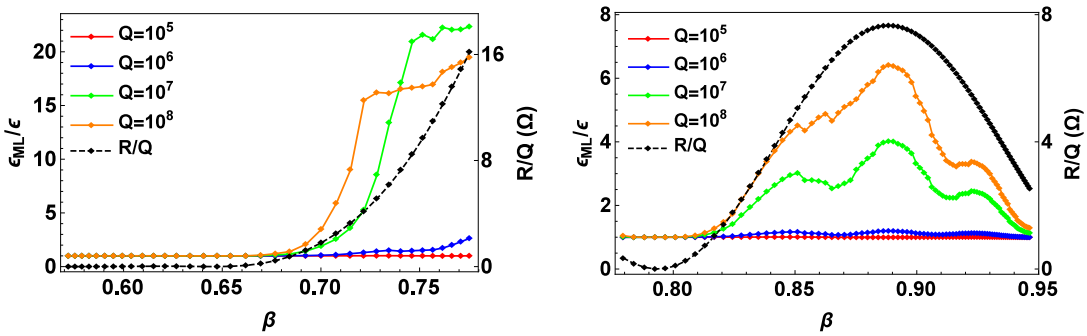

(a) Medium-β 1749.57 MHz mode (b) High-β 1419.23 MHz mode

Figure 7.14: Variation of emittance dilution due to a single mode lying on the nearest machine resonance as a function of the cavities position in the linac.

The variation in the growth, particularly with high Q_L, is evident and in both cases the variation closely follows the R/Q distribution, as expected with some variations due to the shape of the phase space at the specific cavity. In the medium-β section there is a region of around 16 cavities which have a minimal

impact on the beam and in the high-β section there is a similar region with eight cavities. These regions open up the possibility of allowing cavities which fail to meet the ESS criteria being installed early in the production process or to the possibility of cavity sorting. Neither of these is ideal, with the latter providing problems for an installation schedule. However the idea that early errors may have a minimal impact are reassuring as initial problems in the production process are quiet possible.

7.5.5 Impact of Varying R/Q and Q

If a bunch lies on or near a harmonic of the bunch frequency then the voltage excited in the mode by the train strongly depends on how close the HOM frequency is to the resonance which controls the phase that the complex voltage is added, the R/Q which dictates the voltage added per bunch and also the Q_L which determines the damping level. Each of these can have a significant effect on the final result the mode has on the beam. Here the impact of R/Q and Q_L will be discussed in detail with the effect of the mode frequency in the following section.

The effects of R/Q and Q_L allow the worst case scenarios to be investigated, which is that the mode is right on top of the harmonic of the bunch frequency. In testing the effects of Q_L on the performance of ESS the frequency of each HOM which is closest to a harmonic of the bunch frequency is shifted onto that nearest harmonic. This is done individually for each cavity and the Q_L is varied in logarithmic steps from 10^3 to 10^9. In figure 7.15 the level of damping at which the degradation exceeds that caused by RF errors (17%) is plotted for each of the two families of elliptical cavities.

The data in figure 7.15 indicates that if the Q_L is below 3×10^5 in the medium

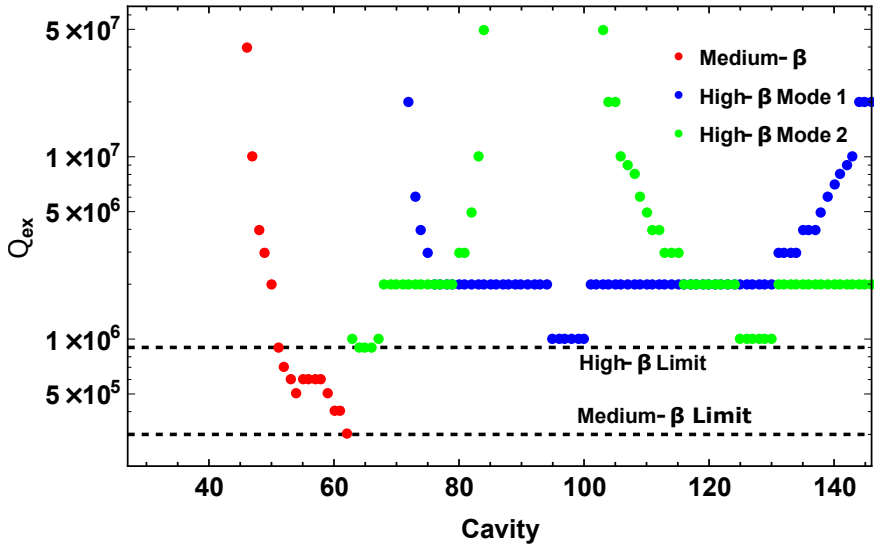

Figure 7.15: Q_L level required to mitigate the impact of resonantly driven HOMs to below the level due to RF error in each cavity.

beta cavities and below 9×10^5 in the high beta cavities then no significant degradation of the beam is seen. If the Q_L of the HOMs can be verified to be significantly below these values then the frequency limit could be reduced or even removed. Damping at this level from the FPC is unlikely and is more likely to be achieved using HOM couplers and hence this study

As the final R/Q for each mode may vary from cavity-to-cavity due to differences in the field shape between the final cavities and the design. To allow this and new designs to be checked easily the R/Q of each cavity in the linac has been varied in logarithmic steps from 0.01 to 100 Ω at several values of Q_L, the results are shown in figure 7.16.

In figure 7.16 a clear trend for the allowable R/Q to increase along the linac which is a result of the increasing rigidity of the beam as it gains energy. Further oscillations which correspond to the oscillation between energy and phase spread can also be seen throughout the length of the linac.

This analysis has allowed for limits to be put on the damping requirements

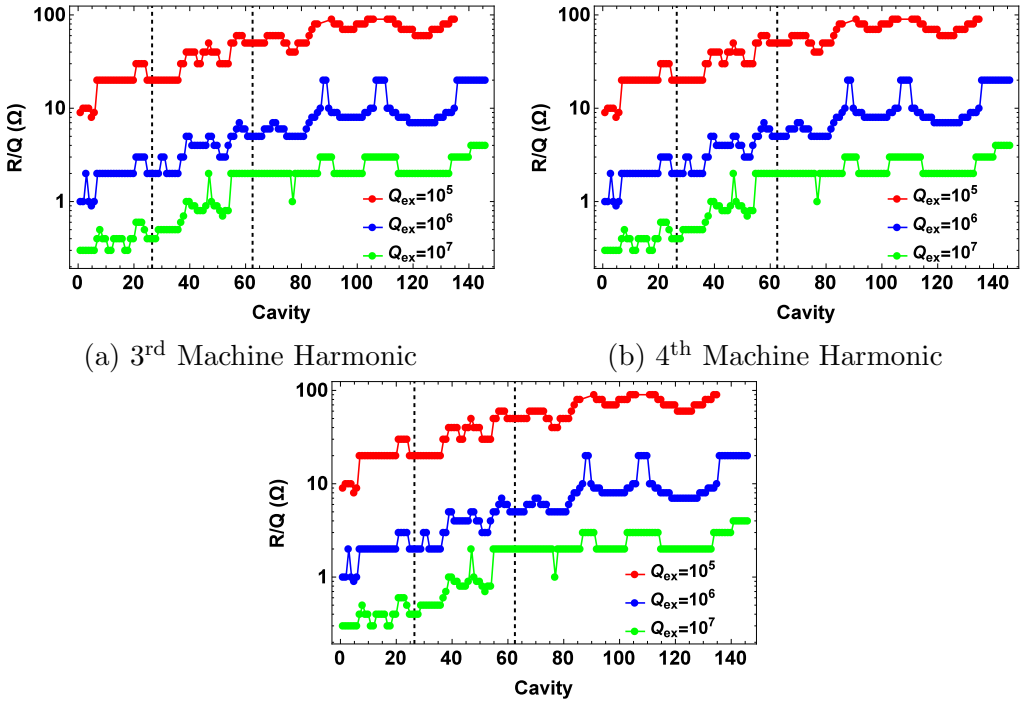

(a) 3rd Machine Harmonic

(b) 4th Machine Harmonic

(c) 5th Machine Harmonic

Figure 7.16: The R/Q which is required to degrade the beam more than the level caused by RF errors when a mode lies on the 3rd, 4th and 5th harmonics of the bunch frequency.

to fully mitigate the impact of resonantly driven HOMs on the beam and to also apply limits to the R/Q if the cavity designs were to be changed resulting in different HOM spectra.

7.6 Beam Dynamics Summary

It has been shown that unless a longitudinal HOM is resonantly driven that HOMs have little effect on the beam at ESS and as a result the use of HOM couplers is not required. This is a significant break from normal practice [14] but results in reduced costs and removes problems with multipacting often present in HOM couplers.

The ability to include angular errors to the cavities, magnet and cryomodule

offset errors are modules that have been added to the "HOMDynamics" code written by Ainsworth [52]. The most significant of these being the angular cavity errors which can significantly degrade the beam particularly at lower beam energies. The addition of magnet errors to the code allows for comparisons to the result from traditional beam optics codes, however due to the use of linear transfer maps non-linear effects are not considered.

In the transverse plane it was found that HOMs play an almost negligible role in reducing the beam quality. However magnet errors and the angular orientation of the cavities can have a significant effect. This study indicated that angular alignments of better than 1 mrad are required to keep the maximum potential growth below 100% and magnet positional errors of less than 1 mm are required to achieve the same level of beam quality.

For resonantly excited HOMs, limits on the R/Q and Q have been found for each cavity allowing for regions of low impact to be identified and for any changes in cavity design to be quickly analysed without re-performing most of the study. As the cavity design has effectively been made redundant in this study which means that insight into the effects of various Q's and R/Q's on beams of low velocity regardless of the cavity design can be found. In particular that as the beam gains energy it becomes less sensitive to lower R/Q modes and therefore resonantly driven HOMs at higher beam velocities with low R/Q are of less concern. This is informative as it gives a rough target for the R/Q of HOMs near harmonics of the bunch frequency in future machines which may use long pulses of protons such as Project-X [32] and MYRRHA [25].

Further, statistical analysis of the phenomena has been performed and it was found that the results are consistent with previous studies [85]. The number of simulations resulting in degradation is in line with what is expected when modes

lie within kHz of the machine harmonics. This result can be readily extended to other cavities with HOMs of similar frequency, Q and R/Q which suggests many superconducting proton linacs with cavity frequencies of 700 MHz or lower are unlikely to require HOM dampers of any kind as long as the HOM frequencies lie within less than 1 MHz or so of harmonics of the machines bunch frequency. In addition it has been shown that it is possible to reduce the ESS limit of 5 MHz on HOM frequencies to value of the order kHz. However when the effects of tuning the cavity on the frequency of the HOM, a greater margin must be given. An appropriate tolerance could $\approx$ 100 kHz at the full extent of the cavity tuning range which in the medium-β cavities is $\sim$2.4 MHz including the shifts expected from simulations by E. Cenni [132].

The findings of this study also indicate as has been suggested in previous work [51, 52] that the use of HOM couplers in high power proton linacs with low frequency cavities is not essential as previously thought. Further it has also provided strong data which indicates the risk from resonantly driven HOMs is in the worst case—where a HOM in the original design lies on a harmonic of the bunch frequency— is low and for ESS in particular is at around the 2% level. This results from a combination of low frequency cavities giving rise to small R/Q's and the high Q of SCRF cavities which being common to many proposed designs of proton linacs makes the results have wider applications than just to the ESS linac.

In addition to this there is also evidence that the transverse alignment of low frequency SCRF cavities is of little importance in high intensity proton linacs as the R/Q of the transverse modes makes the transverse wakefield very small (see table 5.12) compared to other mechanisms of transverse degradation.

Chapter 8

Conclusions

In order to achieve the 5 MW of average beam power that ESS is targeting; the 2 GeV beam energy, 62.5 mA beam current and 2.86 ms pulse length must all be achieved. This requires that all of the ESS cavities are operating in an efficient manner and that there are minimal losses in the accelerator. The ESS has opted to operate without HOM couplers in opposition to the usual convention. This decision was based on previous work [52] which shows the magnitude of beam excited fields at ESS is small, as long as no modes are resonantly driven by the beam. The ESS set a limit on HOM frequencies to prevent such an occurrence, the limit has been set to frequency separation of 5 MHz between all HOMs and harmonics of the bunch frequency in both design and final cavity production. This research has studied the impact of beam excited HOMs on the performance of the ESS, in particular when considering the impact of manufacturing errors on the modal structure of the cavities.

Simulations have been performed in Ansys HFSS to characterise the modal spectrum of each of the current SCRF cavity designs. It was found that the magnitude of the kick factors of the modes within the cavities were of a level consistent with earlier studies using previous cavity design and were therefore

anticipated to have minimal impact on the beam. In addition several modes in the elliptical cavities were identified which lay closest to harmonics of the bunch frequency (352.21 MHz)—one mode in the medium-β cavity at 1749.47 MHz and two in the high-β cavity at 1419.23 and 1419.82 MHz respectively. The mode in the medium-β cavity was determined to be potentially the most harmful as it has highest R/Q and is positioned when the beam is at its most pliable.

In the production of a 146 SCRF cavities geometric errors are inevitable and these—as shown by the high-β prototypes—can result in the frequency of HOMs shifting towards harmonics of the bunch frequency. These errors in the medium-β cavities were investigated through an extensive series of eigenmode simulations performed in Ansys HFSS. The HOM was found to be particularly sensitive to error in the equator ellipse eccentricity A at the 18 MHz/mm level and also in the cell length L at the -7.77 MHz/mm level. Simulations of random errors were then performed using SF where it was shown that the HOMs were considerably more sensitive than the accelerator mode. The results from these simulation were fed into an equivalent circuit model which included cell frequency errors in the form of both capacitive and inductive errors. A series of simulations of including errors of various levels were performed. It was found that for errors below 400 μm the risk of the $\pi/6$ mode shifting within 5 MHz of the 5^{th} harmonic of beam was minimal. Further it was also shown that the modes frequency was most sensitive to errors in the central cells which supports the additional checks and selections of cells performed during the production of the first prototypes [113]. The methods developed in this analysis can readily be applied to other elliptical cavity design and would give good results for cavities with a larger number of cells and higher beam pipe cut-off frequencies.

In an attempt to reduce the chances of the HOM frequency in the high-β

cavities shifting the end-cells were redesigned to increase the HOM separation by 7.59 MHz. This came at a cost of small increases to the peak surface field and a reduction in R/Q. However it also lead to an increase in the geometric factor by 15% which results in an increase in the Q_0 of the cavity by the same amount and consequently could lead to a reduced cryogenic load or possibly increased cavity gradients. As the modifications to the geometry are only to the end half-cell and the overall length and radius of the cavity are maintained the design is plug compatible with the current ESS base line. This goes as far as to include the coupler which can be placed in the same position with its penetration depth increased by 1.85 mm. The result is a design which has many advantages with a handful of very small drawbacks that are far outweighed by the benefits.

In all previous studies it has been assumed that the wakefield in a $v \neq c$ cavity is the same as a $v = c$ cavity without discussion. This has been shown mathematically by Bane [116] to be true in the long range once the exciting charge has exited the cavity. However at ESS and other proton linacs the bunch separation is less than the cavity length meaning that assuming the wakefield is the same may not be strictly true. The mathematical result obtained by Bane was demonstrated in the long range by simulating a pillbox cavity in CST and comparing the results with an analytical modal summation method detailed by Weiland [123], modified to include a bunch of $v < c$. The agreement in the long range was very good however, differences were found in the short range wakefield as expected. Due to the sign of the field from CST this was assumed to be dominated by static fields from the bunch, this was demonstrated by integrating the wakefield off-axis. The off-axis wakefield was shown to be consistent with the analytic prediction except with an apparent time delay in the short range. This delay is likely a result of causality being obeyed in the simulations as it is present

in all simulations regardless of the beam velocity and the delay increases with the offset of the integration axis.

The ESS cavities were then simulated using CST MWS and it was found that the modal summation was applicable in the long range for each of the cavities. However differences were again found in the short range due to the exciting charge, this though is not a concern as it is in a region far closer to the exciting bunch than is possible in the ESS. The most important result from this is that within the minimum separation of the ESS bunches (1/352.21 μs) the wakefield behaves consistent with the modal summation method which is used in the beam dynamics simulations. This analysis represents a confirmation that HOMs and the wakefield may indeed be treated in the same fashion as if the beam was ultra-relativistic in the case of cavities with accelerating frequencies of 352.21 MHz and 704.42 MHz. In addition this means that there is strong evidence that in most proton linacs which tend to use low frequency cavities that the ultra-relativistic form of the wakefield can be used without any corrections needing to be applied due to the lower beam velocity when conventional RF bucket spacings are used. To test this experimentally a setup with two proton bunches of variable separation and highly accurate bunch energy resolution would be required.

Beam dynamics simulations have been performed using the python code "HOM-Dynamics" [52] with several modifications to allow different error sources to be routinely applied. It was shown that passband modes are not a concern in the case where $Q_{ex} < 2 \times 10^6$. This is higher than the Q_{ex} of the accelerating mode with which the Q_{ex} of the modes is expected to be comparable. It was also shown that both longitudinal and transverse HOMs are of little concern at ESS except in the case where a longitudinal HOM is resonantly driven and is consistent with previous studies [51, 85]. The results in the transverse plane included the presense

of transverse and angular cavity errors as well as magnet misalignment errors. It was found that the transverse plane was insensitive to HOM effects resulting from cavity or cryomodule misalignments. However, the beam was sensitive to angular alignments issues which result in a transverse kick from the accelerating mode, with angular errors of order 1.5 mrad capable causing the transverse distribution to double in size.

The case where a HOM lay close to a harmonic of the bunch frequency was paid particular attention. It was found that the position of a cavity within the linac which contained a mode on a harmonic of the bunch frequency is extremely important due to the varying values of the modes R/Q from cavity-to-cavity. This means that there are regions where bad cavities may be placed and have no/little impact on the beam, this naturally leads to the idea of sorting cavities by this feature. However, while theoretically possible, it is impractical in the construction schedule at ESS as it requires all or a significant number of cavities to be ready simultaneously. Further to this, detailed simulation to determine the damping levels required to mitigate the impact of resonantly driven HOMs were performed and it was found Q_{ex}'s of below 3×10^5 and 9×10^5 were sufficient to mitigate the effects of the HOMs in the high and medium-β cavities respectively. In addition simulations to determine limits in terms of R/Q on each cavity were performed, this allows a quick check to be carried out if the cavity designs are changed without repeating the study in its entirety. The results of these studies can be used as a baseline for the analysis of other long pulse machines with bunch frequencies similar to the ESS machine as for much of the study the cavity design itself is irrelevant only the beam velocity is crucial.

Through the simulation of the linac with random frequency errors on the HOM frequencies it was shown that the ESS limit of 5 MHz is sufficient to mitigate the

impact of HOMs on the beam. However, by performing a detailed statistical analysis of the data it was found that the number of significant events that were present are consistent with linacs containing modes within kHz of the machine harmonic rather than MHz. This was found through the use of cumulative distribution functions taking into account the number of cavities in each section of the linac which may impact on the beam. To allow this to be performed a large sample of 10,000 simulations was required to obtain a significant level of confidence. This result was confirmed by shifting the frequency of a HOM in each cavity individually away from the machine harmonic whilst having no HOMs present in the other cavities. The frequency at which the effect was below that due to RF errors was noted and in each case was below 10 kHz. This is strong evidence that in high power proton linacs HOM couplers are not required as long as careful consideration is given to the cavity design with regards to HOM frequencies.

This result is a strong indication that the frequency limit set by ESS of a separation greater than 5 MHz could be reduced by several orders of magnitude without impacting the beam. However due to frequency shifts possible during operation a significantly larger limit is required. One worst case scenario would be that the cavity is tuned onto the machine harmonic during operation. For the medium-β cavity the tuning sensitivity of the $\pi/6$ mode in the 3^{rd} band is 800 kHz/mm compared to the accelerating mode at 200 kHz/mm, with a maximum tuning distance of ± 3 mm. Therefore the final limit found should be set relative to the full extent of the tuning range of the HOM which for the medium-β cavity is ≈ 2.4 MHz.

The work in this thesis gives a detailed study of the effects of beam-excited HOMs on the performance of the ESS linac,he work in this thesis gives a detailed study of the e ects of beam-excited HOMs on the performance of the ESS linac,

the results of which can readily be extended to linear colliders [64] and other machines such as Project-X and MYRRHA. In particular the conclusion that HOM couplers are non-essential and may even result in reduced performance as originally was the case at SNS. There is strong evidence that the high Q_L of the HOMs is beneficial to performance as it results in a very narrow frequency range at which a HOM may be dangerous to the machine. As such if great care is taken in the design to ensure HOMs lie 1–2 MHz away from harmonics of the bunch frequency the risk from the HOMs becomes negligible even when shifts due to active tuning are taken into account.

Ensuring this frequency separation occurs means that the behaviour of the resonant frequencies when manufacturing errors are present must be understood in detail. In this thesis a method of using single cell eigenmode simulations in conjunction with an equivalent circuit model was presented that can be extended to any traditional TM resonator. This study suggested that for the 200 μm maximum errors anticipated that there is almost no risk of a cavity frequencies shifting towards harmonics of the bunch frequency by an amount that would cause concern.

The results in this thesis rely heavily on the fact that the behaviour of the wakefield is understood correctly at the arrival of the next trailing bunch. This meant that a detailed study into the behaviour of the wakefield in low-β structures was needed. This study showed that for structures with similar bunch separations and cavity frequencies that the modal summation method applied in many codes is still valid. The results of this can readily be applied to both higher frequency proton linacs and electron guns where the effects may be more significant and potentially inhibit the performance of the machines in terms of minimising the beam emittance.

Bibliography

[1] CERN Editorial Board. LHC Design Report, 2004.

[2] European Organization for Nuclear Research (CERN). http://home.web.cern.ch/, 2015.

[3] ISIS Homepage. http://www.isis.stfc.ac.uk/, 2015.

[4] S-H. Kim et al. The Status Of The Superconducting Linac And SRF Activities At The SNS. In *Proceedings of SRF2013, Paris, France*, 2013.

[5] J.J. Thompson. Cathode rays. *Philosophical Magazine*, 44, 1897.

[6] J.D. Cockcroft and E.T.S. Walton. Experiments with high velocity positive ions II. The Disinitigration of Elements by High Velocity Protons. *Proceedings of the Royal Society A*, 136:229–242, 1932.

[7] G. Ising. Prinzip einer methode zur herstellung von kanalstrahlen hoher voltzahl. *Ark. Mat. Astron. Fys.*, 18(30):1–4, 1924.

[8] R. Wideröe. ber ein neues prinzip zur herstellung hoher spannungen. *Archiv fr Elektrotechnik*, 21(4):387–406, 1928.

[9] J.D. Jackson. *Classical Electrodynamics*. Wiley, 3rd edition, 1998.

[10] K. Wille. *The Physics of Particle Acceerators an Introduction*. Oxford, 2000.

[11] T.P. Wangler. *RF Linear Accelerators*. Wiley-VCH, 2nd edition.

[12] A.W. Chao et al., editors. *Handbook of Accelerator Physics and Engineering*. 2nd edition, 2012.

[13] F. Gerigk. Cavity Types, CERN-2011-007. In *CAS CERN Accelerator School, RF for Accelerators, Ebeltoft, Denmark*, 2011.

[14] H. Padamsee, J. Knoloch, and T. Hays. *RF Superconductivity for Accelerators*. Wiley-VCH, 2nd edition, 2008.

[15] H. Podlech. Superconducting Versus Normal Conducting Cavities, CERN-2013-001. In *CAS CERN Accelerator School, High Power Hadron Machines, Bilbao, Spain*, 2011.

[16] B. Aune et al. Superconducting TESLA Cavities. *Phys. Rev. ST Accel. Beams*, 3:092001, Sep 2000.

[17] The TLEP Design Study Working Group. First look at the physics case of TLEP. *Journal of High Energy Physics*, 2014(1):1–49, 2014.

[18] J. Carwardine et al. International Linear Collider (ILC) Technical Design Report, 2013.

[19] E. Saldin, E.A. Schneidmiller, and M.V. Yurkov. *The Physics of Free Electron Lasers*. Advanced Texts in Physics. Springer, 2000.

[20] The TESLA Test Facility FEL Team. SASE FEL at the TESLA Facility, 2002.

[21] M. Altarelli et al. The European X-Ray Free-Electron Laser Technical Design Report, 2007.

[22] LCLS-II Project Team. Linear Coherent Light Source II, Final Design Report, 2014.

[23] M. Vretenar. Low-Beta Structures, CERN-2011-007. In *CAS CERN Accelerator School, RF for Accelerators, Ebeltoft, Denmark*, 2011.

[24] D. Vandeplassche and L. Medeiros Romao. Accelerator Driven Systems. In *Proceedings of IPAC2012, New Orleans, Louisiana, USA*, 2012.

[25] H. Ait Abderrahim et al. MYRRHA: A Multipurpose Accelerator Driven System for Research and Development . *Nuclear Instruments and Methods in Physics Research Section A: Accelerators, Spectrometers, Detectors and Associated Equipment*, 463(3):487 – 494, 2001.

[26] T. Nilsson. European RIB Facilities: Status and Future. *Nuclear Instruments and Methods in Physics Research Section B: Beam Interactions with Materials and Atoms*, 317, Part B:194 – 200, 2013.

[27] The Facility for Rare Isotope Beams (FRIB). http://www.frib.msu.edu/, 2015.

[28] R. Catherall et al. An overview of the HIE-ISOLDE Design Study. *Nuclear Instruments and Methods in Physics Research Section B: Beam Interactions with Materials and Atoms*, 317, Part B:204 – 207, 2013.

[29] K. Abe et al. Evidence of Electron Neutrino Appearance in a Muon Neutrino Beam.

[30] ND280 collaboration. T2K Technical Design Report, 2006.

[31] F. Gerigk et al. *Conceptual Design of the Low-Power and High-Power SPL: A Superconducting H^- Linac at CERN*. CERN, 2014.

[32] R. Tschirhart. Project-X: A New High Intensity Proton Accelerator Complex at Fermilab . In *Proceedings of DPF-2011, Providence, RI*, 2011.

[33] G.L. Squires. *Introduction to the Theory of Thermal Neutron Scattering*. Cambridge University Press, 2012.

[34] K. Sköld and D.L. Price. *Neutron Scattering*. Experimental Methods In The Physical Sciences. Academic Press, 1986.

[35] ILL Homepage. http://www.ill.eu/, 2015.

[36] S. Peggs et al. ESS Technical Design Report, 2013.

[37] H. Danared. Design of the ESS Accelerator. In *Proceedings of IPAC 2012, New Orleans, LA, USA*, 2012.

[38] M. Eshraqi. Beam Physics Design of the Optimus+ SC Linac. Technical Report November 2013, ESS, Lund, Sweden, 2013.

[39] D. Filges and F. Goldenbaum. *Handbook of Spallation Research*. Wiley, 2010. ISBN 9783527628872.

[40] J. Fitter, T. Gutberlet, and J. Katsaras. *Neutron Scattering in Biology: Techniques and Applications*. Biological and Medical Physics Series. Springer, 2006.

[41] J.M. Carpenter and C.K. Loong. *Elements of Slow-Neutron Scattering*. Cambridge University Press, 2015.

[42] L. Neri et al. Improved Design of Proton Source and Low Energy Beam Transport Line for European Spallation Source. *Review of Scientific Instruments*, 85(2), 2014.

[43] O. Piquet et al. RF Design of ESS RFQ. In *Proceedings of IPAC 2012, New Orleans, LA, USA*, 2012.

[44] R. Miyamoto et al. Beam Physics Design of the ESS Medium Energy Beam Transport. In *Proceedings of IPAC 2014, Dresden, Germany*, 2014.

[45] R. De Prisco et al. ESS DTL Status: Redesign and Optimusation. In *Proceedings of IPAC 2014, Dresden, Germany*, 2014.

[46] P. Duchesne et al. Design Of The 352 MHz, Beta 0.50, Double Spoke Cavity For ESS. In *Proceedings of SRF2013, Paris, France*, 2013.

[47] G. Devanz et al. ESS Elliptical Cavities And Cryomodules. In *Proceedings of SRF2013, Paris, France*, pages 1218–1222, 2013.

[48] C. Darve et al. The ESS Superconducting Linear Accelerator ESS Accelerator Requirements Optimization of SRF Linac Risk Assessment and Sustainable Infrastructure. In *Proceedings of SRF2013, Paris, France*, pages 77–79, 2013.

[49] *Nuclear Instruments and Methods in Physics Research, Section A: Accelerators, Spectrometers, Detectors and Associated Equipment*.

[50] D. Jeon et al. Cumulative beam break-up study of the spallation neutron source superconducting linac. *Nuclear Instruments and Methods in Physics Research Section A: Accelerators, Spectrometers, Detectors and Associated Equipment*, 495(2):85 – 94, 2002.

[51] M. Schuh. *Study of Higher Order Modes in Superconducting Accelerating Structures for Linac Applications*. PhD thesis, Ruperto-Carola University of Heidelberg, 2011.

[52] R. Ainsworth. *Parasitic Resonances in High Power Proton Linacs: Major Issues and Mitigation Techniques*. PhD thesis, Royal Holloway, 2014.

[53] S. Kim. SNS Superconducting LINAC Operational Experience And Upgrade Path. In *Proceedings of LINAC 2008, Victoria, BC, Canada*, 2008.

[54] J.C. Maxwell. A Dynamical Theory of the Electromagnetic Field. *Phil. Trans. R. Soc.*, 155:459–512, Jan 1865.

[55] D.M. Pozar. *Microwave Engineering*. John Wiley and Sons, 4th edition, 2012.

[56] N. Marcuvitz and Institution of Electrical Engineers. *Waveguide Handbook*. IEE electromagnetic waves series. P. Peregrinus, 1951.

[57] A.H.-D. Cheng and D.T. Cheng. Heritage and early history of the boundary element method. *Engineering Analysis with Boundary Elements*, 29(3):268 – 302, 2005.

[58] S.Y. Lee. *Accelerator Physics*. World Scientific, 2nd edition, 2004.

[59] H. Wiedemann. *Particle Accelerator Physics*. Graduate Texts in Physics. Springer International Publishing, 2015.

[60] K.L.F. Bane, P.B. Wilson, and T. Weiland. Wake Fields And Wake Field Acceleration. In *3rd Summer School on High Energy Particle Accelerators, Upton, New York,.*, 1983.

[61] C.G. Someda. *Electromagnetic Waves, 2nd Edition*. CRC Press, 2006.

[62] J.F. Annett. *Superconductivity, Superfluids and Condensates*. Oxford Master Series in Physics. OUP Oxford, 2004.

[63] W.K.H. Panofsky and W.A. Wenzel. Some considerations concerning the transverse deflection of charged particles in radio-frequency fields. *Review of Scientific Instruments*, 27(11):967, 1956.

[64] R.M. Jones. Wakefield suppression in high gradient linacs for lepton linear colliders. *Phys. Rev. ST Accel. Beams*, 12:104801, 2009.

[65] R.H. Miller. Comparison of Standing Wave and Travelling Wave Structures. In *Proceedings of Linac 1986*, 1986.

[66] V.A. Moiseev, V.V. Paramonov, and K. Floettmann. Comparison of Standing and Travelling Wave Operations for Positron Pre-Accelerator in the TESLA Linear Collider. In *Proceedings of EPAC 2000*, 2000.

[67] J. Bardeen, L.N. Cooper, and J.R. Schrieffer. Theory of superconductivity. *Phys. Rev.*, 108:1175–1204, Dec 1957.

[68] J Bardeen. Two-fluid model of superconductivity. *Phys. Rev. Lett.*, 1: 399–400, Dec 1958.

[69] H. Padamsee. *RF Superconductivity: Volume II: Science, Technology and Applications*. Wiley series in beam physics and accelerator technology. Wiley, 2009.

[70] M. Aicheler et al. A Multi-TeV Linear Collider based on CLIC Technology: CLIC Conceptual Design Report, 2012.

[71] A.A. Abrikosov. The Magnetic Properties of Superconducting Alloys. *Journal of Physics and Chemistry of Solids*, 2(3):199 – 208, 1957.

[72] P. Schumüser. Basic Principles of RF Superconductivity and Superconducting Cavities. In *Proceedings of the 11th Workshop on RF Superconductivity, Lbeck/Travemünder, Germany*, 2003.

[73] R.L. Geng. Review of New Shapes for Higher Gradients . *Physica C: Superconductivity*, 441(12):145 – 150, 2006.

[74] D. Reschke. Results on Large Grain Nine-Cell Cavities at DESY: Gradients up to 45 MV/m After Electropolishing. In *Proceedings of SRF 2011, Chicago, IL, USA*, 2011.

[75] J.K. Sekutowicz. Superconducting Elliptical Cavities, CERN-2011-007. In *CAS CERN Accelerator School, RF for Accelerators, Ebeltoft, Denmark*, 2011.

[76] N. Juntong. *Investiagtion Of Optimised Electromagnetic Fields In SRF Cavities For The ILC*. PhD thesis, University of Manchester, 2011.

[77] J.R. Delayen. Superconducting Accelerating Structures For High-Current Ion Beams. In *Proceedings of the 1988 Linear Accelerator Conference, Williamsburg, Virginia, USA.*, 1988.

[78] CST Microwave Studio. https://www.cst.com/Products/CSTMWS.

[79] D. Alesini. Power Coupling, CERN-2011-007. In *CAS CERN Accelerator School, RF for accelerators, Ebeltoft, Denmark*, 2011.

[80] R. M. Jones, C. E. Adolphsen, J. W. Wang, and Z. Li. Wakefield damping in a pair of x-band accelerators for linear colliders. *Phys. Rev. ST Accel. Beams*, 9:102001, Oct 2006.

[81] E. Rampnoux et al. Design Of 352.21 MHz Power Coupler and Window For The European Spallation Source Project (ESS). In *Proceedings of SRF2013, Paris, France*, 2012.

[82] K. Koepke. Design of power and hom couplers for tesla. In Peter Kittel, editor, *Advances in Cryogenic Engineering*, volume 41 of *A Cryogenic Engineering Conference Publication*, pages 877–884. Springer US, 1996. ISBN 978-1-4613-8022-1.

[83] A. Valez et al. BESSY VSR: A Novel Application of SRF For Synchrotron Light Sources. In *Proceedings of SRF 2015, Whistler, BC, Canada*, 2015.

[84] A.W. Chao and W. Chou. *Reviews of Accelerator Science and Technology: Volume 5: Applications of Superconducting Technology to Accelerators*. World Scientific Publishing Company, 2013.

[85] R. Ainsworth and S. Molloy. The influence of parasitic modes on beam dynamics for the European spallation source linac. *Nuclear Instruments and Methods in Physics Research, Section A: Accelerators, Spectrometers, Detectors and Associated Equipment*, 734:95–100, 2014.

[86] M. Liepe, W.D. Moeller, and S.N. Simrock. Dynamic Lorentz Force Compensation with a Fast Piezoelectric Tuner. In *Proceedings of PAC2001, Chicago, IL, USA.*, 2001.

[87] G. Devanz et al. Compensation of Lorentz Force Detuning of a TTF 9-Cell Cavity With a New Integrated Piezo Tuner. In *Proceedings of EPAC2006, Edinburgh, UK.*, 2006.

[88] S.N. Simrock. Lorentz Force Compensation of Pulsed SRF Cavities. In *Proceedings of LINAC 2002, Gyeongju, Korea*, 2002.

[89] R. Mitchell et al. Lorentz Force Detuning Analysis of the Spallation Neutron Source Accelerating Cavities. In *The 10th Workshop on RF Superconductivity, Tsukuba, Japan*, 2001.

[90] G. Devanz et al. High Power Pulsed Tests of a Beta=0.5 5-cell 704 MHz Superconducting Cavity. In *Proceedings of SRF 2011, Chicago, IL, USA*, 2011.

[91] A.W. Chao. *Physics of Collective Beam Instabilities in High Energy Accelerators*. Wiley Series in Beam Physics and Accelerator Technology. Wiley, 1993.

[92] J. Forshaw and G. Smith. *Dynamics and Relativity*. Manchester Physics Series. Wiley, 2014.

[93] I.S. Grant and W.R. Phillips. *Electromagnetism*. Manchester Physics Series. Wiley, 2nd edition, 2013.

[94] G.V. Stupakov. Wake and Impedence. In *Lecture presented at JAS'2000 Accelerator School On Frontiers Of Accelerator Technology: High Quality Beams, Moscow, Russia*, 2000.

[95] W.Z. Bruno and S.A. Kheifets. *Impedances and Wakes in High-energy Particle Accelerators*. World Scientific, 1998.

[96] L. Palumbo, V.G. Vaccaro, and M. Zobov. Wake Fields and Impedance, LNF-94-041-P1. In *CAS CERN Accelerator School: 5th Advanced Accelerator Physics Course, Rhodes, Greece*, 1993.

[97] P.B. Wilson. Transient Beam Loading in Electron-Positron Storage Rings, CERN-ISR-TH/78-23, 1978.

[98] E.U. Condon. Forced oscillations in cavity resonators. *Journal of Applied Physics*, 12(2):129–132, 1941.

[99] K.F. Riley, M.P. Hobson, and S.J. Bence. *Mathematical Methods for Physics and Engineering: A Comprehensive Guide*. Cambridge University Press, 3rd edition, 2006.

[100] P.B. Wilson. Introduction to Wake Fields and Wake Potentials. *AIP Conf. Proc.*, 184:525–564, 1989.

[101] B. W. Zotter and S. A. Kheifets. *Impedances and Wakes in High-Energy Particle Accelerators*. World Scientific, 1998.

[102] D.E. Nagle, E.A. Knapp, and B.C. Knapp. Coupled resonator model for standing wave accelerator tanks. *Review of Scientific Instruments*, 38(11): 1583–1587, 1967.

[103] R.L. Gluckstern and K.L.F. Bane. The Transverse Wakefield of a Detuned X-Band Accelerator Structure. *Science*, 42(March):123–169, 1993.

[104] A. Bondeson, T. Rylander, and P. Ingelström. *Computational Electromagnetics*. Texts in Applied Mathematics. Springer New York, 2005.

[105] V. Thomée. From finite differences to finite elements. *Journal of Computational and Applied Mathematics*, 128(1-2):1–54, 2001.

[106] R. Courant. Variational methods for the solution of problems of equilibrium and vibrations. *Bull. Amer. Math. Soc.*, 49:1–23, 1943.

[107] K. Halbach and R. Holsinger. SUPERFISH-a computer program for evaluation of RF cavities with cylindrical symmetry. *Particle Accelerators*, 7(4): 213–222, 1976. URL http://cdsweb.cern.ch/record/700607.

[108] Ansys HFSS. http://www.ansys.com/.

[109] W. Bruns. GdfidL: A Finite Difference Program With Reduced Memory and CPU Usage. In *Proceedings of PAC1997, Vancouver, B.C., Canada.*, 1997.

[110] M. Eshraqi. Private comunication, .

[111] A. Farricker, R.M. Jones, and S. Molloy. ICFA mini Workshop on High Order Modes in Superconducting Cavities, HOMSC14 Beam Dynamics in the ESS Linac under the Influence of Monopole and Dipole HOMs. *Physics Procedia*, 79:21 – 29, 2015.

[112] G. Olry. Recent Progress of ESS Spoke and Elliptical Cryomodules. In *Proceedings of SRF2015, Whistler, Canada*, 2015.

[113] E. Cenni et al. ESS Medium Beta Cavity Prototypes and Manufacturing. In *Proceedings of SRF2015, Whistler, Canada*, 2015.

[114] F. Peauger et al. Progress in the Elliptical Cavities and Cryomodule Demonstarors for the ESS Linac. In *Proceedings of SRF2015, Whistler, Canada*, 2015.

[115] F. Peauger et al. Status and First Test Results of Two High Beta Prototype Eliptical Cavities For ESS. In *Proceedings of IPAC2014, Dresden, Germany*, pages 2477–1479, 2014.

Bibliography

[116] K. Bane. Constructing the Wake Potentials From the Empty Cavity Solutions to Maxwell's Equations, CERN/ISR-TH/80-47. 1980.

[117] I.E. Campisi et al. Superconducting Cavity Development for the CEBAF Upgrade. In *Proceedings of PAC 1999, New York, USA*, 1999.

[118] P. Balleyguier. A straightforward method for cavity external Q computation. *Particle Accelerators*, 57(2):113–128, 1997.

[119] P. Balleyguier. External Q Studies for APT SC-Cavity Couplers. In *Proceedings of LINAC 1998, Chicago, IL, USA*, 1998.

[120] C. Arcambal. Private comunication.

[121] J.C. Slater. Microwave electronics. *Reviews of Modern Physics*, 18(4):441–512, 1946.

[122] P.M. Lapostolle and A.L. Septier, editors. *Linear Accelerators*. 1970.

[123] T. Weiland and B. Zotter. Wakefield of a Relativistic Current in a Cavity, CERN/ISR-TH/80-36. 1980.

[124] D. Uriot and N. Pichoff. Status of TraceWin Code. In *Proceedings of IPAC 2015, Richmond, VA, USA*, 2015.

[125] M. Reiser. *Theory and Design of Charged Particle Beams*. Wiley Series in Beam Physics and Accelerator Technology. Wiley, 2008.

[126] M. Eshraqi. Private comunication, .

[127] M. Schuh et al. Influence of higher order modes on the beam stability in the high power superconducting proton linac. *Physical Review Special Topics - Accelerators and Beams*, 14(5):1–23, 2011.

[128] D. Thain, T. Tannenbaum, and M. Livny. Distributed Computing in Practice: The Condor Experience. *Concurrency - Practice and Experience*, 17 (2-4):323–356, 2005.

[129] S. Molloy. An Empirical Study of HOM Frequencies, 2011.

[130] M. Matsumoto and T. Nishimura. Mersenne Twister: A 623-Dimensionally Equidistributed Uniform Pseudo-Random Number Generator. *ACM Transactions on Modeling and Computer Simulation (TOMACS)*, 8(1):3–30, 1998.

[131] A. Johansson et al. LLRF System For The ESS Proton Accelerator. In *Proceedings of IPAC 2014, Dresden, Germany*, 2014.

[132] E. Cenni. Private comunication.

Appendix A

Fundamental Theorem of Beam Loading

Consider a point charge moving on axis through a cylindrically symmetric cavity, as it is on axis it may only excite monopole modes as all other modes have zero on axis longitudinal electric fields. This charge will excite the monopole modes resulting in a beam induced voltage and it will also induce surface currents in the cavity walls. If we consider two particles of equal charge q, and kinetic energy T, that are separated by half a wavelength of the cavity mode. The first charge travels through unexcited cavity where it generates a voltage

$$V_c = -V_{bq}. \tag{A.1}$$

The induced voltage seen by the first charge is some fraction f, of the induced voltage which acts back on the charge producing the voltage,

$$V_q = fV_{bq}. \tag{A.2}$$

The energy lost by the first charge is,

$$\Delta W_1 = -qfV_{qb}. \tag{A.3}$$

We define the energy stored in the induced field to be

$$U = \alpha V_{bq}^2, \tag{A.4}$$

where α is a constant of proportionality. From the conservation of energy we conclude

$$U = \alpha V_{bq}^2 = -W_1 = qfV_{bq}, \tag{A.5}$$

hence

$$V_{bq} = \frac{qf}{\alpha}. \tag{A.6}$$

This implies that the induced voltage is proportional to the charge that caused the excitation. The second charge then enters the cavity half a wavelength later when the voltage induced by the first charge has changed phase by π radians, and is now positive. The charge induced by this second charge will be negative and of equal magnitude, therefore the total voltage in the cavity is $V_c = V_{bq} - V_{bq} = 0$ when the second charge has left the cavity, this also makes the energy stored in the cavity zero. The energy change for the second charge is,

$$\Delta W_1 = -qfV_{bq} + qV_{bq} = qV_b(1 - f). \tag{A.7}$$

Due to the charges being identical and the cavity lossless, through energy conservation it is found that

$$\Delta W_1 + \Delta W_2 = -qfV_{bq} - qfV_{bq} + qV_{bq} = qV_b(1 - 2f) = 0, \tag{A.8}$$

this implies that $f = \frac{1}{2}$ and that the voltage seen by the first charge is equal to half of the induced voltage left in the cavity. The final result is that

$$V_q = \frac{V_b}{2} \tag{A.9}$$

and this resulting equation is known as the fundamental theorem of beam loading.

Appendix B

The Condon Method

B.1 Mode Expansion of Fields in a Cavity

The electric field $\vec{E}(\vec{r},t)$ and the magnetic field $\vec{B}(\vec{r},t)$ can be written in terms of the vector potential $\vec{A}(\vec{r},t)$ and the scalar potential $\Phi(\vec{r},t)$ as;

$$\vec{B} = \nabla \times \vec{A} \tag{B.1}$$

$$\vec{E} = -\frac{\partial \vec{A}}{\partial t} - \nabla\Phi \tag{B.2}$$

In the coulomb gauge ($\nabla.\vec{A} = 0$) The wave equation from Maxwell's equations becomes

$$\nabla^2\vec{A} - \frac{1}{c^2}\frac{\partial^2\vec{A}}{\partial t^2} - \frac{1}{c^2}\frac{\partial\Phi}{\partial t} = -\mu_0\vec{j}. \tag{B.3}$$

Restricting ourselves to be within the perfectly conducting walls of the cavity, the vector potential can be expanded as a set of orthonormal functions, $\vec{a}_\lambda$ as

$$\vec{A}(\vec{r},t) = \sum_\lambda q_\lambda(t)\vec{a}_\lambda(\vec{r}) \tag{B.4}$$

where

$$\nabla^2\vec{a}_\lambda + \frac{\omega_\lambda^2}{c^2}\vec{a}_\lambda = 0 \tag{B.5}$$

with boundary conditions $\nabla.\vec{a}_\lambda = 0$ and $\vec{a}_\lambda \times \hat{n} = 0$ on the metallic surface of the cavity. Similarly with the scalar potential,

$$\Phi(\vec{r},t) = \sum_\lambda r_\lambda(t)\phi_\lambda(\vec{r}) \tag{B.6}$$

where

$$\nabla^2\Phi_\lambda + \frac{\Omega_\lambda^2}{c^2}\Phi_\lambda = 0 \tag{B.7}$$

with $\phi_\lambda = 0$ on the metallic surface. Substituting equations B.4 and B.6 into equation B.3 we get

$$\sum_\lambda \left[(\ddot{q}_\lambda + \omega_\lambda^2 q_\lambda)\vec{a}_\lambda + \dot{r}_\lambda\nabla\phi_\lambda\right] = \mu_0\dot{\vec{j}}c^2 \tag{B.8}$$

Integrating equation B.8 over the volume of the cavity, V and normalising $\vec{a}_\lambda$ as

$$\frac{\epsilon_0}{2}\int_V \vec{a}_{\lambda'}.\vec{a}_\lambda dV = U\delta_{\lambda\lambda'} \tag{B.9}$$

here $\delta_{\lambda\lambda'}$ is a Kronecker delta function, the integral becomes

$$\ddot{q}_\lambda + \omega_\lambda^2 q_\lambda = \frac{1}{2U_\lambda}\int_V \vec{j}.\vec{a}_\lambda dV. \tag{B.10}$$

Hence with no current q_λ will oscillate sinusoidally with frequency ω_λ allowing the vector potential to be written as,

$$\vec{A}(\vec{r},t) = \sum_\lambda C_\lambda\vec{a}_\lambda\cos(\omega_\lambda t + \theta_\lambda) \tag{B.11}$$

where C_λ and θ_λ are constants depending on the cavity. Similarly if we start with Gauss' law,

$$\nabla.\vec{E} = \frac{\rho}{\epsilon_0} \tag{B.12}$$

the resulting equation is

$$r_\lambda = \frac{1}{2T_\lambda}\int_V \rho\phi_\lambda dV, \tag{B.13}$$

where ϕ_λ is normalised by

$$\frac{\epsilon_0}{2}\int_V \nabla\phi_{\lambda'}.\nabla\phi_\lambda dV = T_\lambda\delta_{\lambda\lambda'}. \tag{B.14}$$

Whenever there are no charges in the cavity all r_λ are zero. Thus, given the homogeneous solutions $\vec{a}_\lambda$, ϕ_λ and the sources $\vec{j}$, ρ the equations can be solved for the q_λ, r_λ from equations B.10 and B.13. These in turn allow the electric and magnetic fields to be found. The electric field is given by,

$$\vec{E} = -\sum_\lambda(\dot{q}_\lambda\vec{a}_\lambda + r_\lambda\nabla\phi_\lambda) \tag{B.15}$$

and the magnetic by

$$\vec{B} = \sum_\lambda q_\lambda\nabla\times\vec{a}_\lambda. \tag{B.16}$$

The stored energy is therefore

$$\varepsilon = \frac{1}{2}\int_V(\epsilon_0\vec{E}^2 + \vec{B}^2/\mu_0) = \sum_\lambda(\dot{q}_\lambda^2 U_\lambda + \omega_\lambda^2 q_\lambda^2 U_\lambda + r_\lambda^2 T_\lambda). \tag{B.17}$$

B.2 The Longitudinal Wakefield

The longitudinal wakefield W_z can be calculated using,

$$W_z(s) = -\frac{1}{Q}\int_0^L dz E_z(z,(z+s)/c). \tag{B.18}$$

The charge density $\rho(x,t)$ and current density $j(x,t)$ of the driving charge are given by;

$$\rho(\vec{r},t) = Q\delta(x)\delta(y)\delta(z-ct) \tag{B.19}$$

and

$$\vec{j}(\vec{r},t) = \hat{z}c\rho(\vec{r},t). \tag{B.20}$$

By substituting equation B.6 and B.4 into equation B.10 gives;

$$\ddot{q}_\lambda + \omega_\lambda^2 q_\lambda = \frac{Qc}{2U_\lambda}\begin{cases} 0 & t<0 \\ a_\lambda(0,0,ct) & 0<t<L/c \\ 0 & t>L/c \end{cases} \tag{B.21}$$

As there is no field in the cavity before the driving charge enters, $q(0)=0$ and $\dot{q}(0)=0$ and by varying parameters,

$$q_\lambda(t) = \frac{Qc}{2U_\lambda\omega_\lambda}\int_0^{min(t,L/c)} dt' \sin\omega_\lambda(t-t')a_{\lambda z}(0,0,ct'), \tag{B.22}$$

can be obtained. Similarly by substituting equation B.20 and B.19 into equation B.13,

$$r_\lambda = \frac{Q}{2T_\lambda} \begin{cases} 0 & t < 0 \\ \phi_\lambda(0,0,ct) & 0 < t < L/c \\ 0 & t > L/c \end{cases} \tag{B.23}$$

can be readily found. The fields and the stored energy can then be constructed in terms of the solutions $\vec{a}_\lambda$, ϕ_λ and ω_λ. The energy left in the cavity after the driving charge has left is then found to be,

$$\varepsilon = \sum_\lambda (\dot{q}_\lambda^2 + \omega_\lambda^2 q_\lambda^2) = Q^2 \sum_\lambda \frac{|V_\lambda|}{4U_\lambda} \tag{B.24}$$

where V_λ is defined as;

$$V_\lambda = \int_0^L e^{i\omega_\lambda z/c} a_{\lambda z}(0,0,ct)dz. \tag{B.25}$$

The term which is summed over is known as the modal loss factor an it is defined as,

$$k_\lambda = \frac{|V_\lambda|^2}{4U_\lambda} \tag{B.26}$$

which is the energy per unit charge squared lost to the cavity in each mode. The total loss factor is the sum of the modal loss factors and characterises the total energy lost by a traversing charge. The wake potential in terms of the normal modes can be obtained by substituting the fields into equation B.18 giving;

$$W_z(s) = \frac{1}{Q} \sum_\lambda \int_0^L \left| \dot{q}_\lambda \left(\frac{z+s}{c} \right) a_{\lambda z}(0,0,z) + r_\lambda \left(\frac{z+s}{c} \right) \frac{\partial \phi_\lambda}{\partial z}(0,0,z) \right| \tag{B.27}$$

This can the be solved using equations B.22 and B.23 for the three regimes; when $s > L$, $0 < s < L$ and $s < 0$.

For the case when $s > L$ there are no source terms ($r_\lambda = 0$) and

$$W_z(s) = \sum_\lambda \frac{I_{1\lambda}(s)}{2U_\lambda} \quad s > L \tag{B.28}$$

with

$$I_{1\lambda}(s) = \int_0^L dz \int_0^L dy a_{\lambda z}(z) a_{\lambda z}(y) \cos \frac{\omega - \lambda}{c}(z + s - y) \tag{B.29}$$

equation B.28 can be written as

$$W_z(s) = \sum_\lambda 2k_\lambda \cos \frac{\omega_\lambda s}{c} \quad s > L. \tag{B.30}$$

In the case where $0 < s < L$ the same result is found, however if $s < 0$, $W_z(s) = 0$. Through the fundamental theorem of beam loading the wakefield when $s = 0$ can be found as

$$W_z(0) = \sum_\lambda k_\lambda \cos \frac{\omega_\lambda s}{c} \quad s = 0. \tag{B.31}$$

The result for all three conditions on s can be summarised as:

$$W_z(s) = 2H(s) \sum_n k_\lambda \cos \frac{\omega_n s}{c} \tag{B.32}$$

where,

$$H(s) = \begin{cases} 0 & s < 0 \\ 1/2 & s = 0 \\ 1 & s > 0 \end{cases}. \tag{B.33}$$

This method of decomposing the fields within a cavity into a series of eigenmodes is known as the Condon method and it form the basis of all cavity mode

analysis. This process can be repeated for the transverse wakefield which can be shown to be

$$W_z(s) = 2H(s)\sum_n k_{\perp,\lambda} \sin\frac{\omega_n s}{c}. \tag{B.34}$$

Appendix C

Frequency Scaling of Cavity Parameters

Using Maxwells equations it is possible to show for an alternating field $\vec{E} = E_0 e^{i\omega t}$ with current density $\vec{j} = \sigma\vec{E}$ and for a good conductor ($\omega\epsilon \ll \sigma$);

$$\nabla^2\vec{E} = \tau_n^2\vec{E} \tag{C.1}$$

with $\tau_n = \sqrt{i\omega\sigma\mu}$. Similar equations can be obtained in therms of the magnetic field, $\vec{H}$ and the current density $\vec{j}$. The results from both the electric and magnetic fields are completely consistent with each other this can be show by considering a conducing surface in the x plane assuming the electric field is only in the z direction, with no variation in the x and y planes. The solution for E_z becomes;

$$E_z = E_0 e^{-\tau_n x} \tag{C.2}$$

which can be written as;

$$E_z = E_0 e^{-x\delta} e^{ix/\delta} \tag{C.3}$$

where δ is the skin depth, given by

$$\delta = \sqrt{\frac{2}{\omega\mu\sigma}} \propto \omega^{-1/2} \tag{C.4}$$

Treating the magnetic field in a similar fashion, current density and magnetic field are given by;

$$j_z = j_0 e^{-\tau_n x} \tag{C.5}$$

$$H_y = H_0 e^{-\tau_n x} \tag{C.6}$$

Integrating the current density to find the total current;

$$I = \int_0^\infty j_z(x)\ dx = \int_0^\infty j_0 e^{-\tau_n x}\ dx = \frac{j_0}{\tau_n} \tag{C.7}$$

using $j_o = \sigma E_0$ to find the impedance leads to;

$$Z = \frac{E_0}{I} = \frac{E_0}{j_0/\tau_n} = \frac{\tau_n}{\sigma} = \sqrt{\frac{i\omega\mu_0}{\sigma}} \tag{C.8}$$

The impedance has an imaginary component as the surface field is out of phase with the current in the conductor, due to the rate that flux is changing in the conductor. The microwave surface resistance of a conductor is;

$$R_s = \sqrt{\frac{\omega\mu_0}{2\delta}} \propto \omega^{1/2} \tag{C.9}$$

In the case of a superconductor there are two components to the current the normal current and the super-current components, using the two fluid model the total current is just the sum of the two components. The normal component is

$j_n = \sigma_n E$ where;

$$\sigma_n = \frac{n_n q^2 \tau}{m} \tag{C.10}$$

here n_n is the number of normal conducting electrons and τ is the relaxation time. For the super-current we get $j_s = -i\sigma_s E$ where

$$\sigma_n = \frac{n_s q^2 \tau}{m\omega} \tag{C.11}$$

The total current then becomes

$$j = j_n + j_s = (\sigma_n - i\sigma_s)E \tag{C.12}$$

Through an analogous treatment to that of the normal conducting case we can show the surface impedance is given by

$$Z_s = \sqrt{\frac{i\omega\mu_0}{\sigma_n - i\sigma_s}} = R_s + iX_s \tag{C.13}$$

At temperatures lower than the critical temperature ($T \ll T_c$), n_n is much smaller than n_s, i.e. there is a transition into the superconducting state and for the normal conducting electrons, the relaxation time ($\approx 10^{-14}$ s) between collisions is much smaller than the rf period ($\approx 10^{-9}$). With these the impedance, Z_s can be obtained obtained and also the surface resistance;

$$R_s = \frac{1}{2}\sigma_n \omega^2 \mu_0^2 \lambda_L^3 \propto \omega^2 \tag{C.14}$$

$$X_s = \omega\mu_0\lambda_L \propto \omega \tag{C.15}$$

with a constant called the London penetration depth, $\lambda_L = \sqrt{m/(N_s q^2 \mu_0)}$. From equations C.9 and C.14 it is clear that SC benefit from operating at lower fre-

quencies significantly more than NC.

Consider a cavity with a fixed accelerating field E_0 and of fixed total energy gain ΔW, the cavity resonant frequency is inversely proportional to the cavity dimension, b. The transit time factor and the fields themselves are independent of the frequency. The cavity parameters scale with frequency. The power dissipated in the walls is then given by;

$$P_d = \frac{1}{2} R_s \int_S |\vec{H}|^2 dS \tag{C.16}$$

For a cavity made from NC material the power dissipated scales as

$$P_d \propto R_s |\vec{H}|^2 b \propto \omega^{1/2}.\omega^{-1} \propto \omega^{-1/2} \tag{C.17}$$

And in the case of a SC cavity

$$P_d \propto R_s |\vec{H}|^2 b \propto \omega^2.\omega^{-1} \propto \omega \tag{C.18}$$

The total energy stored in the cavities is given by

$$U = \frac{1}{2}\epsilon_0 \int_v |\vec{E}|^2 \, dV = \frac{1}{2}\mu_0 \int_v |\vec{H}|^2 \, dV \tag{C.19}$$

Therefore the energy stored in a NC and SC cavity at the same frequency are equivalent and scale as;

$$U \propto |\vec{E}|^2 b^2 \propto \omega^{-2} \tag{C.20}$$

From the stored energy and power dissipated the quality factor Q_0 can be calcu-

lated. Q_0 varies with frequency as

$$Q_0 = \frac{\omega U}{P_d} \tag{C.21}$$

in the case of a NC it scales as

$$Q_0 \propto \frac{\omega.\omega^{-2}}{\omega^{-1/2}} \propto \omega^{-1/2} \tag{C.22}$$

and for the SC case

$$Q_0 \propto \frac{\omega.\omega^{-2}}{\omega} \propto \omega^{-2} \tag{C.23}$$

The parameter R/Q_0 is obtained from

$$\frac{R}{Q_0} = \frac{V_c^2}{\omega U}. \tag{C.24}$$

In the case of both Sc and NC this parameter scales the same and as

$$\frac{R}{Q_0} \propto \frac{|\vec{E}|^2}{\omega.\omega^{-2}} \propto \omega \tag{C.25}$$

The cavity geometry factor is defined as

$$G = \frac{\omega\mu \int_V |\vec{H}|^2 dV}{\int_S |\vec{H}|^2 dS} \propto \frac{\omega.\omega^{-3}}{\omega^{-2}} \propto \omega^0 \tag{C.26}$$

this parameter is independent of frequency since it is a figure of merit purely dependent on the cavity geometry, highlighted by it lack of frequency dependence. The longitudinal loss factor per unit length is defined as

$$k_l = \frac{V_c^2}{4U} \propto \frac{|\vec{E}|^2}{\omega^{-2}} \propto \omega^2 \tag{C.27}$$

the loss parameter varies the same for both NC and SC cavities. The transverse dipole kick factor is defined as

$$k_{\perp} = \frac{k_L^{(1)}}{\omega_1 r^2/c} \tag{C.28}$$

where $k_L^{(1)}$ is the longitudinal loss factor of the dipole ar an offset r from the cavity axis, which is $\propto \omega^2$ and ω_1 is the dipole frequency which is $\propto \omega$. This parameter scales with the fundamental frequency as

$$k_{\perp} \propto \frac{\omega^2}{\omega.\omega^{-2}} \propto \omega^3 \tag{C.29}$$

This is independent of the material from which the cavity is made. The longitudinal and transverse wakefields are proportional to their loss factors and hence we can state;

$$W_L \propto \omega^2 \tag{C.30}$$

$$W_T \propto \omega^3 \tag{C.31}$$

A summary of these results is given in table C.1 below.

Appendix C: Frequency Scaling of Cavity Parameters

Parameter	Superconducting	Normal Conducting
Cavity dimensions (b)	ω^{-1}	ω^{-1}
Surface Resistance (R_s)	ω^{2}	$\omega^{1/2}$
Power Dissipated (P_d)	ω^{1}	$\omega^{-1/2}$
Stored Energy (U)	ω^{-2}	ω^{-2}
Quality Factor (Q_0)	ω^{-2}	$\omega^{-1/2}$
Shunt Impedance (R)	ω^{-1}	$\omega^{1/2}$
Geometry Factor (G)	ω^{0}	ω^{0}
R/Q_0	ω^{1}	ω^{1}
Longitudinal Loss Factor	ω^{2}	ω^{2}
Transverse Kick Factor	ω^{3}	ω^{3}

Table C.1: Table of frequency scaling of important RF parameters for normal conducting and superconducting cavities

Appendix D

Pillbox Loss Factor

To analyse the wakefield in a structure both the modal frequencies and loss factors must be known. In this appendix the loss factors for a pillbox cavity will be derived for a beam of arbitrary velocity, β.

The frequencies of modes in a cylindrical pillbox cavity are given by

$$\omega_{np} = c\sqrt{\left(\frac{j_n}{R}\right)^2 + \left(\frac{\pi p}{g}\right)^2} \tag{D.1}$$

where g is the cell length, R is it's radius, j_n is the n$^{\text{th}}$ zero of the fist Bessel function of the first kind, $J_0(x)$ and c is the speed of light in a vacuum.

The longitudinal electric field in a pillbox cavity is given by;

$$E_z^{np} = \frac{j_n}{R} J_0\left(\frac{j_n r}{R}\right) \cos\left(\frac{\pi p z}{g}\right) e^{i\omega_{np} t}. \tag{D.2}$$

Appendix D: Pillbox Loss Factor

Dropping the time dependent oscillation the accelerating voltage is given by

$$V_{np} = \int_0^g E_z \left(r = 0, z, t = \frac{z}{\beta c} \right) \, dz \tag{D.3a}$$

$$= \int_0^g \frac{j_n}{R} \cos\left(\frac{\pi p z}{g}\right) e^{i\frac{z}{\beta c}} \, dz \tag{D.3b}$$

$$= \frac{j_n}{2R} \int_0^g e^{i(A+B)z} + e^{i(B-A)z} \, dz \tag{D.3c}$$

$$= -\frac{ij_n}{2R} \left[\frac{1}{(A+B)} e^{i(A+B)z} + \frac{1}{(B-A)} e^{i(B-A)z} \right]_0^g \tag{D.3d}$$

$$= -\frac{ij_n}{R} \frac{B}{A^2+B^2} \left(1 - (-1)^p e^{iBg}\right), \tag{D.3e}$$

where $A = \frac{p\pi}{g}$ and $B = \frac{\omega_{np}}{\beta c}$. The stored energy in the mode can be calculated from the magnetic field;

$$H_\phi^{np} = i\omega_{np}\epsilon_0 J_1\left(\frac{j_n r}{R}\right) \cos\left(\frac{\pi p z}{g}\right) e^{i\omega_n p t}, \tag{D.4}$$

to be

$$U_{np} = \int_V H_\phi . H_\phi^* dV = \frac{\pi\epsilon_0}{4} \frac{\omega_{np}^2}{c^2} g R^2 J_1^2(j_n). \tag{D.5}$$

The modal loss factor is then given by

$$k_{np} = \frac{|V|^2}{4U} = \frac{2\left(\frac{j_n B}{R(A^2+B^2)}\right)^2 \left[1 - (-1)^p \cos(Bg)\right]}{\pi\epsilon_0 \left(\frac{\omega}{c}\right)^2 g R^2 J_1(j_n)}. \tag{D.6}$$

By obtaining this parameter the wakefield for pillbox cavity of arbitrary dimensions and bunch can be found.